Precision solar neutrino measurements with Super-Kamiokande-IV

Takaaki Yokozawa

December 18, 2012

Abstract

The solar neutrino results from the fourth phase of the Super-Kamiokande (SK-IV) detector are presented. The main physics goal of this thesis is the direct observation of the matter effect of neutrino oscillations, which is called the Mikheyev-Smirnov-Wolfenstein (MSW) effect, by observing the day/night flux asymmetry and the energy spectrum distortion.

The SK detector is a ring imaging water Cherenkov detector which uses 50,000 tons of pure water as a target for neutrinos and is located 1000 m underground at Ikenoyama, Kamioka, Japan. The front end electronics and data acquisition system were replaced in September of 2008 and observation was started as the SK-IV phase. With improvements of the water circulation system, the detector simulation, and the analysis method, a lower background level was achieved in the central region of the detector and we were successful in setting the lower energy threshold down from 4.5MeV to 4.0 MeV (in kinetic electron energy). The systematic uncertainty on the total ^{8}B flux is reduced to $\pm$1.7%, which is much improved compared with SK-I ($^{+3.5\%}_{-3.2\%}$) and SK-III ($\pm$2.2%). The ^8B flux from 4.0 to 19.5 MeV(kinetic) of SK-IV is measured to be 2.34 ± 0.03(Stat.) ± 0.04(Syst.) [$\times$ 10^6/cm^2/s], which is consistent with the SK-I,II,III results.

The neutrino oscillation analysis with combining all the SK phase gives the best fit oscillation parameters of $\sin^2(\theta_{12}) = 0.339^{+0.028}_{-0.024}$ and $\Delta m^2_{21} = 4.69^{+1.80}_{-0.83} \times 10^{-5}$eV^2, where the total ^{8}B flux is constrained to (5.25$\pm$0.21)[$\times 10^6$/cm^2/s], which is the result from the SNO NC measurement. Combining further with other solar experiments and the KamLAND reactor result, the best fit oscillation parameters are obtained as $\sin^2(\theta_{12}) = 0.304^{+0.013}_{-0.013}$ and $\Delta m^2_{21} = 7.44^{+0.20}_{-0.19} \times 10^{-5} eV^2$.

The χ^2 values of the spectrum fit of the SK data with MSW predictions for the two best fit oscillation parameters described above, and for an assumption of a flat shape (constant reduction factor independent of energy) are 76.54, 79.02 and 75.29 for 81 d.o.f, respectively. So the flat shape is preferred at the 1.1-1.9σ level, compared with the best fit oscillation parameters predictions.

By introducing a method to measure the day/night asymmetry with a constraint on the expectation from matter effect and by improving systematic uncertainties, the SK combined day/night asymmetry was obtained as A_{DN}(=(day-night)/$\frac{1}{2}$(day+night)) = -2.8 $\pm$ 1.1(stat.) $\pm$0.5(syst.) [%]. So, a non-zero day/night asymmetry is observed at the 2.3σ level.

Acknowledgments

I would like to express my gratitude to Prof. Masayuki Nakahata for introducing me to the Super-Kamiokande experiment and for giving me many knowledge and suggestions for solar neutrino analysis. This thesis would never exist without his close support and encouragement.

I would like to appreciate to Prof. Yoichiro Suzuki, the spokesperson of the Super-Kamiokande experiment for giving me the oppotunity of studing in the Super-Kamiokande experiment.

I would like to thank grealty to members who worked with me on the solar neutrino analysis, Dr. Y.Koshio, Dr. H.Sekiya, Prof. Y.Takeuchi, Prof. M.Smy and A.Renshaw.

I would like to thank to LOWE (low energy analysis group) members, Prof. Y.Kishimoto, Dr. A.Takeda, Dr. L.Marti, Dr. S.Yamada, Dr. H.Watanabe Dr. T.Iida, Dr. M.Ikeda, Dr. B.Yang, Dr. K.Ueno, Y.Nakano, Prof. M.Vagins, Prof. K.Martens, Dr. K.Bays, Dr. G.Carminati, Prof. M.Sakuda, Prof. H.Ishino, Dr. A.Kibayashi, Dr. T.Yano, T.Mori, H.Toyota, S.Mino, J.Takeuchi, R.Yamaguchi, Prof. Chen.S, Dr. H.Zhang, Y.Zhang, Prof. Y.Fukuda, Prof. S.Tasaka and Prof. L.Labarga.

I would like to thank to all other ICRR staffs who worked with me, Prof. T.Kajita, Prof. K.Kaneyuki, Prof. M.Shiozawa, Prof. Y.Hayato, Prof. S.Moriyama, Prof. M.Yamashita, Prof. K.Okumura, Dr. M.Miura, Dr. Y.Obayashi, Dr. J.Kameda, Dr. K.Abe, Dr. R.Wendell, Dr. H.Ogawa, Dr. K.Kobayashi, Dr. S.Nakayama, Dr. K.Hiraide, Dr. Y.Nishimura, Dr. T.Tomura, Dr. H.Tanaka, Dr. N.Tanimoto, Dr. Y.Shimizu, Dr. H.Kaji, Dr. Y.Takenaga, Dr. N.Okazaki and Dr. J.Liu.

I also would like to thank to my friends and stuffs who supported me all the time in Kamioka, Dr. G.Mitsuka, Dr. H.Nishino, Dr. K.Ueshima, Dr. C.Isihara, Dr. T.Tanaka, T.F.McLachlan, Y.Nakajima, S.Hazama, Dr. D.Motoki, Y.Yokosawa, Y.Kozuma, Maggie, K.Choi, P.de perio, S.Tobayama, Prof. S.Nakamura, I,Murayama, K.Fujii, H.Nishiie, A.Shinozaki, K.Iyogi, H.Uchida, S.Hirano, Y.Nishitani, M.Miyake, K.Otsuka, K.Hieda, O.Takachio, D.Umemoto, Y.Nakano, H.Takiya, K.Hosokawa, A.Murata, N.Oka, K.Nakagawa, I.Kametani, Y.Haga and S. Higashi.

Finally, I wish to express my deep gratitude to my friends and family.

Contents

Chapter 1

Introduction

The Sun continuously produces a huge amount of energy. The origin of this energy is now understood to be nuclear fusion. The generated energy which is released as photons is slowly diffused to the surface of the Sun, over the course of $\sim 10^5$ years, due to high density of the Sun interior. On the other hand, neutrinos which are created in the solar core can provide direct information of the center of the Sun, due to neutrinos having a very small reaction cross section, even given the high density region of the Sun. So, measurements of solar neutrinos give an important test for the theories of stellar evolution and structure.

The neutrino was first introduced by Pauli in 1930 as 'verzweifeltes ausweg (desperate remedy)', in order to preserve the energy consevation law in the beta decay process. It was discovered in 1956 by F.Reines and C.L.Cowan by observing electron anti-neutrinos from a nuclear reactor[1]. In the Standard Model of the elementary particles, the neutrino is a lepton which has a spin of 1/2 and no electric charge, has three flavors (ν_e, ν_μ and ν_τ) and was originally regarded as a massless particle.

The first solar neutrino observation was carried out by R.Davis and his colleagues, using ^{37}Cl atoms[2]. This experiment started around 1968 and gave results which observed that the solar neutrino flux is about 33% of the expected flux estimated by the Standard Solar Model (SSM). This problem was dubbed the solar neutrino problem. In 1989, the solar neutrino problem was confirmed by the Kamiokande experiment[3], which was a 3,000 ton water Cherenkov detector. The deficit of the solar neutrino flux was also observed in the Ga detectors (GALLEX and SAGE) in the early 1990's[4][5].

In 2001, the solar neutrino problem was understood in terms of neutrino oscillations by comparing the ^{8}B flux results from Super-Kamiokande (SK)[6], via the electron-scattering method, and the Sudbury Neutrino Observatory (SNO)[7], via the charged current interaction. The theory of neutrino oscillations tells us that neutrinos have finite masses and that the mixing happens between their mass eigenstates and interaction eigenstates, which are not the same.

Neutrino oscillations are purely quantum mechanical phenomena, which can be understood in terms of a traveling wave function. If neutrinos travel through matter, a potential energy induced by weak interactions with matter (called matter effect, hereafter) will affect the neutrino oscillations. In order to understand current solar neutrino experimental results, the matter effect is necessary, but gives an indirect measurement of neutrino oscillations. This thesis focuses on the matter effect introduced by S. P. Mikheyev, A. Yu. Smirnov and L. Wolfenstein in 1985, often called the MSW effect[8][9]. Direct effects coming from the MSW theory are expected to be observed by precise measurements of the solar neutrino energy spectrum and the flux difference

between daytime and nighttime. The former is due to the matter effect through the Sun, while the latter is due to the matter contained within the Earth.

The structure of this thesis is as follows; the details of the standard solar model, neutrino oscillations and the MSW effect and current results from solar neutrino experiments are described in chapter 2. In chapter 3, the Super-Kamiokande experiment is described, and in chapters 4-7, details of the solar neutrino analysis at Super-Kamiokande are described. The obtained solar neutrino results from the 4th phase of SK are summarized in chapter 8, and SK combined results are summarized in chapter 9. Finally, the discussion and conclusion are given in chapters 10 and 11.

Chapter 2

Solar Neutrinos

The Standard Solar Model (SSM) is the well-established theoretical model of the sun, which takes into account the properties of the Sun which have been measured or calculated independently. In this chapter, the basic ideas of the SSM, neutrinos which are generated in the Sun and the solar neutrino experiments are described. Important neutrino phenomenon, such as neutrino oscillations and its current parameters, are also described. Finally, the motivations of current solar neutrino analyses are described.

2.1 The Standard Solar Model and solar neutrinos

The Sun is considered to be a main sequence star. Because of its proximity to the Earth, studying about the Sun is the best way to understand stellar evolution. In the Standard Soalr Model (SSM), the Sun is assumed to be spherical and to have evolved quasi-statically over a period of about 4.6×10^9years (age of Sun). The evolution of the Sun is manifested by the loss of photons from its surface, which is in turn balanced by the burning of protons into α particles within the core of the Sun. It produces an intense flux of electron neutrinos as a consequence of the nuclear fusion reaction, written as

$$4p \rightarrow {}^4He + 2e^+ + 2\nu_e. \tag{2.1}$$

with releasing an energy of 26.7 MeV as a form of photons. The reaction given in (2.1) is in the form of a net reaction, which proceeds via two different branches. One is called the proton-proton chain (pp chain), which is shown in Fig.2.1. In the pp chain reaction, five types of neutrinos are generated by the following reactions, with unique or maximum neutrino energy;

$$p + p \longrightarrow {}^2H + e^+ + \nu_e \qquad \text{(pp, } E_\nu \text{<0.42 MeV)} \tag{2.2}$$

$$p + e^- + p \longrightarrow {}^2H + \nu_e \qquad \text{(pep, } E_\nu\text{=1.442 MeV)} \tag{2.3}$$

$${}^7Be + e^- \longrightarrow {}^7Li + \nu_e \qquad \text{(}^7\text{Be, } E_\nu\text{=0.861,0.383 MeV)} \tag{2.4}$$

$${}^8B \longrightarrow {}^8Be^* + e^+ + \nu_e \qquad \text{(}^8\text{B, } E_\nu \text{<14.06 MeV)} \tag{2.5}$$

$${}^3He + p \longrightarrow \alpha + e^+ + \nu_e \qquad \text{(hep, } E_\nu \text{<18.77 MeV).} \tag{2.6}$$

The other fusion reaction branch is called the Carbon-Nitrogen-Oxygen cycle (CNO cycle) and is shown in Fig.2.2. There are three generated neutrinos by the following reactions;

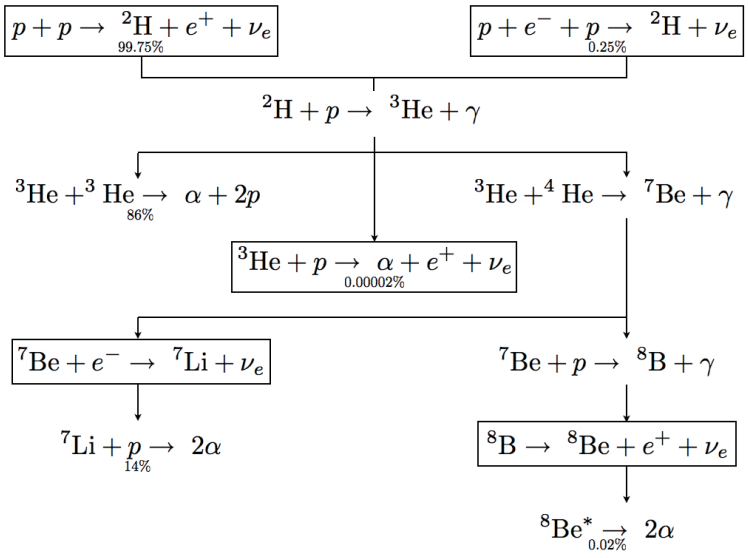

Figure 2.1: Schematic view of the pp chain reactions.

$$^{13}N \longrightarrow {}^{13}C + e^+ + \nu_e \qquad (E_\nu < 1.27 \text{ MeV}) \tag{2.7}$$

$$^{15}O \longrightarrow {}^{15}N + e^+ + \nu_e \qquad (E_\nu < 1.73 \text{ MeV}) \tag{2.8}$$

$$^{17}F \longrightarrow {}^{17}O + e^+ + \nu_e \qquad (E_\nu < 1.74 \text{ MeV}). \tag{2.9}$$

According to the SSM [10], about 98.4% of the total solar luminosity is predicted to be generated by the pp chain, while the remaining 1.6% is thought to be generated by the CNO cycle.

Fig.2.3 shows the generated solar neutrino energy spectrum predited by the BP04 SSM [11], which was developed by J.N.Bahcall and M.H.Pinsonneault in 2004. The BP04 SSM predicted a ^{8}B neutrino flux of 5.79 $(1\pm0.23)[\times 10^6/cm^2/s]$. The upper figure in Fig.2.4 shows the electron density in the Sun, predicted by the BP04 SSM. The lower figure in Fig.2.4 shows the matter density of Earth, taken from the PREM model [12]. As described in section 2.3, these matter density profiles are used as input to determine neutrino oscillations in matter.

2.2 Solar neutrino experiments

In this section, past and current solar neutrino experiments are introduced. These experiments have made great contributions to solar neutrino understanding, and are used in the global oscillation analysis, which is described in section 10.

2.2.1 Radiochemical experiments

Chlorine experiment

The first observation of neutrinos coming from the sun was accomplished around 1968, by Raymond Davis Jr., using an underground chlorine neutrino detector at the Homestake gold

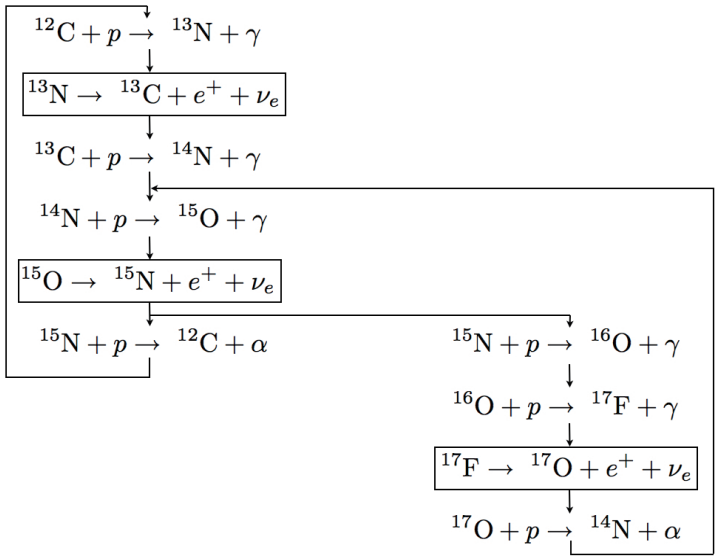

Figure 2.2: Schematic view of the CNO cycle reactions.

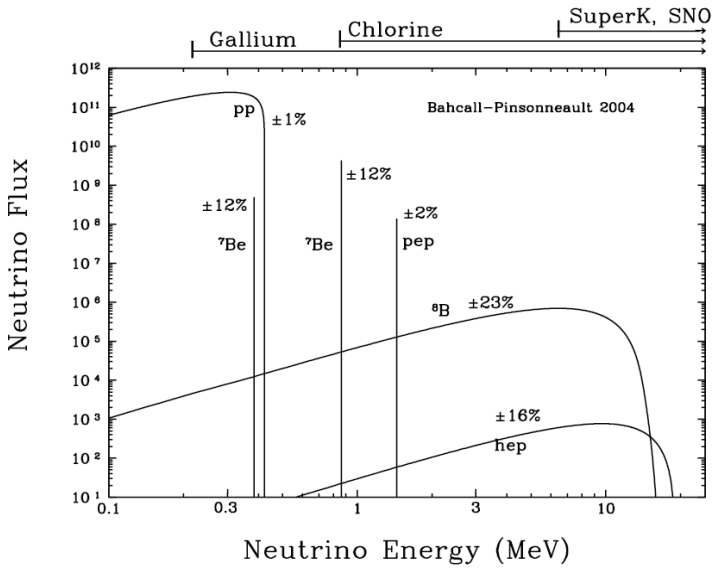

Figure 2.3: The solar neutrino energy spectrum predicted by BP04 SSM. The value in percentage written beside each neutrino spectrum correspond to total flux uncertainties.

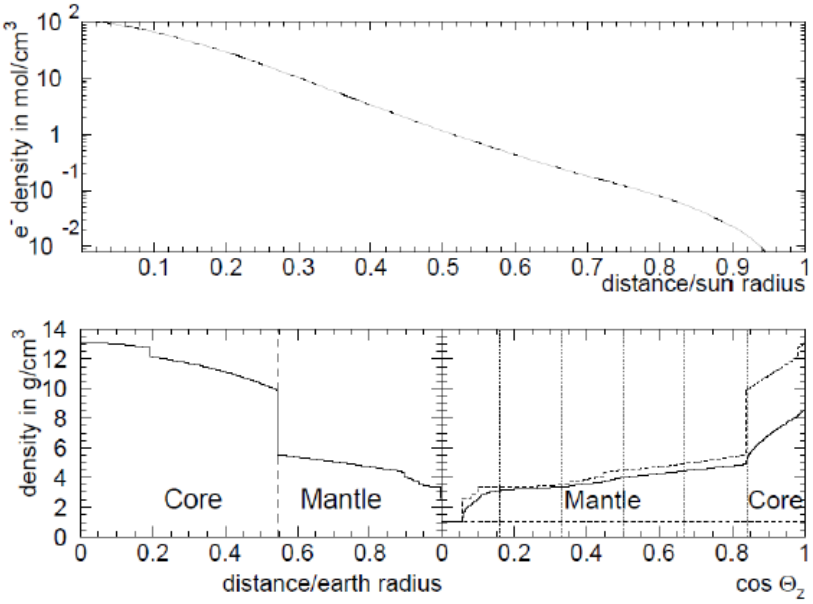

Figure 2.4: Top figure: the electron density of the Sun as a function of distance to surface ($r/r_{\odot}$) calculated by the BP04 SSM. Bottom figure: the mass density of the Earth as a fuction of distance to the surface (left), the minimum (lower dashed line), the average (solid line) and the maximum (upper dashed line) mass density as a function of cosine of zenith angle ($\cos\Theta_z$).

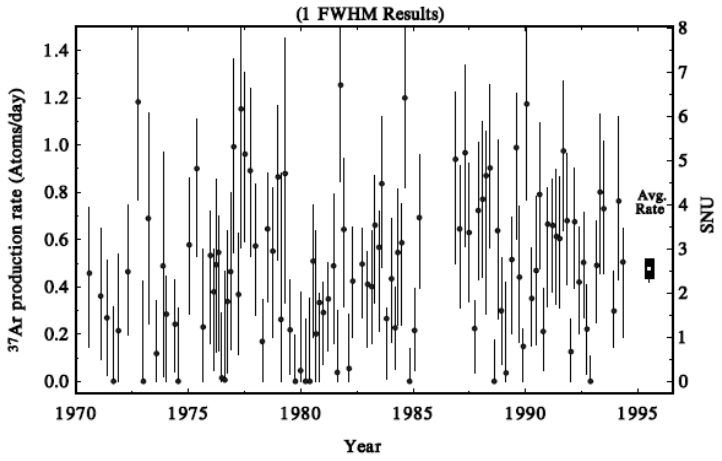

Figure 2.5: The results of the production rate of ^{37}Ar with the Homestake chlorine detector. The errors shown for individual measurements(except of right point) are statistical errors only, while the error shown for the cumulative result is a combination of the statistical and systematic errors in quadrature.

mine in the USA [2]. This detector was located 1778 m underground, and consisted of 615 tons of C_2Cl_4. This experiment started in 1967 and continued the observation until 1994. The neutrino is detected by absorption on the chlorine, written as

$$\nu_e + ^{37}Cl \rightarrow ^{37}Ar + e^-. \tag{2.10}$$

The energy threshold of this interaction is 0.814 MeV, so the Cl experiment was sensitive to ^{8}B, ^{7}Be, pep and CNO neutrinos. The generated ^{37}Ar atoms were extracted by bubbling He gas through the detector's tank, with a collection effeciency of 95%, and then counted by a proportional counter. This extraction was done once every 1-3 months. Fig.2.5 shows the results of the production rate of ^{37}Ar. The average rate was 2.56±0.16(Stat.)±0.16(Syst.) SNU[1], which corresponded to about one third from expectation.

Gallium experiments

The SAGE expriment in Russia [4] and the Gallex/GNO experiments [5][16] in Italy used a gallium target for detecting neutrinos via neutrino absorption on gallium. The reaction is written as

$$\nu_e + ^{71}Ga \rightarrow ^{71}Ge + e^-. \tag{2.11}$$

The SAGE (Soviet-American Gallium Experiment) was located deep underground at the Baksan Neutrino Observatory and began observation in 1990. It used 50 tons of liquid metal Gallium target, in seven chemical reactors that are heated to 30°C, so that the gallium metal remains molten. The resulting Ge atoms were counted by a proportional counter observing Auger electrons and X-rays emitted by the ^{71}Ge electron capture.

[1]A SNU (Solar Neutrino Unit) is the number of interaction per 10^{36} targets per second.

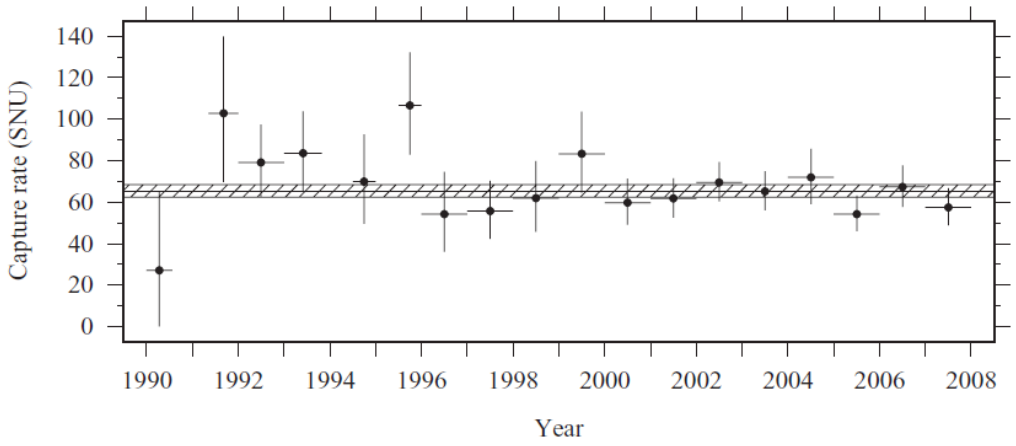

Figure 2.6: The combined SAGE results for each year. The shaded band is the combined best fit and its uncertainty for all years. Error bars shown for individual measurements are statistical errors only.

The Gallex experiment began observation in 1991 and was replaced by GNO (Gallium Neutrino Observatory) in 1998. The Gallex/GNO detector was located in the Gran Sasso Underground Laboratory in Italy and used a 100 ton target of $GaCl_3$-HCl solution, which contains 30.3 tons of gallium. The extraction and the subsequent counting were done every 4-6 weeks.

The advantage of the gallium experiments is the low energy threshold, 0.233 MeV. This low energy threshold allows for the observation of the pp neutrinos. Fig.2.6 shows the combined SAGE results for each year, with the combined observed flux given as $65.4^{+3.1}_{-3.0}(\text{stat.})^{+2.6}_{-2.8}(\text{syst.})$ SNU [4]. Fig.2.7 shows the combined Gallex/GNO result, with the joined flux of Gallex and GNO found to be 69.3±4.1(stat.)±3.6(syst.) SNU [16]. The weighted average of the results of all three Ga experiments, SAGE, Gallex and GNO, is calculated as 66.1±3.1 SNU, which corresponded to about one second from expectation.

2.2.2 SNO experiment

The SNO (Sudbury Neutrino Observatory) experiment [7] was a Cherenkov detector which used 1000 tons of heavy water (D_2O) and ran from 1999 to 2006. It was located 2092 m below the surface in the Creighton mine in Sudbury, Canada. The SNO detector observed ^{8}B neutrinos via three different reactions;

$$\nu_x + d \rightarrow \nu_x + p + n \qquad \text{(Neutral Current(NC))} \tag{2.12}$$
$$\nu_e + d \rightarrow e^- + p + p \qquad \text{(Charged Current(CC))} \tag{2.13}$$
$$\nu_x + e^- \rightarrow \nu_x + e^- \qquad \text{(Elastic Scattering(ES))}, \tag{2.14}$$

where x=e,μ,τ. The characteristics of each reactions are;

- Neutral Current (NC):

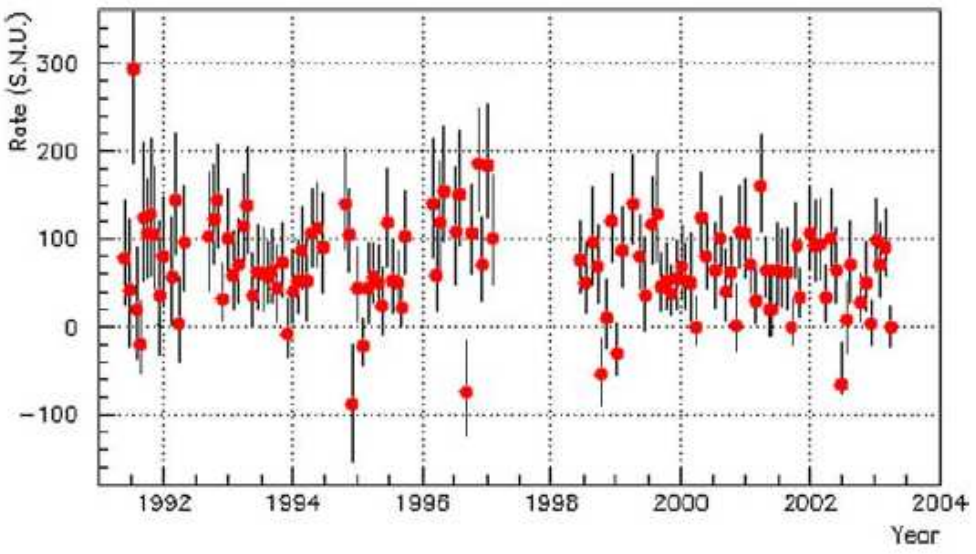

Figure 2.7: The joined Gallex and GNO result. The error bars are statistical errors only.

Equally sensitive to all three active neutrino flavors. This reaction can determine the total ^{8}B neutrino flux ($\Phi_{^8B}$) independently of any specific active neutrino flavor oscillation hypothesis.

- Charged Current (CC):

  Only sensitive to ν_e. Comparing this rate to the NC reaction rate, it is possible to determine the neutrino survival probability as a function of energy.

- Elastic Scattering (ES):

  Sensitive to all neutrino flavors, but the cross section for the ν_e is approximately six times larger than that for the $\nu_{\mu,\tau}$. This reaction is described in detail in section 3.1.1

The SNO detector operated in three phases which are distinguished by the method of the neutrino detection from the NC interactions (2.12).

- Phase1 : $n + d \rightarrow t + \gamma(6.25\text{MeV})(\text{D}_2\text{O})$
- Phase2 : $n +^{35} Cl \rightarrow^{36} Cl + \gamma(8.6\text{MeV})(\text{Salt})$
- Phase3 : $n +^3 He \rightarrow p + t + 0.76\text{MeV}(\text{NCD array})$

The combined NC reaction rate, energy spectrum and day/night asymmetry results of all phases will be described in section 10.1.

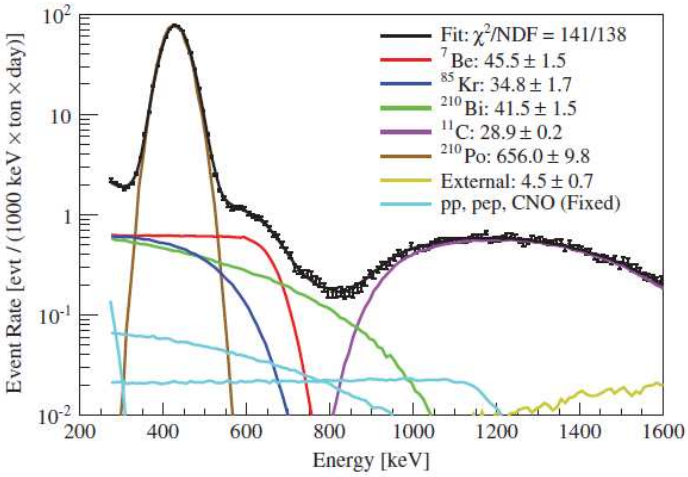

Figure 2.8: A Borexino Monte Carlo best fit result in the units of [counts/day/100 ton] and over the energy region of 270 to 1600 keV.

2.2.3 Borexino experiment

The Borexino experiment [17] is a liquid scintillator experiment located in the Laboratori Nazionali del Gran Sasso (LNGS). This detector is filled with ∼278 metric tons of organic liquid scintillator and began observation in May of 2007. Borexino observed sub-MeV (low energy) solar neutrinos by means of electron scattering.

Fig.2.8 shows a Monte Carlo best fit over the energy region of 270 to 1270 keV. The Borexino experiment obtained the ^{7}Be, pep and CNO neutrino fluxes as

$$
\begin{aligned}
^{7}Be \text{ rate(862 keV line)} &: 46.0 \pm 1.5(\text{Stat.})^{+1.5}_{-1.6}(\text{Syst.}) \text{ [count/day/100 ton]} \\
&\rightarrow 2.78 \pm 0.13[10^{9}/cm^{2}/s] \qquad (2.15) \\
\text{pep rate} &: 3.1 \pm 0.6(\text{Stat.}) \pm 0.3(\text{Syst.}) \text{ [count/day/100 ton]} \\
&\rightarrow 1.6 \pm 0.3[10^{8}/cm^{2}/s] \qquad (2.16) \\
\text{CNO rate} &: < 7.9\text{count/day/100 ton} \\
&\rightarrow < 7.7[10^{8}/cm^{2}/s](95\%\text{C.L.}). \qquad (2.17)
\end{aligned}
$$

2.3 Neutrino oscillations

Neutrino oscillations were first proposed by Z. Maki, M. Nakagawa, S. Sakata, V. Gribov and B. Pontecorvo in 1969[14]. In this section, the theories of neutrino oscillations are described.

2.3.1 Oscillations in vacuum

The flavor eigenstates can be expanded in terms of the neutrino mass eigenstates ($|\nu_j\rangle$, j=1,2,3) as

$$|\nu_\alpha\rangle = U|\nu_j\rangle, \tag{2.18}$$

where ν_α (α=e,μ,τ) are the flavor states and U is often called the Pontecorvo-Maki-Nakagawa-Sakata (PMNS) or Maki-Nakagawa-Sakata (MNS) mixing matrix, and can be written as

$$U = \begin{pmatrix} 1 & 0 & 0 \\ 0 & C_{23} & S_{23} \\ 0 & -S_{23} & C_{23} \end{pmatrix} \begin{pmatrix} C_{13} & 0 & S_{13}e^{-i\delta} \\ 0 & 1 & 0 \\ -S_{13}e^{i\delta} & 0 & C_{13} \end{pmatrix} \begin{pmatrix} C_{12} & S_{12} & 0 \\ -S_{12} & C_{12} & 0 \\ 0 & 0 & 1 \end{pmatrix} \tag{2.19}$$

where $C_{ij} \equiv \cos\theta_{ij}$ and $S_{ij} \equiv \sin\theta_{ij}$ are the miximg angle between the ith and jth mass eigenstates. δ is the CP violation phase in the neutrino sector.

For simplicity, neutrino oscillations between only two flavor eigenstates are described first. The relationship between the flavor eigenstates ($|\nu_e\rangle$, $|\nu_x\rangle$) and the two mass eigenstates($|\nu_1\rangle$, $|\nu_2\rangle$) can be written as

$$\begin{pmatrix} |\nu_e\rangle \\ |\nu_x\rangle \end{pmatrix} = U \begin{pmatrix} |\nu_1\rangle \\ |\nu_2\rangle \end{pmatrix} = \begin{pmatrix} cos\theta & sin\theta \\ -sin\theta & cos\theta \end{pmatrix} \begin{pmatrix} |\nu_1\rangle \\ |\nu_2\rangle \end{pmatrix}. \tag{2.20}$$

The time dependence of the mass eigenstates can be obtained by solving the time dependent Schroedinger equation, which is described as

$$|\nu_j(t)\rangle = |\nu_j(0)\rangle exp(-iE_j t). \tag{2.21}$$

By solving this equation, the transition probability from ν_e to ν_x can be written as

$$\begin{aligned} P(\nu_e \to \nu_x, L) &= sin^2 2\theta_{12} sin^2(\frac{1.27\Delta m^2_{21}[eV^2]L[m]}{E[MeV]}) \\ &= sin^2 2\theta_{12} sin^2(\pi \frac{L}{L_{OSC}}) \\ L_{OSC} &\equiv \frac{\pi}{1.27}\frac{E}{\Delta m^2_{21}}, \end{aligned} \tag{2.22}$$

where L is the travel distance, E the neutrino energy and $\Delta m^2_{21} = m^2_2 - m^2_1$ is a squared mass difference of mass eigenstates 2 and 1. Thus, the ν_e survival probability can be written as

$$P(\nu_e \to \nu_e, L) = 1 - sin^2 2\theta_{12} sin^2(\frac{1.27\Delta m^2_{21} L}{E}). \tag{2.23}$$

The electron neutrino survival probability can be described as a function of distance (L) after traveling, neutrino energy (E), squared mass difference (Δm^2_{21}) and mixing angle (θ_{12}). The values of Δm^2_{21} and θ_{12} are called 'oscillation parameters'.

2.3.2 Oscillation in Matter

When a neutrino travels through matter, the propagation is affected by the weak field of electrons, neutrons and protons via neutral current exchanging of Z^0, while an electron neutrino is only affected by the weak field of charged current interactions (i.e. via $W^{\pm}$ exchange) with

electrons. This $W^{\pm}$ weak field causes additional terms in the Hamiltonian, as seen in the following equation. This effect is called the 'MSW[2] effect' [8][9]. The Hamiltonian $\mathcal{H}$ in the two flavor eigenbasis can be expressed as

$$\mathcal{H} = \mathcal{H}_v + \mathcal{H}_M \tag{2.24}$$

$$= \frac{\Delta m^2}{4E} \begin{pmatrix} -\cos 2\theta & \sin 2\theta \\ \sin 2\theta & \cos 2\theta \end{pmatrix} + \begin{pmatrix} V & 0 \\ 0 & 0 \end{pmatrix}, \tag{2.25}$$

where $\mathcal{H}_v$ is the Hamiltonian in vacuum, the $\mathcal{H}_M$ is that while in matter and V is the potential of the charged current interaction which can be described as

$$V = 2\sqrt{2} G_F N_e, \tag{2.26}$$

where G_F is Fermi coupling constant and N_e is the electron density of the matter. By applying this Hamiltonian to the Schroedinger equation, the eigenstates in matter can be written as

$$\begin{pmatrix} |\nu_1^M\rangle \\ |\nu_2^M\rangle \end{pmatrix} = \begin{pmatrix} cos\theta_M & -sin\theta_M \\ sin\theta_M & cos\theta_M \end{pmatrix} \begin{pmatrix} |\nu_e\rangle \\ |\nu_x\rangle \end{pmatrix}, \tag{2.27}$$

where θ_M is the effective mixing angle in matter and is written as

$$tan2\theta_M = \frac{tan2\theta}{1 - \frac{VE}{\Delta m^2 cos2\theta}}. \tag{2.28}$$

The survival probability in matter is then obtained by replacing θ in equation 2.23 with θ_m and replacing L_{OSC} with the oscillation length in matter L_m, which is written as

$$L_M = \frac{\pi}{1.27\sqrt{(2V + \frac{\Delta m^2}{E}\cos 2\theta)^2 + (\frac{\Delta m^2}{E}\sin 2\theta)^2}}. \tag{2.29}$$

2.3.3 Possible solution of solar oscillation parameters

A simple example of solar neutrino oscillations is the transition of ν_e, generated within the Sun, to $\nu_{\mu,\tau}$ during the trip to Earth, while undergoing vacuum neutrino oscillations. The survival probability is calculated by equation (2.23), with L=150×10^6 km (distance from Sun to Earth). This possible scenario is known as the vacuum (VAC) solution.

Other solutions are obtained by taking into account matter effects. Using the electron density at the Sun and Earth (Fig.2.4), the ν_e survival probability, which takes into account the MSW effect, can be calculated. Fig.2.9 shows how a generated neutrino can adiabatically change its flavor while the electron density varies slowly. At very small electron densities, the electron neutrino almost coincides with the lower mass eigenstate $|\nu_1\rangle$, for the small vacuum mixing angle case. The second flavor eigenstate approximately coincides with the mass eigenstate $|\nu_2\rangle$. The mass of the heavier mass eigenstate increases monotonically with ambient electron density and becomes asymptotically proportional to the electron density. If $m_2 \geq m_1$, at large electron densities the heavier mass eigenstate, $|\nu_2\rangle$, becomes close to $|\nu_e\rangle$, while the lower mass eigenstate,

[2]S. P. Mikheev, A. Yu. Smirnov and L. Wolfenstein

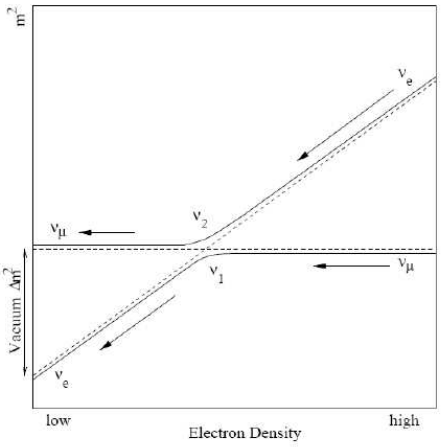

Figure 2.9: The mass eigenstates in matter as a fuction of electron density.

$|\nu_1\rangle$, remains essentially unchanged as a function of electron density. An electron neutrino that is created in the solar interior moves from high densities to lower densities. If the electron density changes at a sufficiently slow rate, no transitions occur between the mass eigenstates. The electron neutrino remains close to mass eigenstate $|\nu_2\rangle$ and exits from the Sun as essentially a different flavor eigenstate, $|\nu_x\rangle$. The regions within the plane of oscillation parameters allowed by current solar neutrino fluxes observed by the Cl, Kamiokande, and Gallium experiments are separately distributed at the small mixing angle (SMA), the large mixinig angle (LMA) and low mass difference (LOW) solutions. The location of these four solutions are shown in Fig.2.10. Now, including measurements by SK and SNO (and with Borexino), the LMA solution is uniquely selected at very high confidence level.

Because the MSW effect depends on the neutrino energy, the survival probability of generated ν_e is energy dependent. This causes a distortion to the observed energy spectrum. As the MSW effect converts ν_e to ν_x on its way out of the Sun, ν_x to ν_e conversion can happen when passing through the Earth. This effect leads to the prediction that the observed electron neutrino flux during the nighttime (when earth is between the detector and the sun) is larger than that of daytime (when the earth is not between the two). This flux difference is called the 'day/night asymmetry'. As described in section 2.5, these direct observations of the MSW effect from the observed energy spectrum distortion and from the day/night flux difference are the main topics of this thesis.

2.4 Latest results of oscillation parameters

The mixing angle θ_{13} remained poorly known and only an upper limit was given before 2010. But recently, T2K and various short baseline reactor experiments observed a non-zero θ_{13} value and is now precisely determined with an accuracy of 10% in $\sin^2(\theta_{13})$. In this section, the measurements and results of θ_{13} from the various experiments and the precise oscillation parameter results from the KamLAND experiment are described.

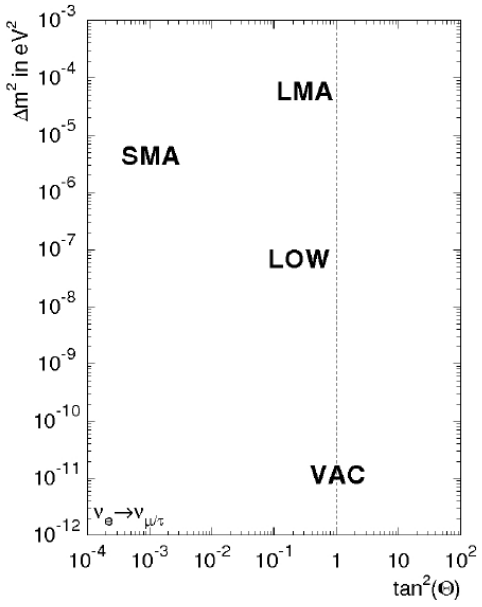

Figure 2.10: The location of possible solutions of solar oscillation parameters ($\tan^2\theta_{12}$,$\Delta m2$ in eV^2).

2.4.1 θ_{13} from short baseline reactor experiments

The short baseline reactor experiments give a precise value for θ_{13}. Since the value of θ_{13} affects the analysis of solar neutrino oscillations, some details of the short baseline reactor experiments are described in this section. For experiments with L/E around 0.5 km/MeV, which was adopted by the short baseline reactor experiments, the survival probability of $\bar{\nu}_e$ can be writtern as

$$P(\bar{\nu}_e \rightarrow \bar{\nu}_e) = 1 - sin^2(2\theta_{13})sin^2(1.27\Delta m^2_{atm}L/E) + O(\Delta^2_{21}), \tag{2.30}$$

where Δm^2_{atm} is the effective atmospheric mass squared difference, measured to be $|\Delta m^2_{atm}|$ = $(2.32^{+0.12}_{-0.08})\times10^{-3}$ eV^2 [18]. This survival probability comes from a simple 2 flavor oscillation formula with no matter effects included, and shows that reactor experiments with a short base line ($\sim$1km) can ignore the disappearance of $\bar{\nu}_e$, driven by θ_{12} and Δm^2_{21}. Thus, we can unambiguously determine the mixiing angle θ_{13} based on the survival probability of electron antineutrinos. Reactor neutrinos are actually antineutrinos, but by assuming CPT invariance, the value of θ_{13} obtained by antineutrino oscillation experiments can be adopted to the analysis of solar neutrino experiments.

The reactor $\bar{\nu}_e$ neutrinos are detected via the inverse beta decay reaction, which is written as

$$\bar{\nu}_e + p \rightarrow e^+ + n, \tag{2.31}$$

with a 1.8 MeV threshold. Using the coincidence of a prompt positron signal (e^+) and a delayed signal coming from the neutron capture by gadolinium or a proton, the inverse beta decay events

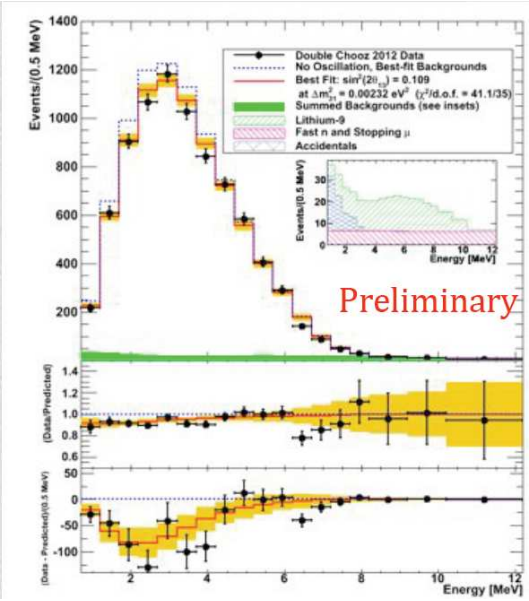

Figure 2.11: Energy spectrum obtained by the Double Chooz experiment. Top figure: Expected energy spectrum for the no-oscillation case (blue dashed line) and for the best fit oscillation parameters (red solid line), along with measured spectrum (black). Middle figure: Difference between data and the no-oscillation spectrum with the best fit expectation(red). Bottom figure: Difference between data and the no-oscillation spectrum with the best fit expectation.

can be distinguished from backgrounds.

Double Chooz experiment

The Double Chooz detector [19] is located at the Chooz nuclear power station in the Ardennes region of northern France. The far detector is placed ∼1000 m from the reactor cores, contains a 10 m^3 target of Gd loaded liquid scintillator and started observation in April 2011. The near detector will be placed ∼400 m from the reactor cores, with same target as the far detector and the plan is to start observation in 2013. Fig.2.11 shows the energy spectrum of the so far observed data, with predictions of no-oscillation and best-fit oscillation parameters included. Double Chooz indicated reactor $\bar{\nu}_e$ disappearance and gives $sin^2(2\theta_{13})$ as

$$sin^2(2\theta_{13}) = 0.109 \pm 0.030(Stat.) \pm 0.025(Syst.), \tag{2.32}$$

with 227.9 days live time.

Daya Bay

The Daya Bay detector [20] is located on the southern coast of China near 6 reactors located at the Daya Bay nuclear power plant (D1,D2) and the Ling Ao nuclear power plant (L1,L2,L3,L4), and is made up of 3 experimental halls (EH1,EH2,EH3) and 6 antineutrino detectors (AD1-AD6).

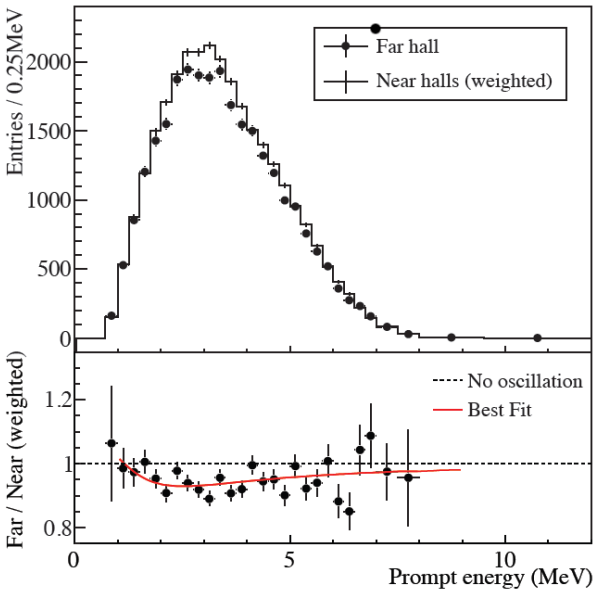

Figure 2.12: Energy spectrum obtained at the Daya Bay experiment. Top figure: The measured energy spectrum of the far hall (sum of three far ADs) compared with the no-oscillation prediction based on the measurements of the two near halls. Bottom figure: The ratio between measured and predicted spectra. The solid curve is the expected ratio with oscillations and assuming $sin^2(\theta_{13})$=0.089. The dashed line is the no-oscillation prediction.

The antineutrino detectors consist of ∼20 tons of gadolinium-doped liquid scintillator, with 0.1% Gd by weight in the innermost volume. Fig.2.12 shows the measured energy spectrum of the far hall compared with the no-oscillation prediction based on the measurements of the two near halls and also the ratio between those two. The Daya Bay experiment gives the result of

$$sin^2(2\theta_{13}) = 0.089 \pm 0.010(Stat.) \pm 0.005(Syst.), \tag{2.33}$$

using data from the observation period of Dec. 2011 to May. 2012.

RENO experiment

The RENO experiment [21] is placed near the Yonggwang nuclear power plant and is located on the west coast of South Korea. There are six reactors, with the near and far detectors located 209 m and 1400 m from the center of the reactor array, respectively. The near detector is located 79 m underground from the ridge, while the far detector is located 260 m underground in a mountain. The detectors hold 18.6 m^3 of hydrocarbon liquid scintillator with gadolinium.

Fig.2.13 show the observed energy spectrum in the far detector compared with the non-oscillation prediction from the measurements in the near detector. A rate-only analysis obtains the result of

$$sin^2(2\theta_{13}) = 0.113 \pm 0.013(Stat.) \pm 0.019(Syst.), \tag{2.34}$$

with 228 live time days occurring between Aug. 2011 and Mar. 2012.

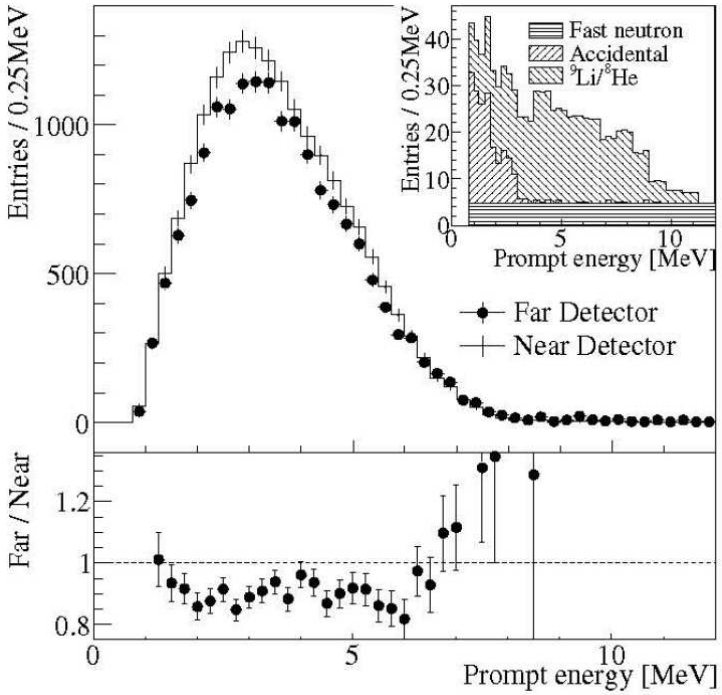

Figure 2.13: Energy spectrum obtained at tha Reno experiment. Spectrum in the far detector compared with the non-oscillation prediction from the measurements in the near detector.

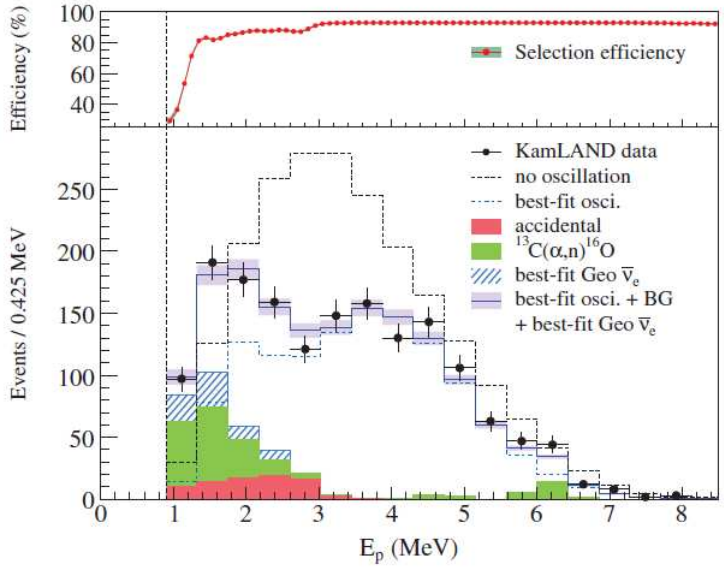

Figure 2.14: Energy sepctrum obtained at the KamLAND experiment with the best fit oscillation case.

2.4.2 KamLAND experiment

The KamLAND detector [22] is located in the Kamioka mine and consistsis of 1000 tons of organic liquid scintillator. The KamLAND experiment started data taking in 2002. The prompt scintillation light is emitted from the positron, while light from a 2.2MeV gamma ray is emitted when the neutron is captured by a proton. The KamLAND experiment had determined a precise value of the neutrino oscillation parameter Δm^2_{21} and placed stringent constraints on $\sin^2(\theta_{12})$ by directly observing distortion of the reactor $\bar{\nu}_e$ energy spectrum. For L/E around 15 km/MeV (so-called solar L/E), the survival probability of $\bar{\nu}_e$ is writtern as

$$P(\bar{\nu}_e \to \bar{\nu}_e) = cos^4(\theta_{13})(1 - sin^2(2\theta_{12})sin^2(1.27\Delta m^2_{21}L/E)) + sin^4(\theta_{13}). \quad (2.35)$$

The observed reactor energy spectrum from 2002 to 2007 is shown in Fig.2.14. The best fit value of each oscillation parameter is given by

$$\Delta m^2_{21} = 7.49^{+0.21}_{-0.19} \times 10^{-5} eV^2 \quad (2.36)$$
$$sin^2(\theta_{12}) = 0.309^{+0.40}_{-0.29}, \quad (2.37)$$

while using a fixed value of $\sin^2(\theta_{13})$=0.025, obtained from the statistical average of the short baseline experiments.

2.5 Physics of solar neutrino analysis in this thesis

The main physics goal of this thesis is the direct observation of the MSW effect. As explaind in section 2.3.3, the key measurements for this goal are the observations of a day/night flux

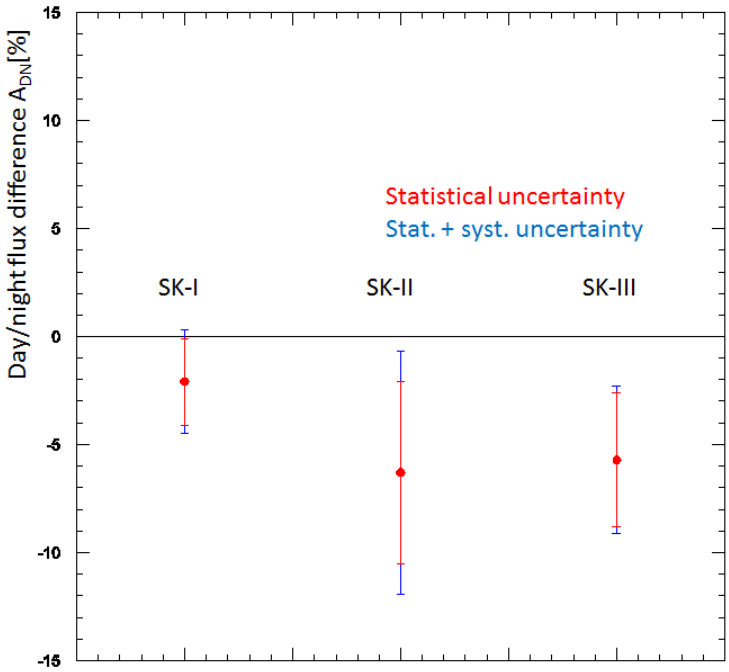

Figure 2.15: Day/night flux difference with statistical (blue) and systematic (red) uncertainties for SK-I, II, III. The 'straight' day/night value (see text) is used in this plot.

difference and a measurement of the energy spectrum distortion.

Fig.2.15 shows the observed 'straight' day/night flux difference for each Super-Kamiokande (SK) phase. The definition of SK phase is described in Chapter.3. The straight day/night flux difference is defined by

$$A_{DN}(\text{straight}) = \frac{\Phi_{day} - \Phi_{night}}{\frac{1}{2}(\Phi_{day} + \Phi_{night})}, \tag{2.38}$$

where Φ_{day} and Φ_{night} are observed fluxes using the daytime and the nighttime data, respectively

The tendency is that the night flux is larger than the day flux at about the 2-5% level, but the data is also still consistent with zero when taking into account statistical and systematic uncertainties. In order to get the combined value of all SK phases, a more sophisticated method is necessary because of the different systematic uncertainties for each SK phase. The main contribution of the systematic error comes from the directional dependence of the energy scale systematic uncertainties (∼1.2-1.3%), which was made by the position dependence of water quality in the SK detector. In the SK-III and SK-IV day/night analysis, this systematic uncertainty was greatly reduced, as shown in this thesis in the following chapters. Also, the combined day/night result of all SK phases using the sophisticated analysis method is presented.

Fig.2.16 shows the solar neutrino ν_e survival probabilities obtained from solar experiments. The flux of ^{7}Be (blue) and pep (red) neutrinos are used as the result for Borexino, ^{8}B neutrinos (green) are used as the result of Borexino+SNO-I,II (low-energy threshold analysis, LETA) [23] and ^{8}B neutrinos (black) are used as the result of SK+SNO. This figure also shows the MSW-LMA predicted survival probability as a function of neutrino energy. As shown in Fig.2.16, the

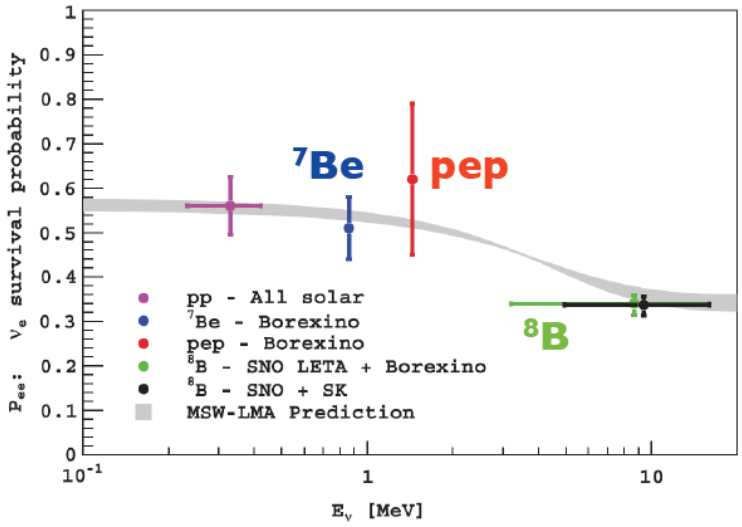

Figure 2.16: The global experimental constraints on the low energy solar neutrino ν_e survival probability (P_{ee}). The gray band shows the MSW-LMA prediction P_{ee} with the 1 σ range estimated in [24].

survival probability is expected to distort in the few MeV energy region, in the MSW-LMA model. The observed flux obtained by Borexino data (^{7}B and pep flux) validates the MSW-LMA prediction, but the transition point in the spectrum is not measured yet and there are some models which predict a shifting of the transition point. So, the spectrum measurement at a few MeV (3-6 MeV) is important. Fig.2.17 shows the observed energy spectrum in SK-III, with predicted energy distortion. As shown in the figure, it was still difficult to decide whether the observed spectrum was distorted or not due to the large statistical uncertainty for the lower energy bins and the large energy correlated systematic uncertainties for the higher energy bins. The large statistical uncertainty for the lower energy bins comes from the large amount of background. So, it is important to get data with a lower background rate, lower the threshold and lower the energy correlated systematic uncertainties, in order to observe the MSW effect from energy spectrum. SK has observed lower background data in the fourth phase (SK-IV) and systematic uncertainty was also improved. In this thesis, details of the SK-IV analysis are described. Also, by combining the energy spectrum of all SK phases, in which the correction of systematic errors are taken into account, the energy spectrum distortion is discussed in this thesis.

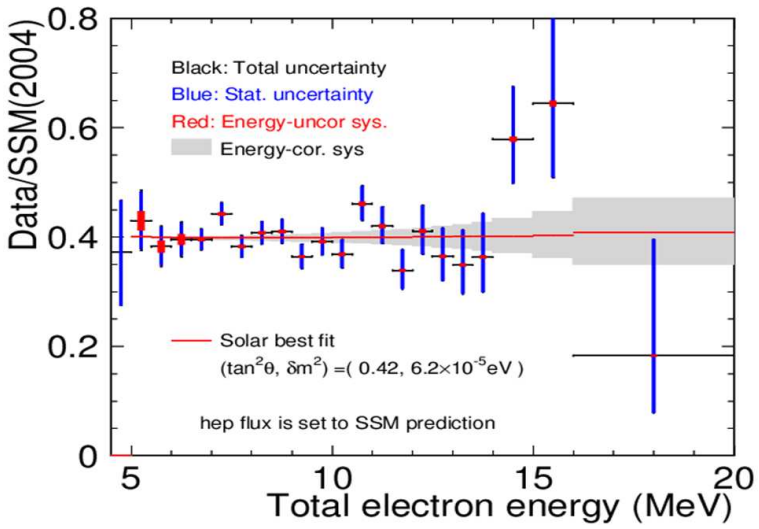

Figure 2.17: Observed energy spectrum/BP04 SSM, in SK-III phase. Horizontal axis shows the observed number of solar neutrino over expected number of solar neutrino which is simulated by solar neutrino MC for the flux of 5.79 $[\times 10^6/cm^2/s]$ (BP2004). The black points shows the fraction of data/SSM (Statistical uncertainty component in blue and energy-uncorrelated component in red) with energy-correlated systematic uncertainty(gray). The red line is a predicted energy spectrum distortion for given best fit oscillation parameters.

Chapter 3

The Super-Kamiokande Detector

3.1 SK detector

The Super-Kamiokande(SK) detector is a ring imaging water Cherenkov detector which consists of 50,000 tons of pure water and an array of photosensors. It is located 1000 m underground at Ikenoyama, Kamioka, Japan. This chapter describes the detection principle and components of the detector, i.e. photosensors, data acquisition system and the water circulation system.

3.1.1 Detection principle

In SK, solar neutrinos are detected by the neutrino-electron elastic scattering reaction.

$$\nu + e^- \rightarrow \nu + e^- \tag{3.1}$$

The advantages of the SK detector are as follows;

- With large amount of pure water, a large number of neutrino events are detected.
- The recoil electrons are scattered in the forward direction in the case of higher energy neutrinos, like ^8B solar neutrinos. The detection of the Cherenkov ring enables us to reconstruct the direction of the electrons, and so, the reconstructed events point back to the Sun.
- Real time detection: Events are observed at the time of interaction. It is quite useful to discuss time variation of the flux such as the day/night effect.
- The energy distribution of the recoil electrons are reflected by the energy spectrum of the incident neutrinos.

The cross section [29] of the reaction (3.1) is described as

$$\frac{d\sigma}{dT_e} = \frac{G_F^2 m_e}{2\pi}[A_0 + B_0(1 - \frac{T_e}{E_\nu})^2 + C_0\frac{m_e T_e}{E_\nu^2}] \tag{3.2}$$

$$\frac{G_F^2 m_e}{2\pi} = 4.31 \times 10^{-45}(\mathrm{cm}^2/\mathrm{MeV}),$$

where G_F, m_e, E_ν and T_e are the Fermi coupling constant, the electron mass, the incident neutrino enregy and the kinetic energy of the recoil electron, respectively. The parameters of A_0, B_0 and C_0 are defined as

$$\begin{aligned} A_0 = (g_V + g_A)^2, \quad B_0 = (g_V - g_A)^2, \quad C_0 = (g_A^2 - g_V^2), \\ g_V = 2sin^2\theta_W + \frac{1}{2}, \quad g_A = +\frac{1}{2} \quad \text{for} \quad (\nu_e), \\ g_V = 2sin^2\theta_W - \frac{1}{2}, \quad g_A = -\frac{1}{2} \quad \text{for} \quad (\nu_\mu), (\nu_\tau), \end{aligned}$$

where θ_W is the Weinberg angle, and using the latest results, $sin^2\theta_w$=0.2317 [15]. Fig.3.1 shows the differential cross section of the reaction (3.1) for an incident neutrino energy of 10 MeV. The horizontal axis shows the kinetic energy of the recoil electron (T_e). The radiative corrections of the one-loop electroweak, QCD and QED processes are also considered. These corrections reduce the relative probability of observing recoil electrons by about 4%, in our energy region. The details of the radiative corrections are also described in [15].

The total cross section as a function of incident neutrino energy is obtained by integrating equation (3.2) from 0 to T_{max}. T_{max} is limited by the incident neutrino energy and described as

$$T_{max} = \frac{E_\nu}{1 + \frac{m_e}{2E_\nu}}. \tag{3.3}$$

Fig.3.2 shows the total cross section of ν_e and those of ν_μ, ν_τ. The cross section of $\nu_{\mu,\tau}$-e scattering is approximately six times lower than that of ν_e-e scattering, because the ν_μ and ν_τ reaction occurs only through the neutral current, while ν_e interacts through both the charged and neutral currents.

The recoil electron energy distributon resulting from ^8B solar neutrino interactions is described as

$$F(T_e)dT_e = \left[\int_0^{E_{\nu,max}} \phi(E_\nu)\frac{d\sigma}{dT_e}dE_\nu\right] dT_e, \tag{3.4}$$

where $\phi(E_\nu)$ is the ^8B solar neutrino spectrum as shown in Fig.3.3. For the shape of the ^{8}B solar neutrino spectrum, we adopted the calculation based on the α-spectrum measurement of $^8B \rightarrow ^8 Be^* + e^+ + \nu_e$, $^8Be^* \rightarrow 2\alpha$ by Winter et al. [25]. The recoil electron energy spectrum is shown in Fig.3.4.

The angle between the directions of the recoil electron and the incident neutrino is given by

$$cos\theta = \frac{1 + m_e/E_\nu}{\sqrt{1 + 2m_e/T_e}}, \tag{3.5}$$

with the angular distribution of the recoil electrons given by

$$F(\theta)d\theta = \left[\int_0^{E_{\nu,\max}} \phi(E_\nu)\frac{d\sigma}{dT_e}\frac{dT_e}{d\theta}dE_\nu\right] d\theta. \tag{3.6}$$

These energy and angular distributions of the recoil electrons, which are described in (3.4) and (3.6), are used as the input to the Monte Carlo simulation of the ^8B and hep solar neutrinos. They are described in Sec.8.1.

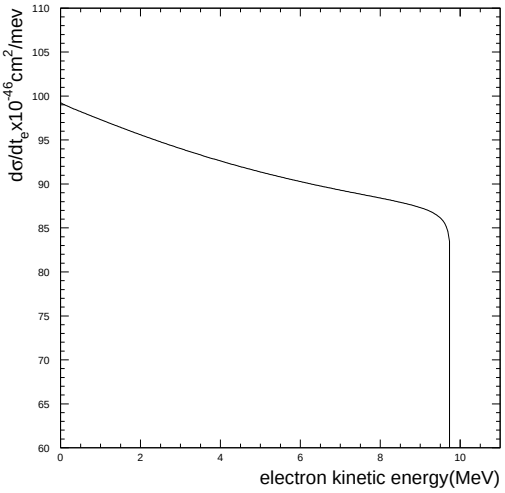

Figure 3.1: Differential cross section of ν_e-e scattering in the case of 10 MeV incident neutrino energy.

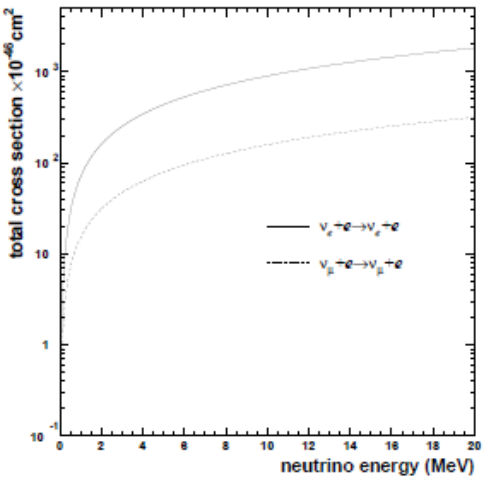

Figure 3.2: The cross sections of ν_e and ν_μ, ν_τ-e scattering as a function of incident neutrino energy

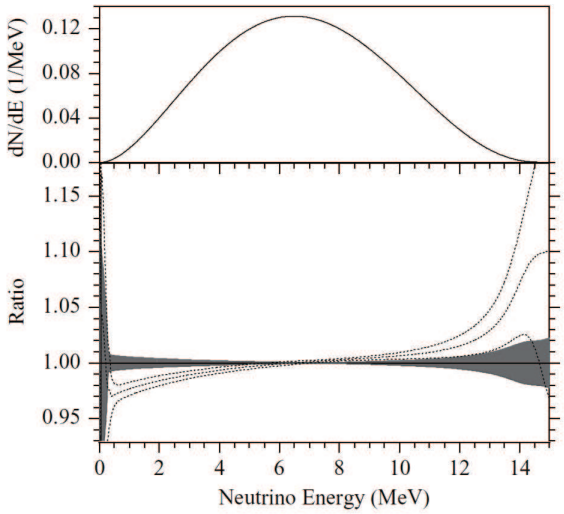

Figure 3.3: The upper figure shows the neutrino energy specturm measured by Winter [25]. The lower plot shows the experimental uncertainty of the Winter spectrum (black band) and the ratio between Winter spectrum and the Ortiz spectrum [26] and its $\pm 1\sigma$ experimental uncertainty (dashed line).

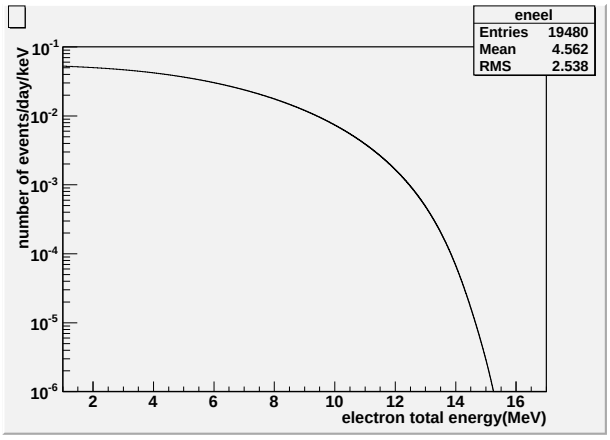

Figure 3.4: The total recoil electron spectrum observed with SK.

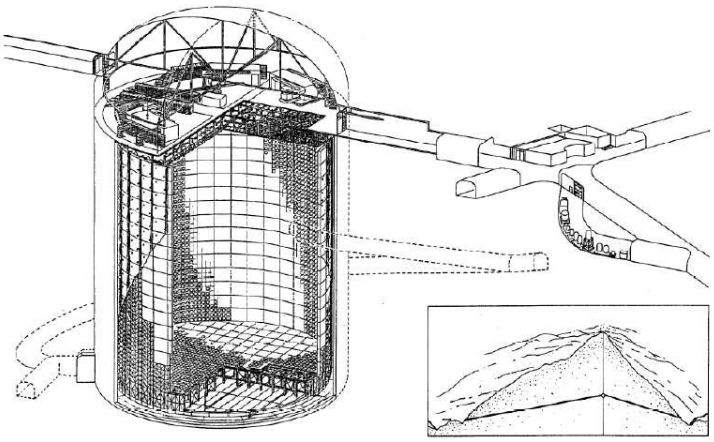

Figure 3.5: The SK detector

3.1.2 The Super-Kamiokande detector

SK is a cylindrical water Cherenkov detector with a 39.3 m diameter and a 41.4 m height. Fig.3.5 shows the overview of the SK detector. The last three characters of Super-Kamiokande stands for 'Neutrino Detection Experiment' and 'Nucleon Decay Experiment'. To reduce the backgrounds coming from cosmic ray muons, it is constructed at 1,000 m underground, which can reduce the rate of cosmic ray muon to 1/100,000, compared with that at the surface. The observed muon flux in the SK detector is about two Hz. The construction was started in 1991 and observation in April, 1996. SK has four phases, whose differences are photo-coverage, existance of PMT covers, front-end electronics and so on. The differencies is described in detail in section 3.1.4.

A PMT support structure, which is shown in Fig.3.6, divides the detector tank into two optically isolated volumes, which are called the inner detector (ID) and the outer detector (OD). The ID has about 32,000 tons of pure water and about 11,000 PMTs (the exact number is different for each SK phase). The wall of the ID tank, except for the PMT surfaces, is covered by black polyethylene terephthalate sheets to block the light from leaking from the OD and to reduce the effect of light reflections by the ID wall. The OD is an outer two meter layer from detector wall. The main purpose of the OD is to veto radioactive background, coming from the rock, and to tag cosmic ray muons. Totally 1885 eight inch PMTs are mounted at the OD wall facing outward. In order to increase the photon detection efficiency, a wave length shifting plate is mounted around each OD PMT. The inner surface of the OD region is covered by Tyvek sheets, except for the PMT surfaces, to further increase the light collection efficiency.

3.1.3 20 inch photomultiplier tubes

The 20 inch photomultiplier tubes (PMT), which are used in the ID and shown in Figs.3.7 and 3.8, were produced by Hamamatsu Photonics. The photo-cathode uses Bialkali (Sb-K-Cs) and has sensitivity between 300 and 600 nm wavelengths, which matches the Cherenkov light

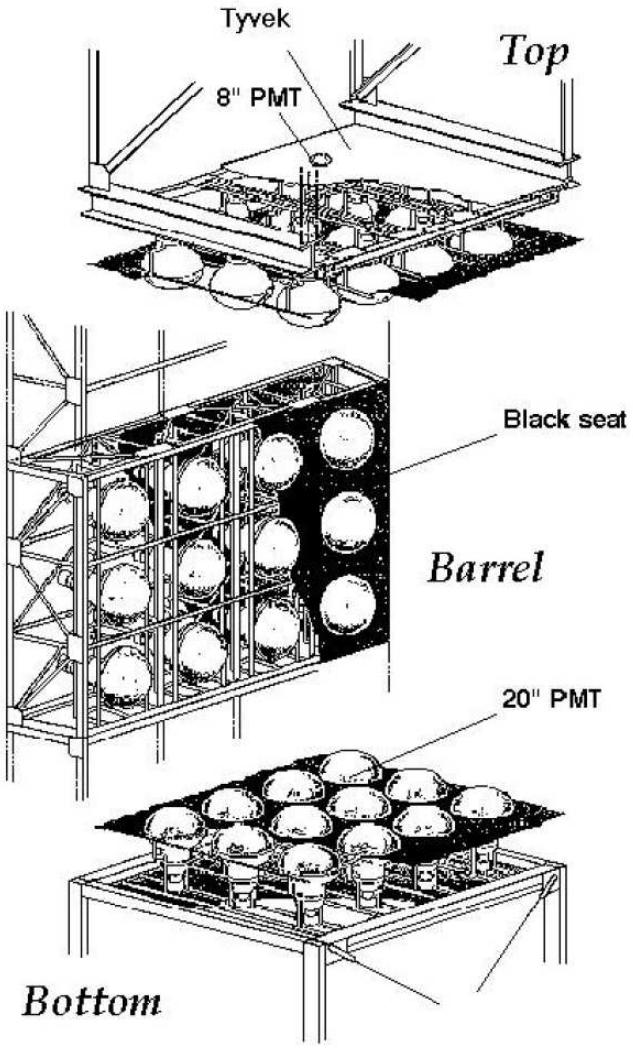

Figure 3.6: Schematic view of one unit of the PMT support structure. Thickness of the structure is about 55 cm. It holds twelve 20 inch PMTs for the inner detector and two eight inch PMTs for the outer detector.

Figure 3.7: Picture of a 20 inch, eight inch and five inch PMT.

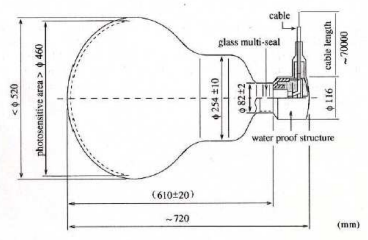

Figure 3.8: Schematic view of the 20 inch PMT.

after passage through the tank. The maximum quantum efficiency of the PMT is about 22% at 390 nm. Fig.3.9 shows the relationship of the Cherenkov light after traveling through 15 m of water and taking the quantum efficiency of the PMTs into account. The geo-magnetic field at the PMTs must be reduced to less than 100 mG, in order to keep uniform response throughout the dectecotr. A network of compensation coils surrounds the entire detector volume (the coil is attached on the tank wall). The geo-magnetic field is kept at less than 50 mG at each PMT position.

The interior of the PMT is vacuum to avoid discharge and to transport photo-electrons. As mentioned in Sec.3.1.4, all of the ID PMTs are enclosed in a protective case, consisting of an acrylic front and a Fiber Reinforce Plastic (FRP) back, which is shown in Fig.3.10 since the beginning of the SK-II phase. So if a PMT is accidentaly broken, it causes a strong shock wave which could in turn cause a chain reaction of exploding PMTs. The transparency of the front acrylic cover is more than 96% for photon wavelengths above 350 nm.

3.1.4 Phases of the SK detector

From April 1996, the SK detector started observation as the SK-I phase, with 11,146 ID PMTs and 1,885 OD PMTs. After 5 years of observation, in order to replace bad PMTs which have high dark noise, discarge in the dynodes, and so on, the SK-I observation phase was stopped. After the replacement work was finished filling of the tank with pure water was started in September 2001. When the water height became about ∼30 m in November 2011, one of the bottom PMTs was broken and the released shock wave triggered a chain reaction which destroyed 6777 ID PMTs and 1,100 OD PMTs.

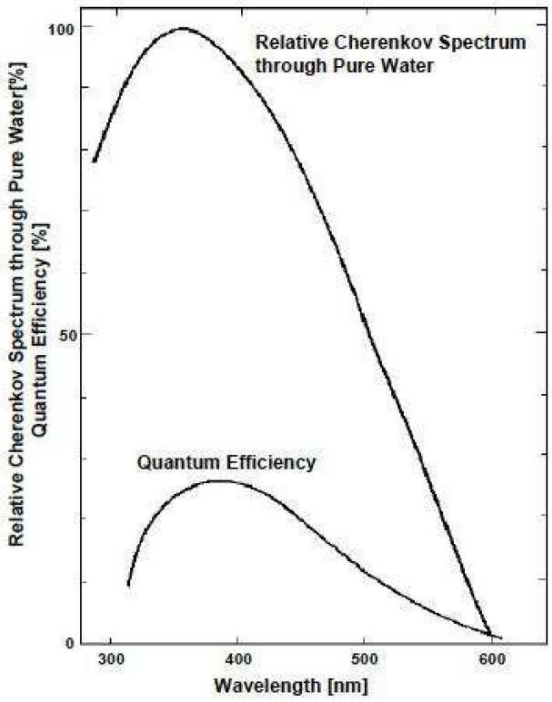

Figure 3.9: Spectrum of Cherenkov light and quantum efficiency of the 20 inch PMTs.

Figure 3.10: PMT case to prevent a chain reaction in the case of an imploded PMT.

SK phase	SK-I	SK-II	SK-III	SK-IV
Start	Apr.1996	Oct.2002	Jul.2005	Sep.2008
Finish	Apr.2001	Oct.2005	Aug.2008	continued
livetime	1496days	791days	548days	(1069days)
Number of ID PMT	11146	5182	11129	11129
Number of OD PMT	1885	1885	1885	1885
Photo coverage	40%	19%	40 %	40%

Table 3.1: Summary of the features of each SK phase. Livetime of SK-IV phase is from Sep. 2008 to Mar. 2012, used in this thesis.

After this accident, the detector was reconstructed using the surviving ID PMTs. Broken OD PMTs were all replaced by newly produced PMTs. After this reconstruction work in 2002, the SK-II period was started with 5,182 ID PMTs and 1,885 OD PMTs, in October 2002. As described before, all ID PMTs were each enclosed in a protective case to prevent another chain reaction, even if one PMT is somehow destroyed.

In order to recover the original number of ID PMTs, about 6,000 20 inch PMTs were reproduced from 2002 to 2005. A work to mount those PMTs, called the full-reconstruction, was conducted from October 2005 to July 2006. After this work, the SK-III phase was started with 11,129 ID PMTs.

The front end electronics and data acquisition system were replaced in September 2008, marking the beginning of the SK-IV phase. The data acqusition system during the SK-I,II,III phases and the new data acquisition system of SK-IV are described in the next section.

3.2 Data acquisition system

In this capter, the data acquisition systems are described. As described above, the data acquisition system is different between SK-I,II,III and SK-IV. The PMT signal is converted to digital signals, which contain charge and timing information, by the electronics system installed on top of the SK tank. For this purpose, there are 4 electronics huts and a central hut. In the electronics huts, the front-end electronics and the high voltage systems which supply high voltage to PMTs are contained. In the central hut, the trigger system and control electronics are present. A new type of trigger, special high energy trigger (SHE), are added in SK-IV for the study of Supernova Relic Neutrino (SRN) study. If the event has a SHE trigger and doesn't have an OD trigger, an After Trigger (AFT) is issued to take 500μsec data of after SHE trigger to detect the prompt positron and delayed 2.2MeV gamma event from neutron capture by proton which occurred from the inverse beta decay reaction. In September 2011, the SHE threshold was lowered from 70 to 58 hits to study the lower energy SRN candidate event.

3.2.1 Data acquisition system of SK-I,II,III

The layout of the data acquisition system of SK-I,II,III is shown in Fig.3.11. The front-end electronics (ATM, Analog Timing Module) were developed based on TKO (Tristan KEK Online)

standards. The integrated charge and timing information are digitized by an ADC (Analog to Digital Converter) on board the ATM module. One ATM module processed signals from 12 PMTs, so about 1000 ATM modules were used in total.

Fig.3.12 shows the schematic view of the input components of the ATM. Input signals were amplified 100 times and divided into four signals by the hybrid IC.

One of the divided signals would go through a discriminator, which had a threshold set to 100 mV, corresponding to about 0.32 photo-electrons. If this threshold was exceeded, two signals were generated. One signal was a pulse which has 200 nsec width and -15 mV height. These pulses of the input 12 PMT channels were then summed and output as a HITSUM signal. The HITSUM signal was used for generating a global trigger which was used to determine whether or not to save the event. This method of global trigger generation is described in the next subsection. Another signal was a pulse of 900 nsec width and -15 mV height, and this pulse was called the selfgate signal. The selfgate signal was used as the trigger to start the QAC and TAC integration, as described below.

The other two divided signals were sent to a QAC (charge to analog converter), which integrated the charge for 400 nsec and to a TAC (time to analog converter), which generated the hit timing. If a global trigger was generated within 1.3μ sec, the integrated QAC and TAC information was digitized by an ADC.

The final divided signal was output as a PMTSUM signal. The PMTSUM is the sum of the input PMT signals, for one ATM board, and was run into a Flash ADC that recorded the waveform information.

3.2.2 Hardware trigger

The HITSUM signals from the ATMs were eventually summed at the centeral hut, and a global trigger generated. The reason why the HITSUM signal had a 200 nsec width is that the event duration time in the SK detector is up to 200 nsec, which is corresponded the time of flight would take to go from one edge of the detector to other edge. If the summed HITSUM signal exceeded a threshold, a global trigger was generated. The overview of the global trigger generation is shown in Fig.3.13.

There were, and still remain, three levels of the global trigger, called the High Energy trigger (HE), the Low Energy trigger (LE) and the Super Low Energy trigger (SLE). These triggers were determined by the threshold of the summed HITSUM, with each trigger threshold, for each SK phase, and are summarized in Table 3.2.

	SK-I	SK-II	SK-III
SLE	186mV(*)	110mV	186mV
LE	320mV	152mV	302mV
HE	340mV	180mV	320mV

Table 3.2: Trigger threshold in each data taking period. The SLE threshold was lowered time to time during SK-I. The final value is shown here.

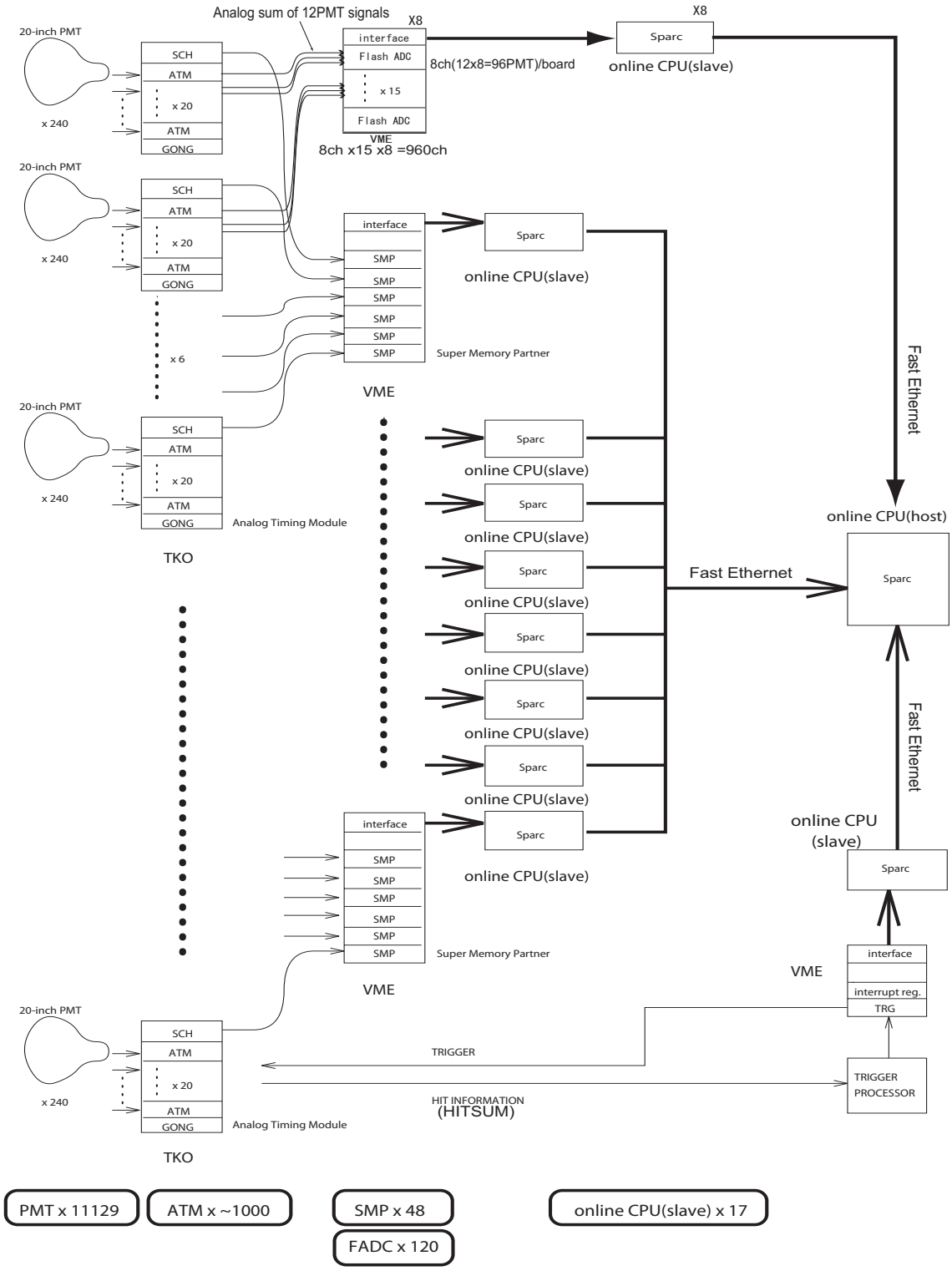

Figure 3.11: The layout of the data acquisition system of SK-I,II,III.

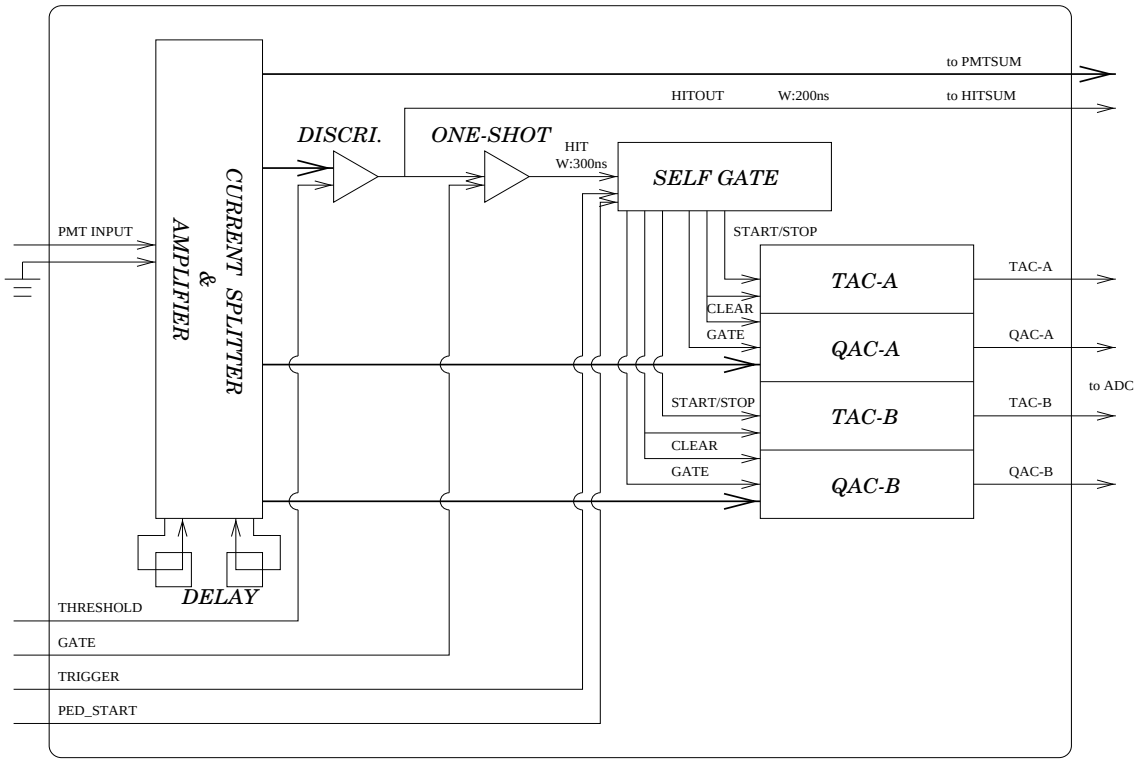

Figure 3.12: The schematic view of the input components of the ATM.

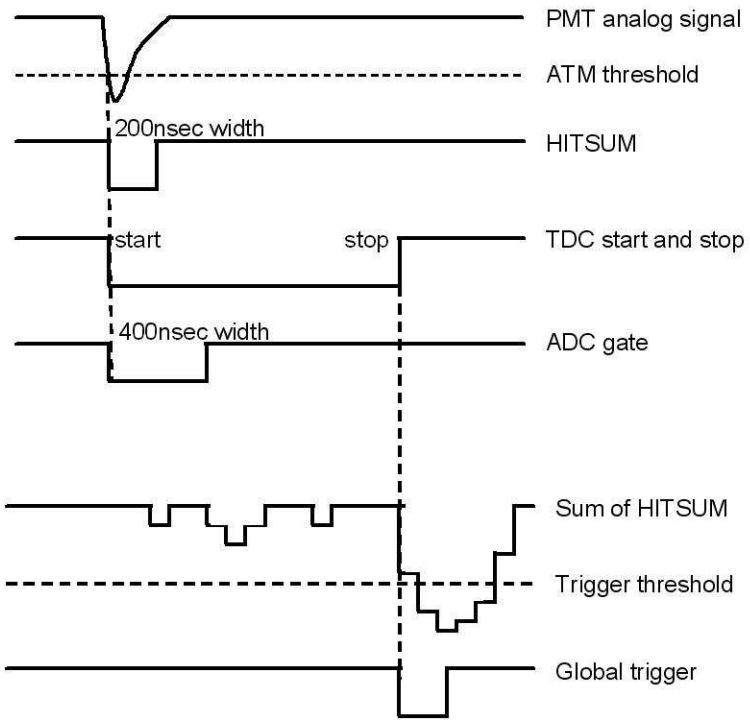

Figure 3.13: The overview of the global trigger generation.

3.2.3 Data acquisition system of SK-IV

Fig.3.14 shows the block diagram of the data acquisition system of SK-IV.

To achieve stable observation for the next 10∼20 years, and to improve the sensitity of the detector, new front-end electronics, called QBEEs (QTC-Based Electronics with Ethernet), were installed in September 2008, and marked the start of the SK-IV phase. Fig.3.15 shows a picture of one QBEE. The QBEEs are housed in TKO crates, re-used from the SK-I, II, III setup, while the readout scheme is completely different, as described below. One QBEE module processes signals from 24 PMTs. Fig.3.16 shows the block diagram of signal processing in the QBEEs. The essential components on the QBEE for the analog signal processing and digitization are the QTC (Charge-to-Time Converter) ASIC [28] and the multi-hit TDC, respectively.

The QTC detects the PMT signals and drives output timing signals whose width represents the integrated charge of the PMT signal. To satisfy the physics requirements of keeping good charge resolution at a few photo-electron level signal, and of setting a larger dynamic range compared with the old front end electronics (ATM), the QTC has three input channels which are called the small, medium and high gains. These gains are set to 1, 1/7 and 1/49. The characteristics of each input channel are summarized in Table 3.3. The overall charge dynamic rang is 0.2 pC to 2500 pC, which is about 5 times wider than that of the ATMs. The charge integration gate is set to 400 nsec.

The output signal from the QTC is sent to a multi-hit TDC. The TDC measures the width of the QTC output pulse by detecting the leading and trailing edges. A Field Programmable Gate Array (FPGA) reads and processes the data stored in the TDC, with the width information dig-

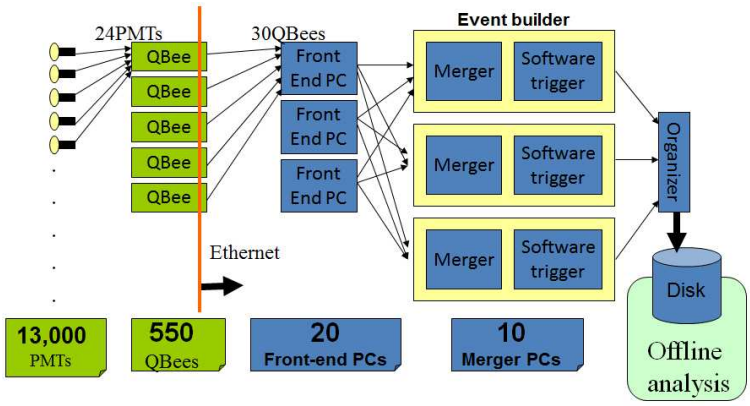

Figure 3.14: The block diagram of the DAQ system of SK-IV.

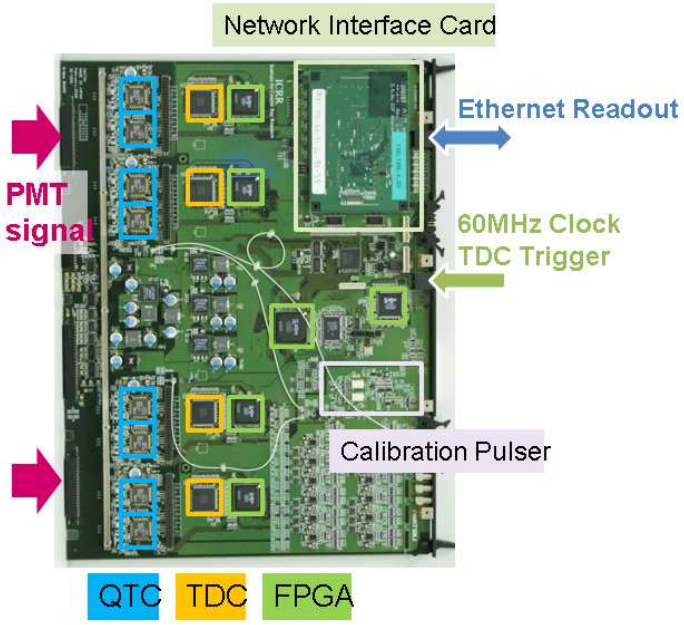

Figure 3.15: Picture of the new QBEE electronics.

input channel	observable charge range	charge resolution
Small	0∼51[pC]	0.1[pC/count](∼0.05[p.e./count])
Medium	0∼357[pC]	0.7[pC/count](∼0.35[p.e./count])
Large	0∼2500[pC](∼1250[p.e.])	4.9[pC/count](∼2.5[p.e./count])

Table 3.3: The characteristics of each input channel.

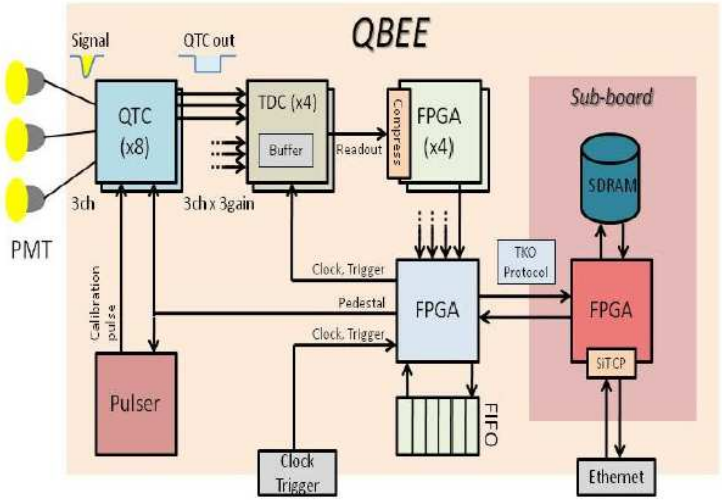

Figure 3.16: The block diagram of the signal processing in the QBEEs.

itized to charge infromation and the arrival timing inforamtion digitized to timing information. The digitized signal is sent to the front end PCs via ethernet. The charge and timing resolution of the QBEEs, for the single photo-electron level signal, are 10% and 0.3 nsec, respectively. Both resolutions are better than the intrinsic resolutions of the 20 inch PMTs. Furthermore, the QBEEs achieved high-seed signal processing by combining the pipelined components of the QTC, TDC and FPGA.

Data from the QBEE boards is sent to the front-end PCs. The front end PCs sort the received data by time and then send it to the Merger PCs. In the Merger PCs, a software trigger program, which is described in detail in the next section, is run to extract an event from all the hit data, from all PMTs. The triggered event data are collected by the organizer PC and recorded to disk.

3.2.4 Software trigger

Because of the achievement of high-speed signal digitization, all of every hit PMT's information of all of hit PMTs is collected at the Merger PC. The software trigger searches for events which have an $N_{hit,200ns}$ (number of hits within a 200 nsec sliding time window) threshold. The $N_{hit,200ns}$ threshold for each trigger type is summarized in Table 3.4. The key feature of the software trigger is that it is possible to select an event width dependent upon trigger type. In SK-I,II,III, the width was always 1.3 μsec, because of the hardware trigger, while in SK-IV the events with LE/HE trigger types have a width of 40 μsec. The wider event width is ideal for detecting possible pre-activity (i.e. prompt γ rays) and post-activity (i.e. μ decay electrons). The events with SLE trigger type have a width of 1.5 μsec, because of its high rate due to radioactive backgrounds. It is possible to tag external triggers for calibration events and now simpler to program to Monte Carlo simulation. The systematic error of the trigger threshold of SK-IV has been reduced compared with SK-I,II,III, and is described in chapter 7.

trigger type	hit threshold[hits/200nsec]	event width[μsec]
SLE	34	1.5(-0.5∼+1.0)
LE	47	40(-5∼+35)
HE	50	40(-5∼+35)
SHE	70(before Sep.2011)	40(-5∼+35)
SHE	58(after Sep.2011)	40(-5∼+35)

Table 3.4: Summary of software trigger types with SK-IV.

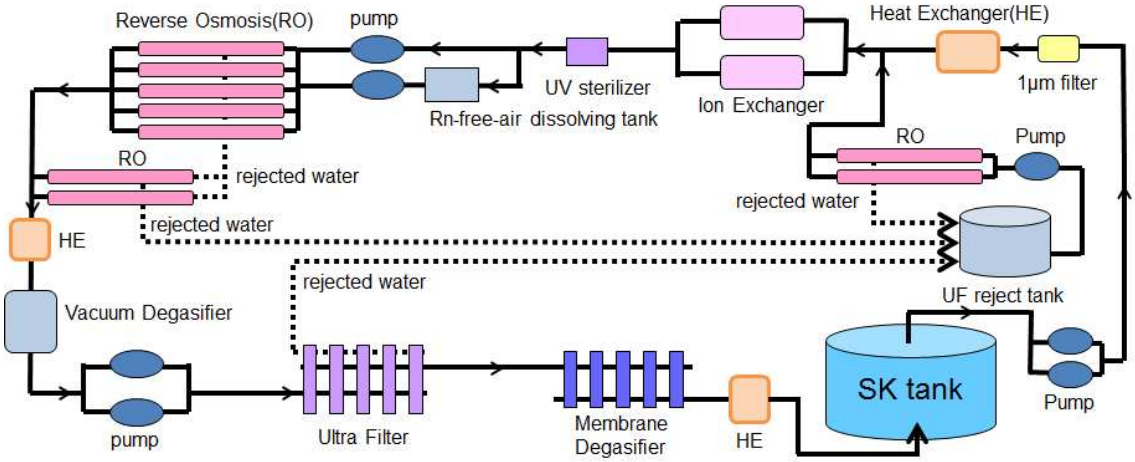

Figure 3.17: Schematic view of the water purification system.

3.3 Water circulation system

The water in the detector is continuously circulated through the water purification system with a flow rate of about 60 tons/hour. In this section, the water purification system and its important improvements during the SK-III and IV phase are described.

3.3.1 Water purification system

The schematic view of the SK-IV water purification system is shown in Fig.3.17. The water purification system consists of the following components;

- 1 μm filter: Remove dust ($\sim$1μm) and particles.
- Heat exchanger (HE): The water temperature rises due to the heat geneated by pumps, PMTs, surrounding rock and so on. The temperature of the supply water is controlled with an accuracy of 0.01°C, to suppress the convection inside the detector. The processed water temperature is about 13°C, and is low enough to supress bacteria growth. This water temperature control is only one of the improvements in SK-IV, and is described in details in the next section.

- Ion exchanger: The resin for the high molecular, three dimensional network structure within the ion exhange group. It is able to remove heavy ions such as Na^+, Cl^-, Ca^{2+} and ^{218}Po.
- UV sterilizer: Kill bacteria by ultraviolet light.
- Radon(Rn)-free-air dissolving system: Dissolving the Rn free air into the water increases the efficiency of the Rn removal by the vacuum degasifier.
- Reverse Osmosis filter (RO): Remove contaminants heavier than 1000 molecular weight. The RO is newly added during the SK-III phase.
- Vacuum degasifier: Remove gas components dissolved in the water. The main purpose is to remove Rn. It is able to remove about 99% of oxygen and 96% of radon.
- Ultra Filter (UF): Removes small particles, down to the size of 10 nm.
- Membrance Degasifier: Remove radon with 83% efficiency.

3.3.2 Water circulation

Fig.3.18 shows the water circulation mode in the detector. The purified water from the water purification system is supplied at the bottom of the ID detector and extracted from the tank at the top of the ID and the edge of the OD. The detector has been running with this configuration since August 2007 (during SK-III).

In addition, the new control system for the supply water temperature was installed in November 2009 (during SK-IV). This system can control the temperature within 0.01°C. Fig.3.19 shows the time dependence of the supply water temperature. The rate of convection due to the different supply water temperature is kept much lower. The reason the water circulation is designed to reduce convection is in order to reduce radon emanating from the PMT surface glass. Convection transports such radon to the fiducial volume of the detector. The lowering of the background level in the central region of the detector is discussed in chapter 6.

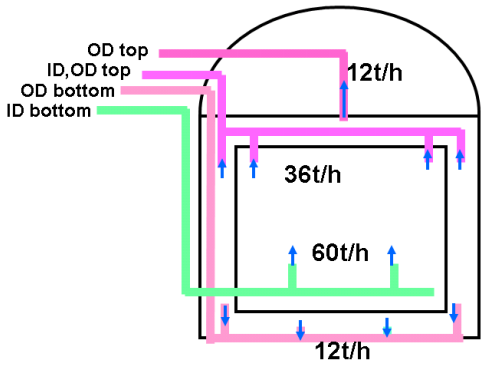

Figure 3.18: The water circulation mode.

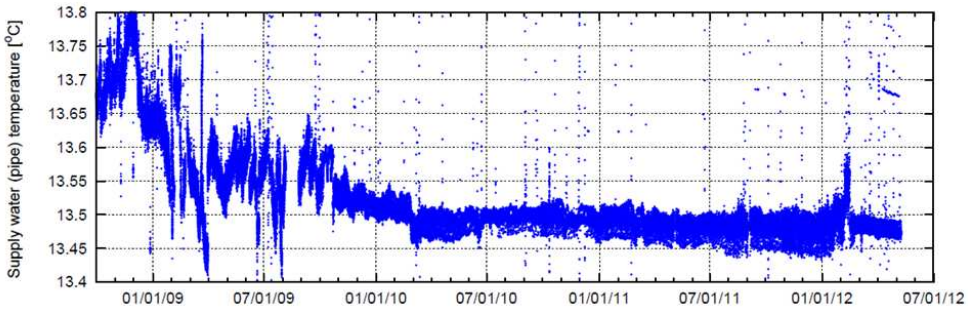

Figure 3.19: Time dependence of the supply water temperature. In January 2010 the new temperature control system was installed.

Chapter 4

Event Reconstruction

In this chapter, the reconstruction of solar neutrino events of SK-IV is described. Super-Kamiokande observes solar neutrino events by detecting the Cherenkov light coming from the recoil electron of the ν-e elastic scattering. Because the observed recoil electron travels only $\sim$10 cm, it is treated as a point-like source. The observed light at each hit PMTs is close to one photo-electron, and because the one photo-electron level charge information does not tell the absolute light deposit, only the timing information of the hit PMTs is used for event reconstruction. In the event reconstruction, the vertex of the point-like source is reconstructed first. Next, the direction and energy are reconstructed. Because the direction and energy are related to each other, the direction and energy reconstructions are iterative.

4.1 Vertex reconstruction

Low energy charged particles, such as recoil electrons coming from solar neutrino interactions, travel about 10 cm. Because of the large size of SK detector and its vertex resolution, the reconstructed vertex is treated as a point-like source. For the vertex reconstruction, a maximum likelihood fit to the timing residuals of the Cherenkov signal is used. This vertex reconstructed tool is called BONSAI (Branch Optimization Navigating Successive Annealing Iterations) [30]. The definision of the likelihood is as follows;

$$\mathcal{L}(\vec{x}, t_0) = \sum_{i=1}^{Nhit} \log(P(t - tof - t_0)), \tag{4.1}$$

where $\vec{x}$ is the testing vertex, t is the observed time for each PMT, tof is the time of flight from the test vertex ($\vec{x}$) to each hit PMT, t_0 is the time offset of the vertex position, and the function P is a probability density function which describes the function of timing for a single photoelectron signal. This probability density function is obtained from LINAC calibration which is described in section 5.1.5, and is shown in Fig.4.1. Fig.4.2 shows the vertex resolution as a function of recoil electron energy. The vertex resolution of SK-IV is slightly better than that of SK-III, because of the front end electronics replacement and better timing calibration which is described in Section 5. The vertex resolution for 10 MeV electrons is $\sim$70 cm.

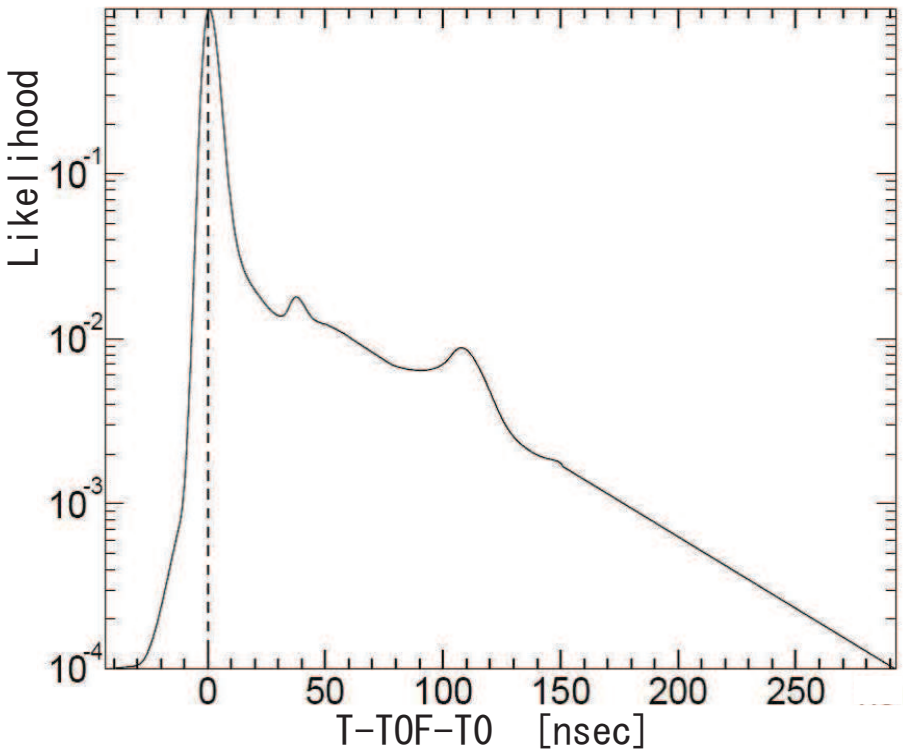

Figure 4.1: Probability density function of the residual times used in the vertex reconstruction program. Second and third peaks around the 30 nsec and 100 nsec are caused by after pulses of the PMTs.

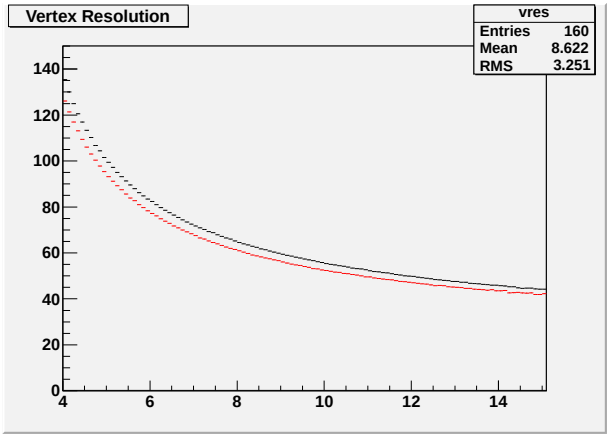

Figure 4.2: Vertex resolution as a function of energy. The vertex resolution is defined as the point which contains 68% of events when comparing the real vertex and the reconstructed vertex. Red shows SK-IV, while black shows SK-III. Horizontal axis is the input recoil electron energy.

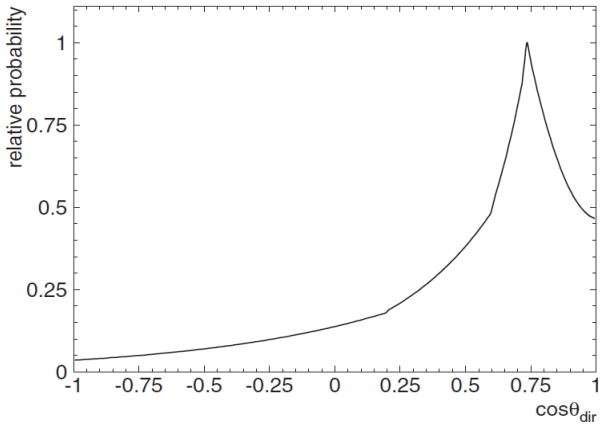

Figure 4.3: The angular likelihood function for 10 MeV electrons. The vertical axis shows a relative probability normalized to one at the maximum. The peak of this distribution is at θ_{dir} =∼42 degrees.

4.2 Direction reconstruction

For the direction reconstruction, a maximum pattern likelihood fit with the Cherenkov ring pattern is used. The definition of the likelihood is as follows;

$$\mathcal{L}(\vec{d}) \equiv \sum_{i}^{N_{20}} \log(f_{dir}(\cos\theta_{dir,i}, E))_i \times \frac{\cos\theta_i}{a(\theta_i)}, \tag{4.2}$$

where $\vec{d}$ is a testing particle direction, N_{20} is number of hit PMTs within a 20 nsec timing window around the residual timing($t - tof - t_0$), θ_{dir} is the expected opening angle distribution between the vector from the vertex to each PMT and $\vec{d}$. Because the magnitude of the multiple coulomb scattering depends on particle momemtum, the probablity density function of opening angle (f_{dir}) should be energy dependent. The energy dependence of f_{dir} is generated using the mono-energetic electron MC. As an example, Fig.4.3 shows the likelihood function for 10 MeV electrons and Fig.4.4 shows energy dependence of the angular likelihood function.

The term of $\frac{\cos\theta_i}{a(\theta_i)}$ is the correction for the PMT acceptance. θ_i is photon incident angle, and $a(\theta_i)$ is the acceptance function which is shown in Fig.4.5. The angular resolution as a function of energy is shown in Fig.4.6. For 10 MeV electrons, the angular resolution is about 25 degrees.

4.3 Energy reconstruction

The basic idea of the energy reconstruction is that the energy deposited by a charged particle is approximately proportional to the number of hit PMTs. Before converting from the number of hit PMTs to reconstructed energy, several corrections, which are described in equation (4.3), are applied, and the result is called the number of effective hits, N_{eff};

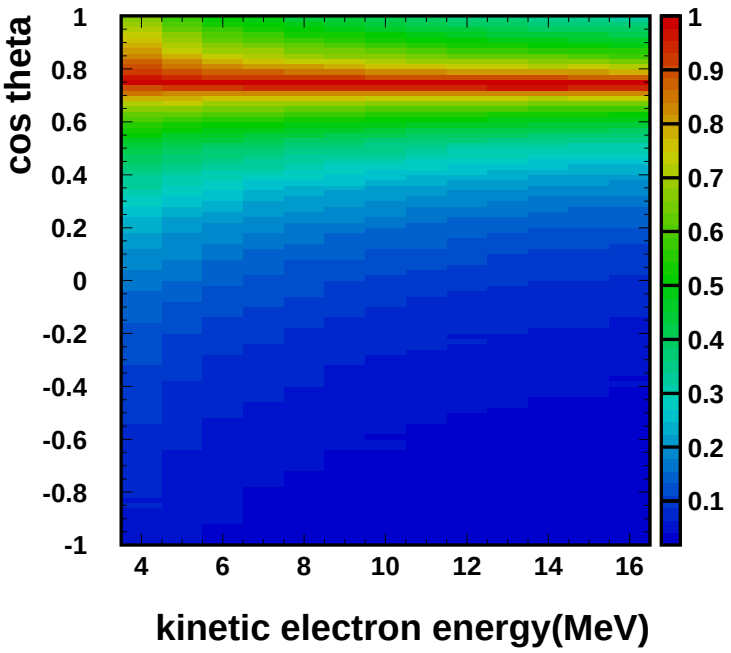

Figure 4.4: The energy dependence of the angular likelihood.

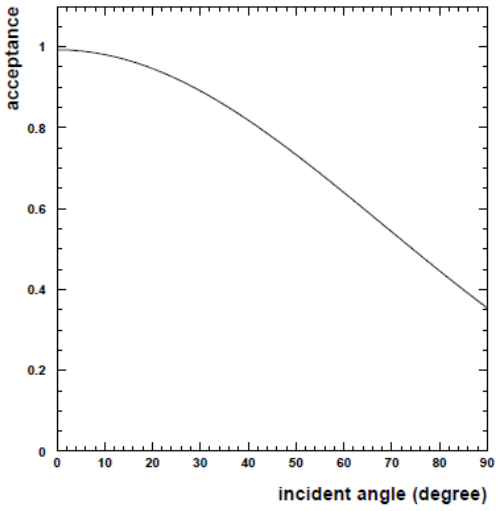

Figure 4.5: The incident angle dependence of the PMT acceptance.

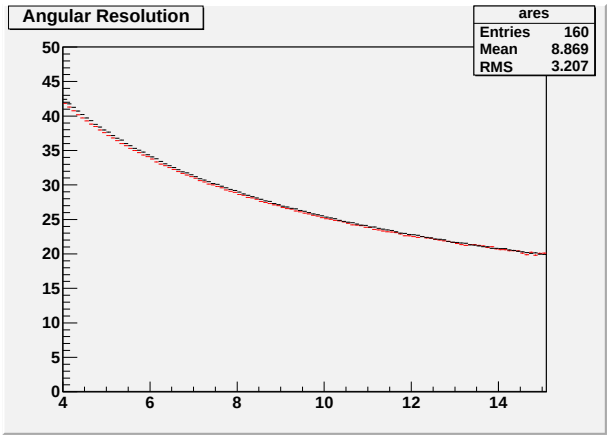

Figure 4.6: The angular resolution as a function of energy.

$$N_{eff} = \sum_{i}^{N_{50}} \left\{ (X_i + \epsilon_{tail} - \epsilon_{dark}) \times \frac{N_{all}}{N_{alive}} \times \frac{1}{S(\theta_i, \phi_i)} \times \exp(\frac{r_i}{\lambda(run)})/QE_i \right\}. \tag{4.3}$$

Items in N_{eff} are as follows;

- N_{50}: Number of hit PMTs

  N_{50} is the maximum number of hits within a 50 nsec timing window, after subtracting the time of flight.

- X_i: Multi photo-electron hit correction

  Although the majority of hit PMTs observe a single photo-electron, in the case of event occurring near the wall or towards the wall, there is the possibility that the hit PMT will observe multiple photo-electrons because there is not enough distance between the interaction vertex and the PMTs to spread the Cherenkov light. X_i is a factor to correct for the multiple photo-electron effects. It is defined as

$$X_i = \begin{cases} \frac{\log \frac{1}{1-x_i}}{x_i}, & x_i < 1 \\ 3.0, & x_i = 1 \end{cases} \tag{4.4}$$

  where x_i is the fraction of hit PMTs of the surrounding PMTs around the i-th hit PMT. If the i-th hit PMT detects multiple photons, many PMTs surrounding the i-th PMT are also hit. In the case of x_i=1, for all surronding PMT hits, X_i are assigned to 3, and in the case of $x_i < 1$, using Poisson statistics X_i is defined as equation (4.4).

- ϵ_{tail}: late hits correction

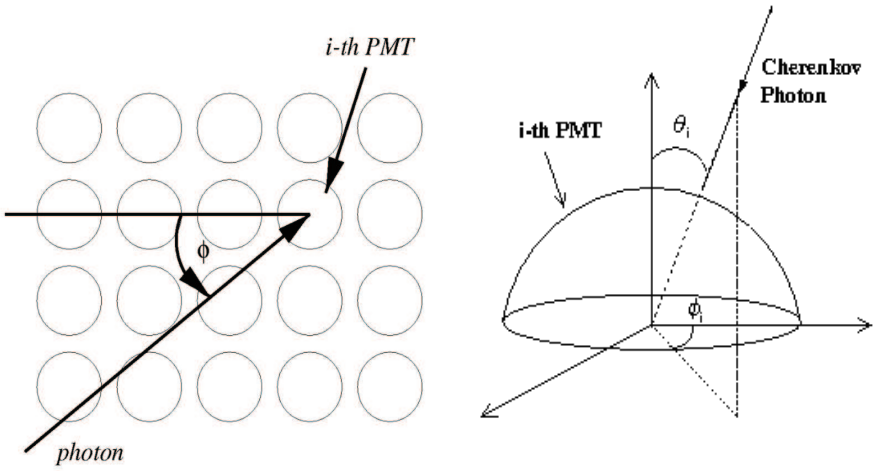

Figure 4.7: The definitions of (θ_i, ϕ_i).

Some Cherenkov lights are observed outside of the 50 nsec timing window, due to scattering in water or reflection on the inner surface of the detector. The correction of ϵ_{tail} is defined as

$$\epsilon_{tail} = \frac{N_{100} - N_{50} - N_{alive} \times R_{dark} \times 50nsec}{N_{50}}, \tag{4.5}$$

where N_{100} is the maximum number of 100 nsec timing window. As described in the next item, dark rate effects are subtracted out of the 50 nsec timing window.

- ϵ_{dark}: dark noise hits correction

  The correction of ϵ_{dark} is defined as

$$\epsilon_{dark} = \frac{N_{alive} \times R_{dark} \times 50nsec}{N_{50}}, \tag{4.6}$$

  where N_{alive} is the number of all live PMTs. For each run, the average dark noise rate (R_{dark}) is measured. The average for SK-IV is ∼4.5kHz.

- $\frac{N_{all}}{N_{alive}}$: Dead PMT correction

  There is a time variation in the number of dead PMTs, where N_{all} is the total number of PMT, which is 11,129 for SK-IV. N_{alive} is the total number of alive PMTs. The correction is to multiply by the ratio of $\frac{N_{all}}{N_{alive}}$.

- $\frac{1}{S(\theta_i,\phi_i)}$: Photo-cathode coverage correction

  The correction for direction dependence due to PMT photo-cathode coverage. The definitions of θ_i and ϕ_i are shown in Fig.4.7. $S(\theta_i, \phi_i)$ is the effective photocathode area for the angles (θ_i, ϕ_i), which is shown in Fig.4.8.

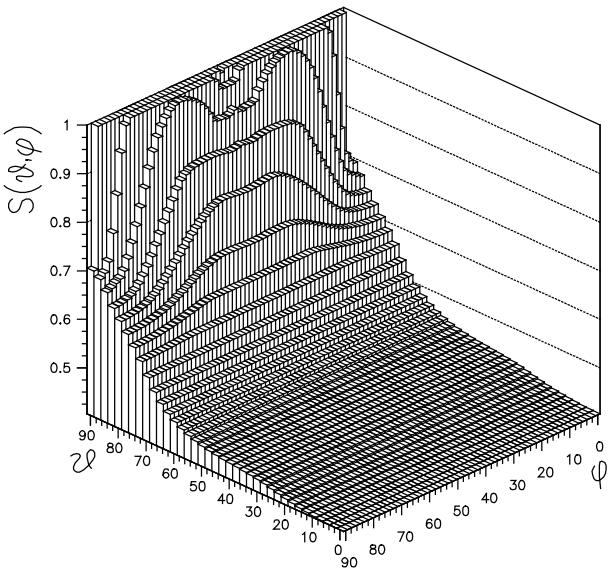

Figure 4.8: The function of $S(\theta_i, \phi_i)$, photo-cathode coverage correction factor.

- $\exp(\frac{r_i}{\lambda(run)})$: Water transparency correction

  The correction for the effect of the water transparency, where r_i is the distance between the reconstructed vertex and the i-th PMT and $\lambda(run)$ is the water transparency measured with $\mu \rightarrow$e decays, which is described in Sec.5.3.

- QE_i: PMT quantum efficiency correction

  The correction for PMT quantum efficiency (QE). The QE for each PMT is described in section 5.2.2.

The event energy is calculated using the function of N_{eff}. This 'N_{eff} to MeV' converted function is obtained by a Monte Carlo simulation. Fig.4.9 shows the obtained relationship between N_{eff} and the reconstructed energy. The best fit result of the converted fitted function is

$$0.82 + 0.13 \times N_{eff} - 1.11 \times 10^{-4} \times N_{eff}^2 + 1.25 \times 10^{-6} \times N_{eff}^3 - 3.42 \times 10^{-9} \times N_{eff}^4. \quad (4.7)$$

This function is applied below 25 MeV, which corresponds to $N_{eff} < 189.8$. Above 25 MeV, the N_{eff} vs. energy relationship is fit with a one-demensional polynomial funciton, described as

$$25.00 + 0.138 \times (N_{eff} - 189.8). \quad (4.8)$$

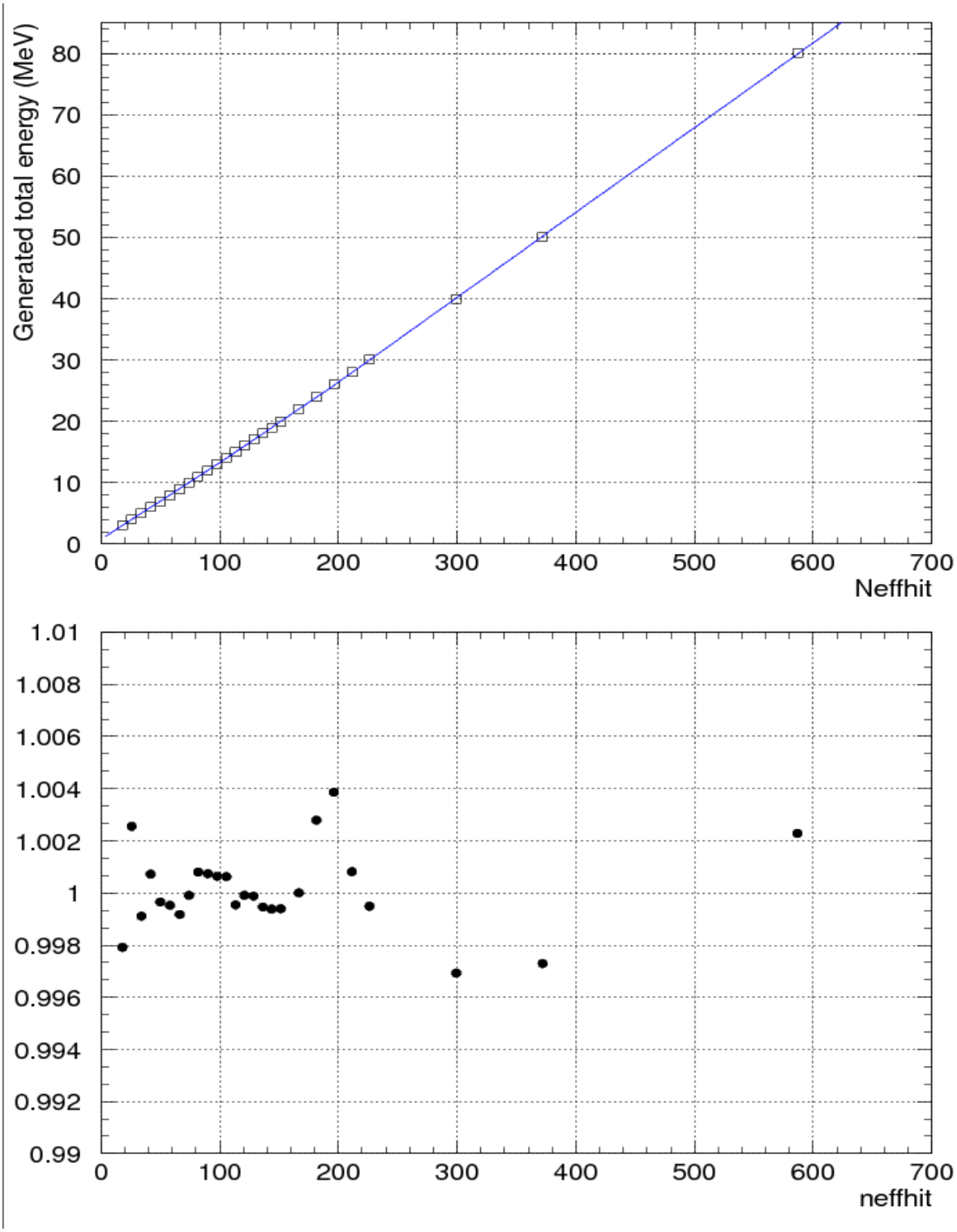

Figure 4.9: The relationship between N_{eff} and energy. The upper figure shows the fitted result and the lower figure shows the ratio between the simulated point and the fitted function.

Chapter 5

Detector Calibration

The details of the detector calibration are described in this chapter. Super-Kamiokande consists of about 11,000 20-inch PMTs and 50 kton of pure water. Many calibrations are done for the PMTs and the pure water. As described in chapter 3, event reconstruction is based on PMT response, especially the timing information. The PMT gain and quantum efficiency measurements were done during the SK-III phase, and these quantities are essentially unchanged with the replacement of the front-end electronics. However, several calibrations, such as PMT timing calibration, water transparency measurements and absolute energy scale calibration were redone after installation of the SK-IV electronics. Details of the calibration sources, input parameters for Monte Carlo (MC), and trigger efficiency measurements are also described.

5.1 Calibration sources

To acquire accurate information from the PMTs and to measure and monitor water conditions and so on, the SK group has developed many calibration sources. In this section, details of these calibration sources are described.

5.1.1 Nickel source

The nickel source is a gamma ray source, which emits high energy gamma rays when a thermal neutron is captured by the nickel through the reaction $Ni^n(n,\gamma)^{n+1}Ni$. As a neutron source, the spontaneous fission source of ^{252}Cf, shown in left of Fig.5.1, is used. ^{252}Cf decays through $\alpha-$decay ($\sim 96.9\%$) and spontaneous fission ($\sim 3.1\%$) with a multiplicity of 3.8 neutrons. The half life of ^{252}Cf is 2.65 years.

The ^{252}Cf source is set at the center of the so-called 'nickel ball', shown in the right portion of Fig.5.1. A pair of brass rods support the ^{252}Cf source within the ball, shown in the middle portion of Fig.5.1. The nickel ball consists of 3.5 kg of polyethylene and 6.5 kg of NiO. The accuracy of the uniformity of the nickel ball is within 1%. Table 5.1 shows the isotope abundance ratio, neutron capture cross-section and the most frequently emitted gamma energies of the different nickel isotopes.

The characteristics of the nickel source is very stable for weak Cherenkov light, emitting this light uniformly and an ease of taking the data. It is useful for calibrations which need stable light at the one photon level, such as determining the absolute gain and quantum efficiency of

Reaction	isotope abundance [%]	capture cross-section [barns]	Sum of all γ energy [MeV]
$^{58}Ni(n,\gamma)^{59}Ni$	67.88	4.4	9.000
$^{60}Ni(n,\gamma)^{61}Ni$	26.23	2.6	7.820
$^{62}Ni(n,\gamma)^{63}Ni$	3.66	15	6.838
$^{64}Ni(n,\gamma)^{65}Ni$	1.08	1.52	6.098

Table 5.1: Characteristics of neutron capture on a nickel nuleus.

Figure 5.1: The picture of the Cf source (left), the brass rod (middle), and the nickel ball (right)

each PMT. It is also used for checking the trigger efficiency, checking the water conditions and its position dependence and the quality of vertex reconstruction.

5.1.2 Xenon light source

The xenon light source was made by Hamamatsu Photonics, and has a stability of output intensity better than 5%. The Xe lamp light goes through a UV filter, which passes only UV light, and is then divided into two optical fibers. One goes into a scintillator ball set inside the SK tank, while the other goes to a two inch PMT monitor, shown in Fig.5.2. Looking at a spectrometer measurement, only light with wavelength less than 400 nm is transmitted to the fibers. The characteristics of the xenon light source are its high stability and strong light yield. Therefore, it is used for the PMT gain calibration and continuous monitoring of the water conditions.

5.1.3 Laser light source for timing calibration

The characteristic of the laser light source is its very short pulse width. First, an N_2 laser generates 337 nm light, with a very short pulse ($< 0.4nm$), and using a dye it converts the wavelength from 337 nm to 398 nm, which is near the peak of the Cherenkov spectrum seen in SK. Then, the light is transported into the SK tank via optical fiber, and then semi-uniform light is emitted with a diffuser ball.

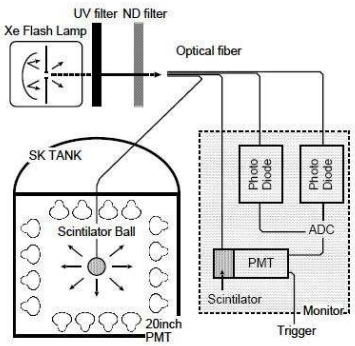

Figure 5.2: Schematic view of the set up of the Xe light source.

USHO Laser

The USHO (Usho Optical Systems Co.) laser is used for making the TQmap. While this laser requires N_2 gas flow during operation time, it emits shorter pulses of light compared with other light sources. The characteristics of the USHO Laser are as shown in Table 5.2. The USHO laser is used for the precise PMT timing calibration, which is described in section 5.2.3. Although the pulse time width is very short, its longer time stability is not good. So other laser light sources are needed for the long term stability check of PMT timing.

USHO N_2 laser	
Wevelength	337.1nm
Max. rate	20Hz
Pulse width(FWHM)	0.3ns
USHO Dye module	
Wavelength	396nm
Spectrum Bandwidth(FWHM)	5ns
Pulse width(FWHM)	0.2ns
Max. rate	20Hz

Table 5.2: Characteristics of the USHO laser.

LSI Laser

The Laser Science Instruments (LSI) dye laser system is used for long term TQ calibration, called 'auto TQ calibration'. Because it runs every 1 second, it is also used for the PMT nonlinearity calibration and the OD calibration. Since this laser system uses nitrogen as a gain medium, continuous operation is easier compared to the USHO laser. The characteristics of the LSI Laser are shown in Table 5.3.

LSI N_2 laser	
Wevelength	337.1nm
Max. rate	20Hz
Pulse width(FWHM)	$\leq$ 4ns
USHO Dye module	
Wavelength	396nm
Spectrum Bandwidth(FWHM)	0.3ns
Pulse width(FWHM)	$\leq$ 4ns
Max. rate	20Hz

Table 5.3: Characteristics of the LSI laser.

5.1.4 Laser light source for water quality monitoring

The laser light source is also used for monitoring the water quality. There is 4 lasers, with different wavelengths, to monitor the time variation and wavelength dependence of the water quality. At the beginning of SK-IV, the 337 nm wavelength LSI laser converted the wavelength by use of a dye. Since then a new laser, an LTB 337 nm laser, and a set of laser diodes were newly installed to achieve stable intensity during data taking. The summary of used laser light is shown in Table 5.4, with the laser characteristics is as follows.

laser	wavelength	Replace date	Replace laser	Replace wavelength[nm]
LSI laser	337nm	Oct.2010	LTB laser	337nm
LSI+dye module	365nm	Jul.2009	Laser Diode	375nm
LSI+dye module	400nm	Jul.2009	Laser Diode	405nm
LSI+dye module	420nm	Mar.2009	Laser Diode	445nm

Table 5.4: Laser type for water quality monitoring, for each wavelength.

LTB laser

The Laser Technik Berlin (LTB) laser which is shown in Fig.5.3, is newly installed in October of 2010. The characteristics of the LTB laser are shown in Table 5.5. Compared with the LSI laser, the intensity of the light is much more stable.

Wevelength	337.1nm
Max. rate	100Hz
Pulse width(FWHM)	3ns

Table 5.5: Characteristics of the LTB laser.

Figure 5.3: Picture of LTB laser.

Figure 5.4: Picture of a single laser diode.

Laser diodes

To further improve water calibrations in SK-IV, the nitrogen/dye laser was further replaced with laser diodes (LD)(Fig.5.4), which are NIM module types, because the intensity of the nitrogen laser is unstable and gradually its intensity decreases. The laser diodes are stable even if environmental conditions, like temperature, are changed. At first, the 445nm LD was delivered for testing in November of 2008, and then it was replaced to the 375 nm and 405 nm LD in July of 2009. Finally a 473 nm LD was introduced in Feb of 2010. The characteristics of the LD are shown in Table 5.6.

5.1.5 LINAC

An electron beam produced by a linear accelerator (LINAC) is used for precise calibration of the absolute energy. The LINAC is placed just beside the SK tank. The detailed information

Wevelength	445, 375, 405, 473nm
rate	Single∼1MHz
Select-able pluse duration	1,3,5ns
Intensity	tunable

Table 5.6: Characteristics of the laser diodes.

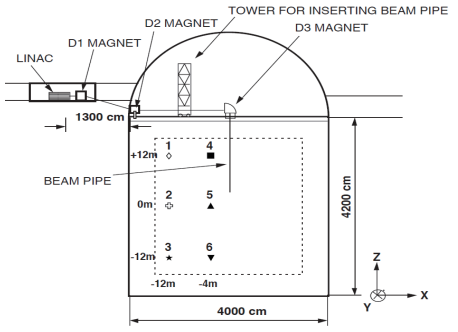

Figure 5.5: Schematic view of the LINAC system.

about the LINAC is written in [33]. The momentum of the electron beam is accurately known ($\sim 0.2\%$ accuracy) using a well calibrated germanium detector. Fig.5.5 shows the schematic view of the LINAC system. The electron beam which is accelerated by the LINAC is injected into the SK tank through an evaculated pipe (less than 0.1Pa). The range of the beam momentum is about 5-18 MeV/c, which covers the momentum range of recoil electrons coming from solar neutrino interactions.

5.1.6 DT generator

The deuterium-tritium (DT) generator [31] is a calibration device which emits neutrons via the following reaction:

$$^3H +^2 H \rightarrow^4 He + n. \tag{5.1}$$

The energy of the generated neutron is 14.2 MeV, which is enough energy to generate ^{16}N via the following reaction:

$$^{16}O + n \rightarrow^{16} N + p. \tag{5.2}$$

The ^{16}N decays with gamma-rays and/or electrons, with a half-live of 7.13 seconds. The main decay mode is to produce a 6.1 MeV gamma and a 4.3 MeV electron (66%) or a 10.41 MeV electron (28%). Fig.5.6 shows the schematic view of the DT calibration.

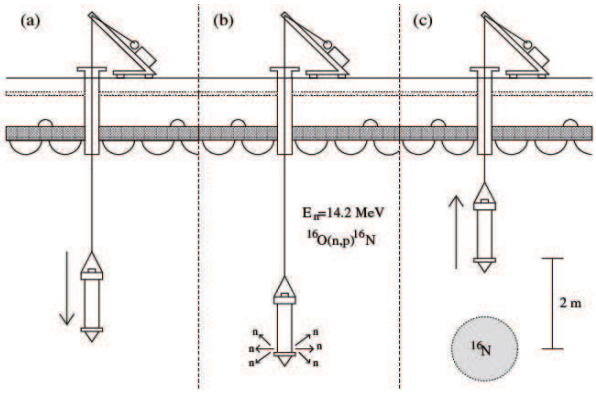

Figure 5.6: Schematic view of the DT system.

5.2 PMT calibration

Super-Kamiokande consists of about 11,000 20-inch PMTs inside the inner detector. To achieve precise measurements of solar neutrinos, PMT calibration has an important role, because the PMT response affects the event reconstruction and so on. We have performed PMT gain and quantum efficiency (QE) measurements during the SK-III period, and timing calibrations during SK-IV. In this section, the PMT calibrations are described.

5.2.1 PMT gain calibration

We define two factors to describe the PMT charge response, QE and gain. QE is determined as the probabilty of emitting a photo-electron when a photon hits the PMT photo-cathode. The gain ($A(i)$) is defined as the amplification factor of each photo-electron by the PMT dynodes. Furthermore, we split the gain factor into two factors, the 'absolute gain' and the 'relative gain'. The absolute gain is a common gain factor for all PMTs, which is a conversion factor from the output charge [pC] to the number of photo-electron [pe]. The 'relative gain' is the relative difference of each individual PMT.

In the beginning of SK-III, the high voltage (HV) of each PMT was determined using the PMT charge response (Q_{obs}) from the xenon light source. The Q_{obs} was determined as

$$Q_{obs}(i) \propto N_{photon}(i) \times QE(i) \times A(i) \tag{5.3}$$

where, i is the PMT sequential number and N_{photon} is the number of photons which hit the photo cathode. It was success to determine the HV to set the uniform charge output (Q_{obs}) within 1.3% RMS.

After determination of the HV, the absolute gain was measured by the nickel source. Because the nickel source emits 1 photo-electron level light, the charge distribution of one photo-electron hits can be obtained. Fig.5.7 shows the output charge distribution of one photo-electron data obtained by nickel calibration. The SK-IV distribution was multiplied by 0.844 in order that the peak of the SK-IV distribution matched the peak position of SK-III. Because the PMT gain increased $2 \sim 3$% in every year, and with different performance of charge digitization due to new front-end electronics, the peak value of SK-IV is higher than SK-III. The behavior difference

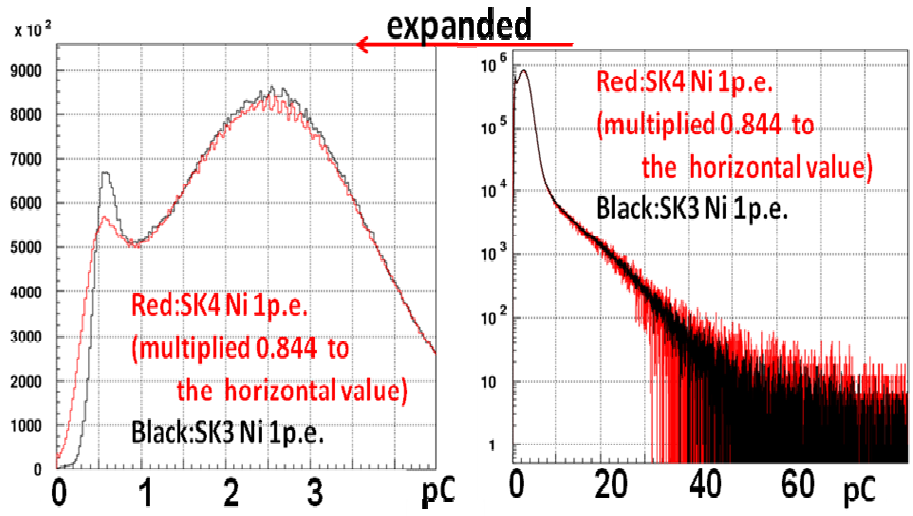

Figure 5.7: Output charge distribution of one photo-electon hits for SK-III (black) and SK-IV (red). The SK-IV distribution was multiplied by 0.844 so that the peak of the SK-IV distribution matched the SK-III peak.

of the lower charge between SK-III and SK-IV is caused by the difference of the front-end electronics performance and the difference in charge discrimination. From this distribution, we can get the absolute gain value for SK-IV as 2.645 [pC/p.e.]. Table 5.7 shows the absolute gain value for each SK phase.

SK phase	Absolute gain
SK-I	2.055
SK-II	2.297
SK-III	2.243
SK-IV	2.645

Table 5.7: The absolute gain, conversion factor from output charge of PMT [pC] to number of photo-electrons. Because the gain increases as time passes, even with constant HV, the absolute gain factor becomes larger with time, but new PMTs which were installed just before SK-III have lower gain than those used during SK-II. The absolute gain was slightly lower in SK-III.

The relative gain was measured with two sets of laser calibration data. One with high light output (∼50 photo-electrons/PMT) and another with a 1 photo-electron level in each PMT. Using the former data, the observed charge (Q_{obs}) is obtained, while using the latter, the number of hit counts over many laser fires are counted, which is called $N_{hit}(i)$.The ratio between Q_{obs} and N_{hit} gives the relative gain as

$$\frac{Q_{obs}(i)}{N_{hit}(i)} \propto \text{Relative Gain}(i). \tag{5.4}$$

This method is free from the water transparency, geomagnetic field and so on.

5.2.2 PMT quantum efficiency measurement

As described in the previous section, quantum efficiency is defined as the probability of photo-electron production when a photon hits the photo cathode. Individual PMTs have their own QE values, and so QE measurement for each PMT is needed. For the mearurement of the QE, the nickel source is used, mostly because this light source emits one photo-electron level light and matches the spectrum of Cherenkov light.

The hit rate of each PMT is used. Details of the method are described here. Each PMT has a sequential number, from 1 to 11146, with numbers 1-7650 placed in the barrel part of detector, 7651-9398 in the top, and 9399-11146 in the bottom. The hit rate of each PMT includes dark noise contrubution. To remove hits due to dark noise and only count hits from the nickel light source, 'on-time' and 'off-time' hits are defined. Fig.5.8 shows the hit timing distribution, with time of flight subtracted, from the source to the reconstructed event vertex. Then counts of hits in the windows of on-time and off-time are made. On-time and off-time are defined as 750-1050 nsec and 1200-1500 nsec, respectively. Substracting off-time hits from on-time hits, the true hitrate is obtained. This quantity is defined as $hit(i)$. In order to take into account position dependence of PMT positions, a geometrical correction is applied and the corrected hit hit_{corr} is defined as

$$hit_{corr}(i) = hit(i) \times R^2(i)/a(\theta(i)), \tag{5.5}$$

where R(i) is the distance from the source position to PMT(i) and $a(\theta(i))$ is the acceptance of the PMT, which can be described as

$$F(\theta) = 0.205 + 0.524 \times \cos\theta + 0.390 \times \cos^2\theta - 0.132 \times \cos^3\theta. \tag{5.6}$$

This fuction was obtained from the simple geometry of the PMTs.

Finally the hit_{corr} is normalized by the total number of hit_{corr} and the number of PMTs (N_{PMT}=11,129 for SK-III and IV), and is described

$$\text{hitrate}(i) = \text{hit}_{corr}(i)/(\Sigma\text{hit}_{corr}(i)/N_{PMT}). \tag{5.7}$$

Even though the upper corrections are applied, the position dependence of the PMT hit rate remains. This is especially true in the case of photon reflections by neighboring PMTs or water scattering. They can be reproduced by MC. Fig.5.9 shows the hitrate distribution of both data and MC. In this MC, QE of all PMT is set to the same value. The hitrate ratio between the data and MC is defined as the QE table. Data was taken when the detector water was well mixed, and the position dependence of the water transparency must have been negligible. MC was geneated with uniform water transparency.

5.2.3 PMT timing calibration

The PMT timing calibration is very important because event vertex reconstruction is based on PMT timing information. Ideally, the timing response of each PMT is the same, but due to the length of the PMT signal cable and response of the electronics, there is a PMT dependence on the timing information. Due to time walk, which is shown in Fig.5.10, a correction due to the

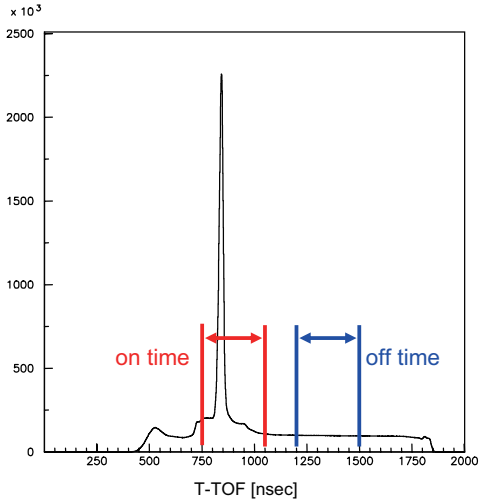

Figure 5.8: Hit timing distribution of nickel light source events.

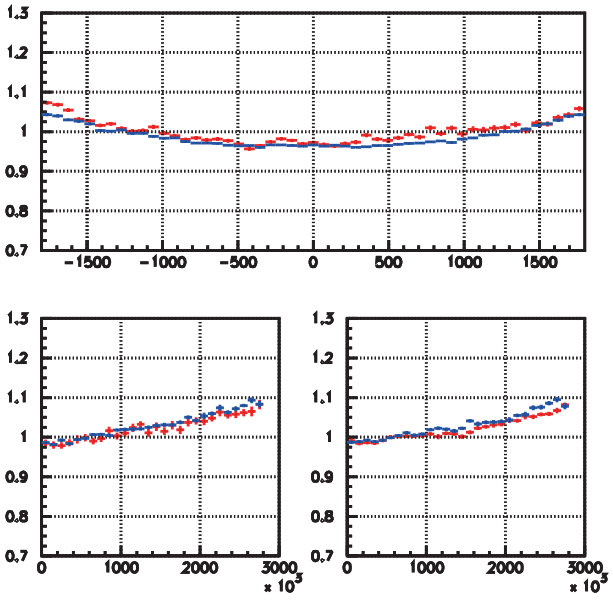

Figure 5.9: Position dependence of the PMT hit rate. The upper, bottom left and bottom right figures show the hitrate for the barrel, top and bottom PMTs, respectively. The horizontal axis of the upper figure is the z [cm] positon of PMTs. For the lower figures, the horizontal axis is the square of the distance from the center $[cm^2]$ of the tank. The red and blue distributions show the hitrate of data and MC, respectively.

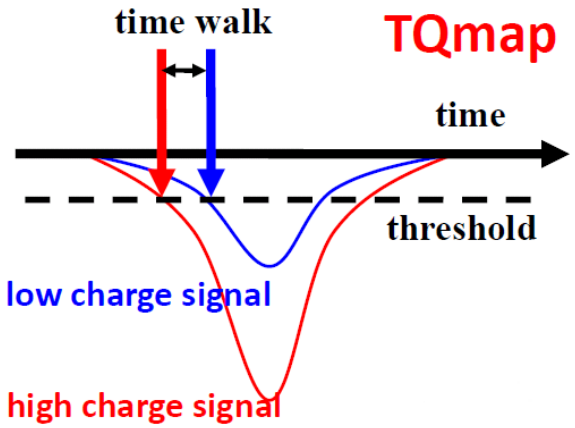

Figure 5.10: Explanation about time-walk.

pulse height (integrated charge) is necessary. Time-walk occurs because if the observed charge is larger, the PMT signal exceeds the TDC discriminator threshold earlier, and if lower, it exceeds later. To correct them, the timing-charge relation table, called the TQ map, should be made for each PMT. In this section, details of the PMT timing calibration are described.

For the timing calibration, a laser light source is used because of its fast rise time and ease of light intensity control. At the beginning of SK-IV, data was taken using the USHO laser light source, with various light intensities. Fig.5.11 shows the schematic view of the USHO laser light calibration.

The method of making the TQmap is as follows; (1) Make the timing distribution plot for each PMT, after subracting the time of flight from the light source position to each PMT. Fig.5.12 shows an example of the timing vs charge distributions for one PMT. The charge value (Q_{obs}) is divided into 180 bins, with the following bin sizes.

$$\Delta Q_{bin} \equiv \begin{cases} 0.2 \text{ pC}, & \text{for } 1 \leq Q_{bin} \leq 50 \text{ (0 pC} \leq Q \leq 10 \text{ pC)} \\ 10^{\frac{Q_{bin}}{50}} - 10^{\frac{Q_{bin}-1}{50}}, & \text{for } 51 \leq Q_{bin} \leq 180 \text{ (10 pC} \leq Q \leq 3981 \text{ pC)} \end{cases} \tag{5.8}$$

(2) The timing distribution has a binning effect, so it is necessary to smooth the timing histogram. This method is called the smearing method and Fig.5.13 gives an explanation. First we apply an asymmetric gaussian fit from t-low to t-high, which is defined in Fig.5.13 as the value of horizontal axis of 0.05% from peak value. The asymmetric gaussian fit results are taken into account into MC as a timing resolution of each observed charge. After getting the max value for each Q_{obs} bin, we apply fitting by 3rd-degree polynomial fuction for the low Q range, 5th-degree polynomial function for the middle Q range, and 7th-degree polynomial function for the high Q range. Each charge range is defined in section 2. Timing information after the TQmap correction is shown in Fig.5.14.

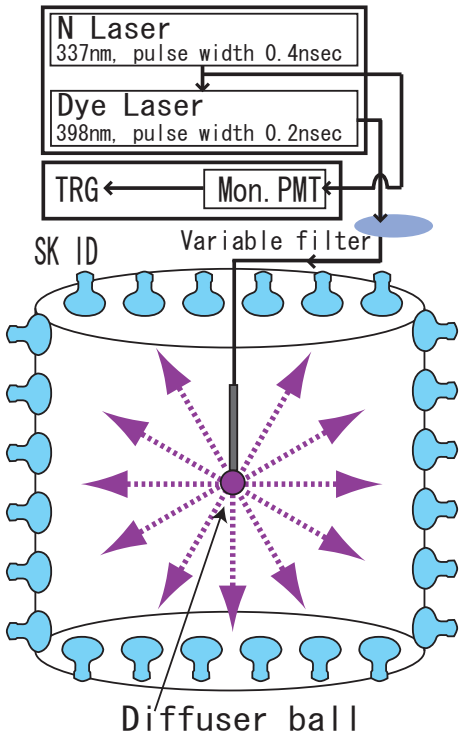

Figure 5.11: Schematic view of the USHO laser light calibration system.

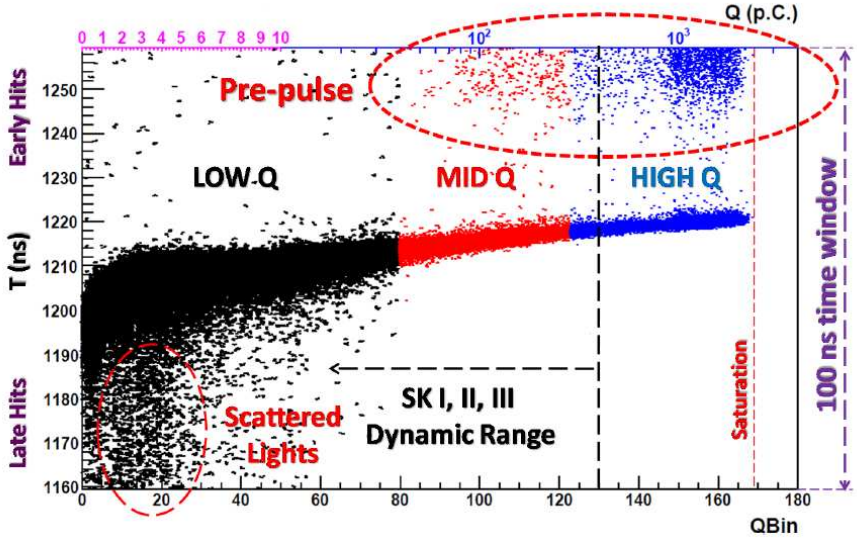

Figure 5.12: Obtained TQ map by the USHO laser. The horizontal axis shows Q_{bin}, defined in equation 5.8. Black, red and blue points are the QBEE charge ranges as defined in chapter 2.

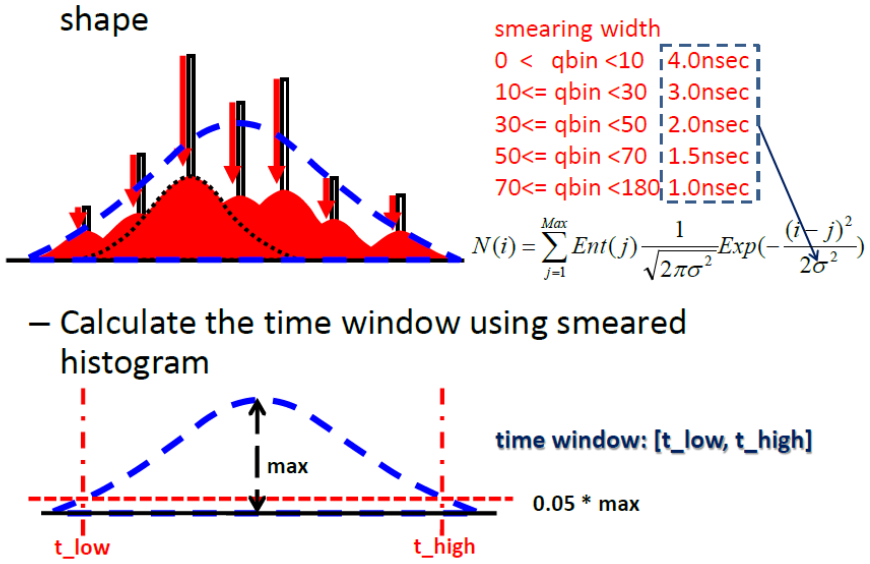

Figure 5.13: Schematic view of the TQ smearing method. Each bin has its binning effect, expanded to a Gaussian distribution. The sigma of the Gaussian is defined for each Q_{bin} value. After smearing the timing distribution, we apply an asymmetric gaussian fit from the lower part to higher part, as shown in this figure.

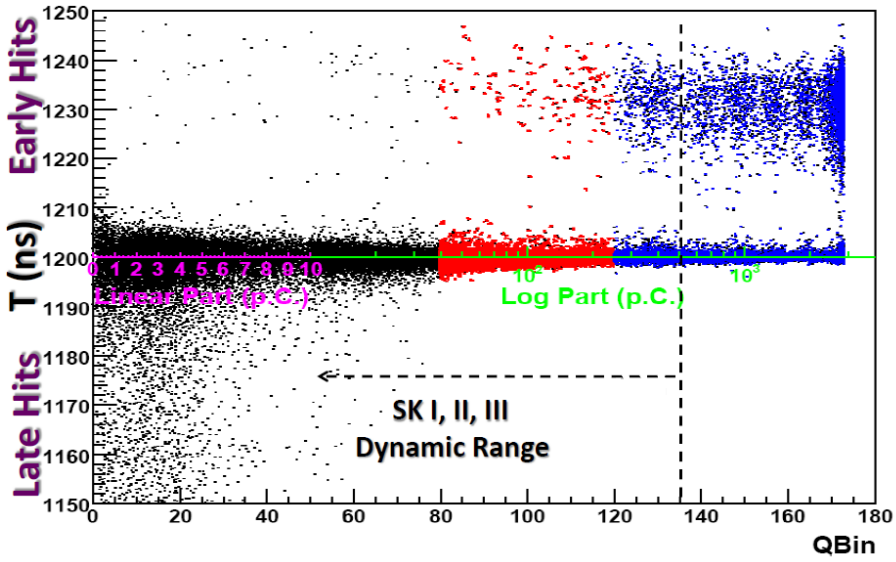

Figure 5.14: Timing distribution after correcting with the TQ map.

5.3 Water transparency measurement

The water transparency measurement is also important because it affects the number of photons which are detected by the PMTs. This means water transparency affects energy determination. In this section, the two water transparency measurements, decay-e and N_2 laser, are described. Finally the input parameters to the MC are described.

5.3.1 Measurement by decay-e

As discussed in section 2, due to the improvements of the water circulation system, the water transparency of the SK-IV detector is kept more stable at a higher quality. But still there is a time variation. In order to take into account the time variation, we always monitor the water using decay electrons/positrons from cosmic-ray muons, which have stopped in the detector (in this thesis, these events are called decay-electron or decay-e). The selection criteria of decay-e events are;

- The time difference between the parent muon event and the decay-e candidate event is $3.0\mu\text{sec} \leq \Delta\text{T} \leq 8.0\mu\text{sec}$.
- The reconstructed vertex of the decay-e candidate events is within the 22.5 kton fiducial volume, i.e. 2 m from the wall.
- The distance between the stopping point of cosmic ray muon and decay-e candidate event is within 250 cm.
- The number of hit PMTs within the 1.3μsec selects $120 \leq N_{hits} \leq 600$.

The event rate of the decay-e events is about 1,500 events in one day. Using these decay-e events, correlation between the log of the observed charge, $\log(Q_{obs}(r))$, of hit PMTs and the distance between the decay-e vertex and hitPMTs can be obtained. Fig.5.15 shows the charge versus distance distribution. For the hit PMTs, an opening angle of $32^\circ < \theta_{dir} < 52^\circ$ was used. Then we apply linear fitting to this distribution, and the inverse of the fitted slope becomes the water transparency. From statistics, it needs to take a running average of ± 7 days, using a linear function. Fig.5.16 shows time variation of the water transparency for the SK-IV period. One point corresponding to one elapsed day.

5.3.2 Measurement by laser light injector

The coefficients of the water parameters are the absorption coefficent(α_{Abs}), the Rayliegh scattering coefficient(α_{Raylie}) and the Mie scattering coefficients(α_{Mie}). Each coefficient is independently measured by either an N_2 laser or a laser diode(LD). Fig.5.17 shows a schematic view of the water coefficient measurement.

The lasers are fired every 1 minute. Using this data, the water coefficients are obtained by the following method.

- Make [scattered Hit]/[Q_{tot}] distributions, Hit/Q_{tot} hereafter, for each detector region (Top, B1,..., B5, Bottom), as shown in Fig.5.17.

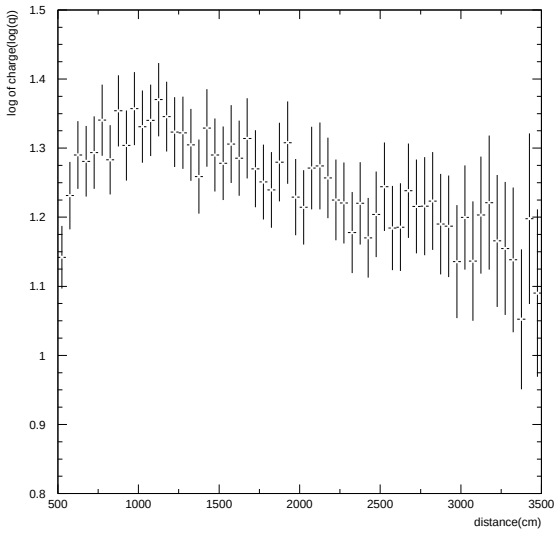

Figure 5.15: Charge vs. distance between the decay-e vertex distribution and hit PMTs. The vertical axis shows the log of the observed charge, $\log(Q_{obs})$.

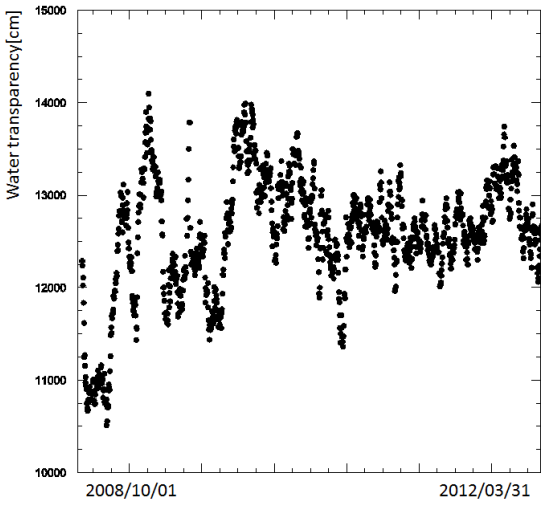

Figure 5.16: Time variation of the water transparency measured by decay-e events.

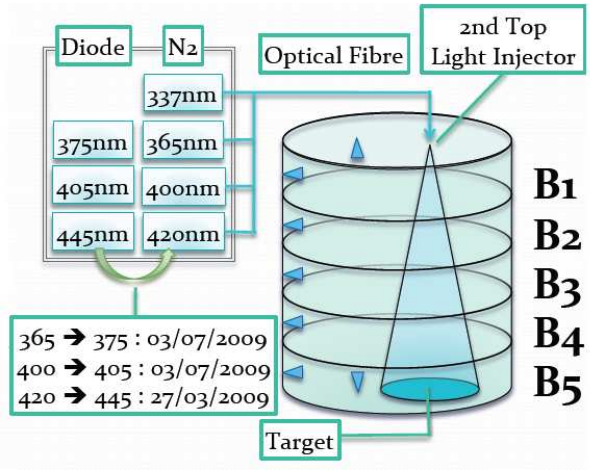

Figure 5.17: Schematic view of the measurements of the water coefficients. An N_2 laser was used for 337nm measurements, while laser diodes were used for the other wavelength measurements.

- Generate Monte Carlo by varying water coefficients and make same Hit/Q_{tot} distributions. Fig.5.18 shows Hit/Q_{tot} distributions of data (black) and MC (red).
- Compare each MC with data by χ^2 defined as

$$\chi^2 = \Sigma \frac{(DATA - MC)^2}{\sigma^2_{DATA} + \sigma^2_{MC}}. \tag{5.9}$$

- Find minimum value for each water coefficient.

When the water coefficients were input to MC, the symmetric scatteing (Rayleigh+symmetric Mie scattering) and the asymmetric scattering (forward Mie scattering), instead of Rayleigh and Mie scattering are take into account. Fig.5.19 shows the definition of the symmetric and asymmetric scattering. So water transparency in the MC is described as

$$WT = \frac{1}{(\alpha_{abs} + \alpha_{Sym.scat.} + \alpha_{Asym.scat.})}. \tag{5.10}$$

After getting the water coefficients for each wavelength, they are fit with an empirical function. Fitted functions for each water coefficient are as follows;

$$\begin{aligned}
\alpha_{sym}(\lambda) &= r_1 \times \frac{1}{\lambda^4}\left(1.0 + \frac{r_2}{\lambda^2}\right) \\
\alpha_{asy}(\lambda) &= m_1 \times \left(1.0 + \frac{4.623 \times 10^6}{\lambda^4} \times (\lambda - 3992.4)^2\right) \\
\alpha_{abs}(\lambda) &= a_1 \times \frac{2.691 \times 10^7}{\lambda^4} + \left(a_1 \times 1.164\left(\frac{\lambda}{500.0}\right)^{10.94}\right) && (\lambda \leq 463.9) \\
&= a_1 \times \frac{a_2}{\lambda^4} + \text{Popefry}(\lambda), && (\lambda \geq 463.9)
\end{aligned}$$

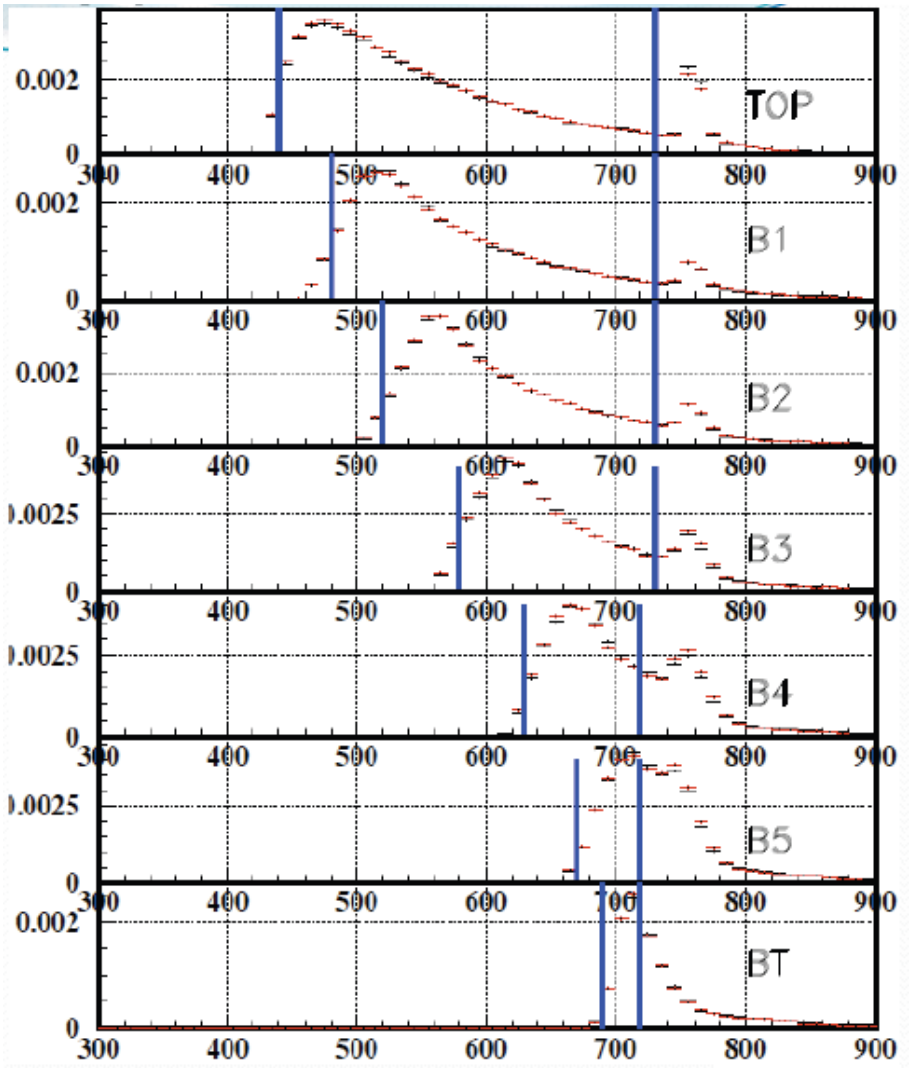

Figure 5.18: Hit/Q_{tot} distribution from the laser calibration. The horizontal axis shows time [ns], while the vertical axis shows Hits/total charge, for data (black) and MC (red). The first peak and second peak correspond to scattering of photons in the water and those reflected on the bottom PMTs and black seats.

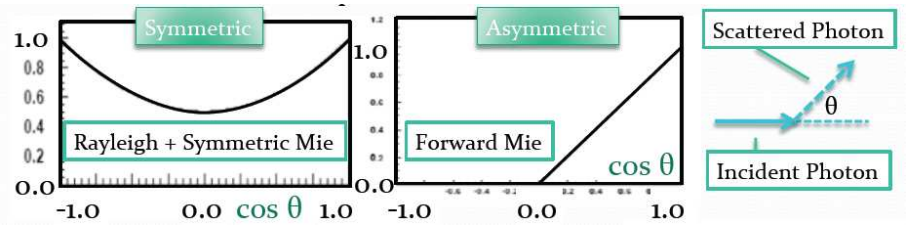

Figure 5.19: Definition of the symmetric and asymmetric scattering in the MC.

where r_1, r_2, m_1 and a_1 are multiplicative factors which adjust the function to match the water transparency and λ is the wavelength of Cherenkov light. The numbers, except for r_1, r_2, m_1 and a_1, are used as fixed values because they were historical factors present in the equations. The additional factor of the absorption function, above 463.9 nm, was defined by theoretically calculated data by Pope and Fry[34]. Fig.5.20 shows the observed water coefficents for each wavelength, shown in circles with error bars, and the best fit value of function $\lambda \geq 463.9$, using April 2009 data. The symmetric and asymmetric parameters from this result are used during the whole SK-IV period. Time and position dependences is described in the next section.

5.4 Input parameters to detector simulation

In this section, the input parameters which are used in the MC are introduced. Most of the physics processes of the SK detector are based on GEANT 3.21, but the Cherenkov photon propagation and light attenuation in water were originally developed by the SK woring group. As already described along with PMT calibration, the one photon distribution, Quantum efficiency table and TQ mapping are input parameters. Photon propagation, time and position dependence of water transparency, and PMT response are described in this section.

Cherenkov photon propagation

The number of emitted Cherenkov photons dN by an electron is given by

$$d^2N = \frac{2\pi\alpha}{n(\lambda)\lambda^2}(1 - \frac{1}{n^2\beta^2})dxd\lambda, \tag{5.11}$$

where n is the refractive index of the water (n=1.343 at λ=400 nm), α is the fine structure constant ($\simeq$1/137) and β is the velocity of the electron, per light velocity, in vacuum(v/c). dx and $d\lambda$ are the track length and wave length, respectively. The opening angle of the emitted Cherenkov photon is given by

$$cos\theta = \frac{1}{n\beta}. \tag{5.12}$$

From the constraint on the value of $cos\theta$, the energy threshold of the Cherenkov light emission (E_{thr}) is

$$E_{thr} = \frac{nm}{\sqrt{n^2 - 1}}. \tag{5.13}$$

where m is a electron mass.

Time dependence of water transparency

Because the time variation of the scattering parameters is small, only the absorption parameter is variable in the MC and the symmetric and asymmetric scattering are set to fixed values. The energy scale calibration, which is described in section 5.5, was done by LINAC data taken in August of 2010, and needs the precise water coefficients from August 2010. The values of r_1, r_2, m_1 and a_1 in August 2010 are calculated as

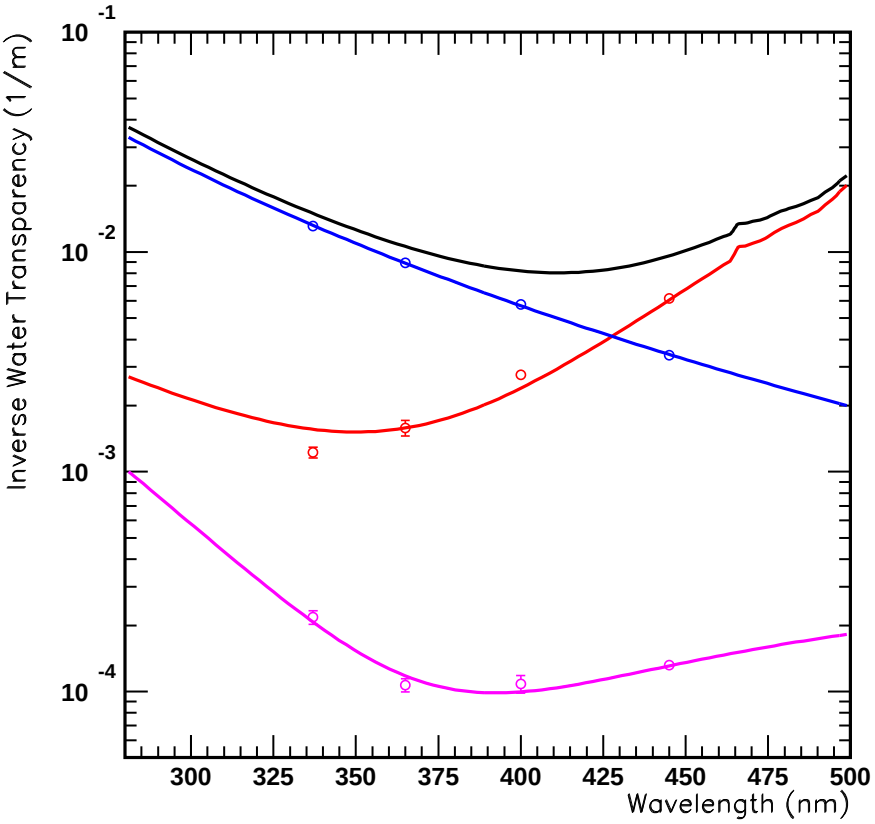

Figure 5.20: The fitted inverse water transparency as of April 2009. The black line shows the fitted result of the water transparency, the red is absorption, blue is the symmetric scattering, and pink is the asymmetric scattering.

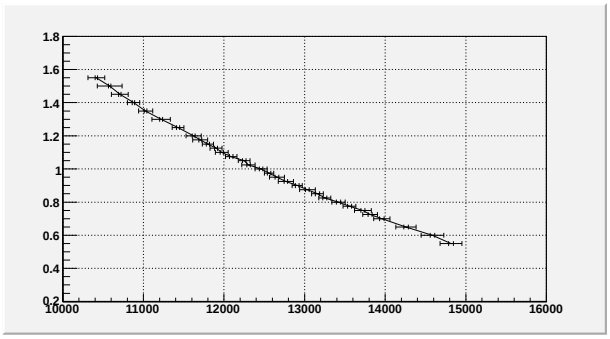

Figure 5.21: The relationship between decay electron water transparency (horizontal[cm]) and the absorption factor (vertical, scaled to 1 in August 2010).

$$\begin{aligned} r_1 &= 8.514 \times 10^8 \\ r_2 &= 1.138 \times 10^6 \\ m_1 &= 1.002 \times 10^{-4} \\ a_1 &= 0.7142. \end{aligned} \tag{5.14}$$

The water quality in SK changes as a function of time, as shown in Fig.5.16. The relationship between the water transparency of decay electrons and the absorption parameter was estimated to match the input electron energy and reconstructed electron energy. Fig.5.21 shows the correlated function between water transparency and the absorption parameter. The vertical axis is scaled so the absorption parameter is equal to 1 in August 2010.

Position dependence of water transparency

Because it was known that there is position dependence, especially z-position dependence, of the water transparency. This position dependence mainly due to supplying purified water from the bottom of the detector and draining from the top. The position dependence of the water transparency is continuously monitored by the auto-xenon calibration source (every 1 minute) and the nickel calibration source (once per month), since the beginning of the SK-III phase. This position dependence is also checked by using the value of the top bottom asymmetry (TBA).

$$TBA = (< top > - < bottom >)/ < barrel > \tag{5.15}$$

For the nickel light source $< top >$, $< bottom >$ and $< barrel >$ show the mean hit PMTs hitrate in each of the top, bottom and barrel parts of the detector. The situation is similarly for the auto-xenon light source, but the mean PMT charge is used to define the value. From the TBA value, there seems to be a $3\% \sim 5\%$ level of z-dependence of the water transparency. It accounts for $\pm 0.5\%$ of the systematic uncertainty of the directional dependence of the energy reconstruction, in the SK-I solar neutrino analysis. Even though there is a z-dependence of the water transparency, the original MC could not reproduce this position dependence, because uniform attenuation length over the detector volume was used. When the quantum efficiency

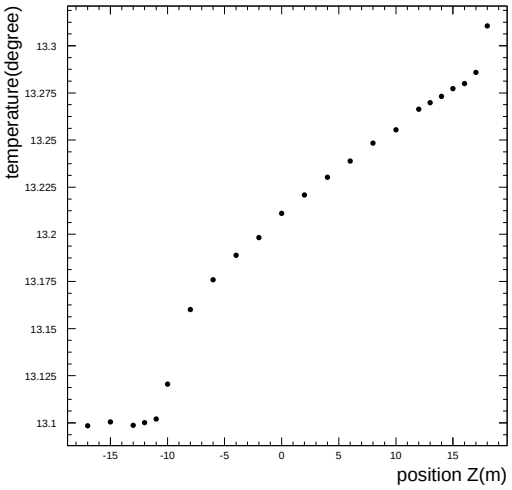

Figure 5.22: Z-dependence of the detector water temperature. Below z=-1100 cm, the water temperature is uniform because of convection.

was measured, the nickel data when the detector water transparency was uniform was used, and convection was forced to happen by increasing the supply water temperature. But, usually convection does not happen and the non-uniforminity of water transparency exists. This should be taken into account in the MC. So the simple model of the light absoption, as shown in equation 5.16, is introduced to MC.

$$\alpha_{abs}(\lambda, z) = \begin{cases} \alpha_{abs}(\lambda)(1 + \beta \times z), & \text{for } z \geq -1100\text{cm} \\ \alpha_{abs}(\lambda)(1 - \beta \times 1100), & \text{for } z < -1100\text{cm} \end{cases} \tag{5.16}$$

As discussed below, the variation of the water transparency is mainly due to the absorption parameter, and so only the absorption parameter is varied along with the detector z position. Below z=-1100 cm we assume a unifrom absorption parameter, because of convection of the water. Fig.5.22 shows the z-dependence of the water temperature. It is clealy seen that there is convection below z=-1100 cm. The parameter β shows the degree of the z-dependence of the water transparency. This β parameter is tuned by the hitrate analysis.

In principle, the hitrate analysis is based on the method of measuring quantum efficiency. To cancel the effects of the quantum efficency of the PMTs, QE(i), the equation 5.5 is changed to

$$hit_{corr}(i) = hit(i) \times R(i)^2 / F(\theta(i)) / QE(i). \tag{5.17}$$

After generating the hitrate table for data and MC with the β value set between 0 to 0.016 [1/m], we calcluate the χ^2 for each β value of MC and determine the best β value from the minimum χ^2. Fig.5.24 shows an example of the hitrate for data and MC, β equal to 0 (no z-dependence) and to the best value (best z-dependence).

The TBA value and the β value are correlated according to

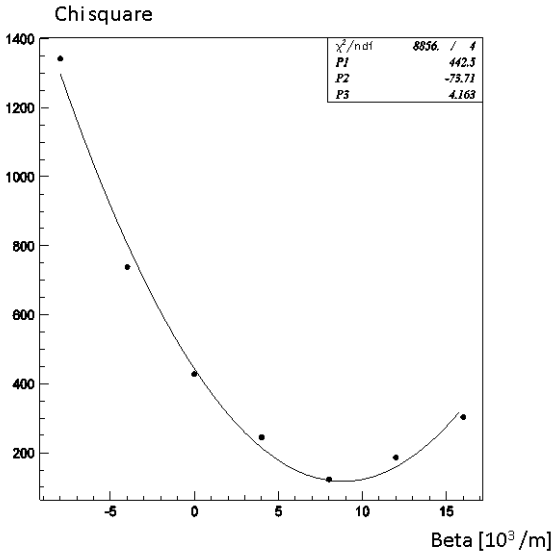

Figure 5.23: Estimated χ^2 for each β, with the minimum χ^2 value setting the best β value.

$$\beta = \{-0.163(TBA)^2 \times 3.676(TBA)\} \times 10^{-3}. \tag{5.18}$$

From the TBA value of the auto-xenon calibration, the time variation of the position dependence is reconstructed.

PMT response to photons

When generated photons arrive at the surface of the PMTs in the MC, one of the following 3 actions is selected; (1) absorbance by the photo-cathode (with some fraction of it causing photo-electron production), (2) reflectance from the PMT surface, or (3) transmitance through the PMT, as explaind in Fig.5.25(b). Each process has an incident angle dependence. The final probablity of the photo-electron genaration is defined as follows.

$$\text{Probability} = QE(\lambda) \times P_{obs}(\theta_i, \lambda) \times \text{COREPMT} \times \text{qetable}(i) \tag{5.19}$$

$$P_{obs} = \frac{\text{Absorption}(\theta_i, \lambda)}{\text{Absorption}(0, \lambda)} \tag{5.20}$$

$QE(\lambda)$ is the incident wavelength (λ) dependence of the quantum efficiency of the 20 inch PMTs, measured by Hamamatsu and shown in Fig.3.9, Absorption(θ_i, λ) is the summed fraction of the photo-electron generation (green) and absorption (black) in Fig.5.25(b), which is measured by the laser light source calibration with each λ. COREPMT is a correction factor which is fine tuned by LINAC calibration (described in detail in section 5.5), and qetable(i) is described in 5.2.2. After the photo-electrons are generated, the output charge, which is described in section 5.2.1, is simulated and if the output charge exceeds the threshold of the front-end electronics,

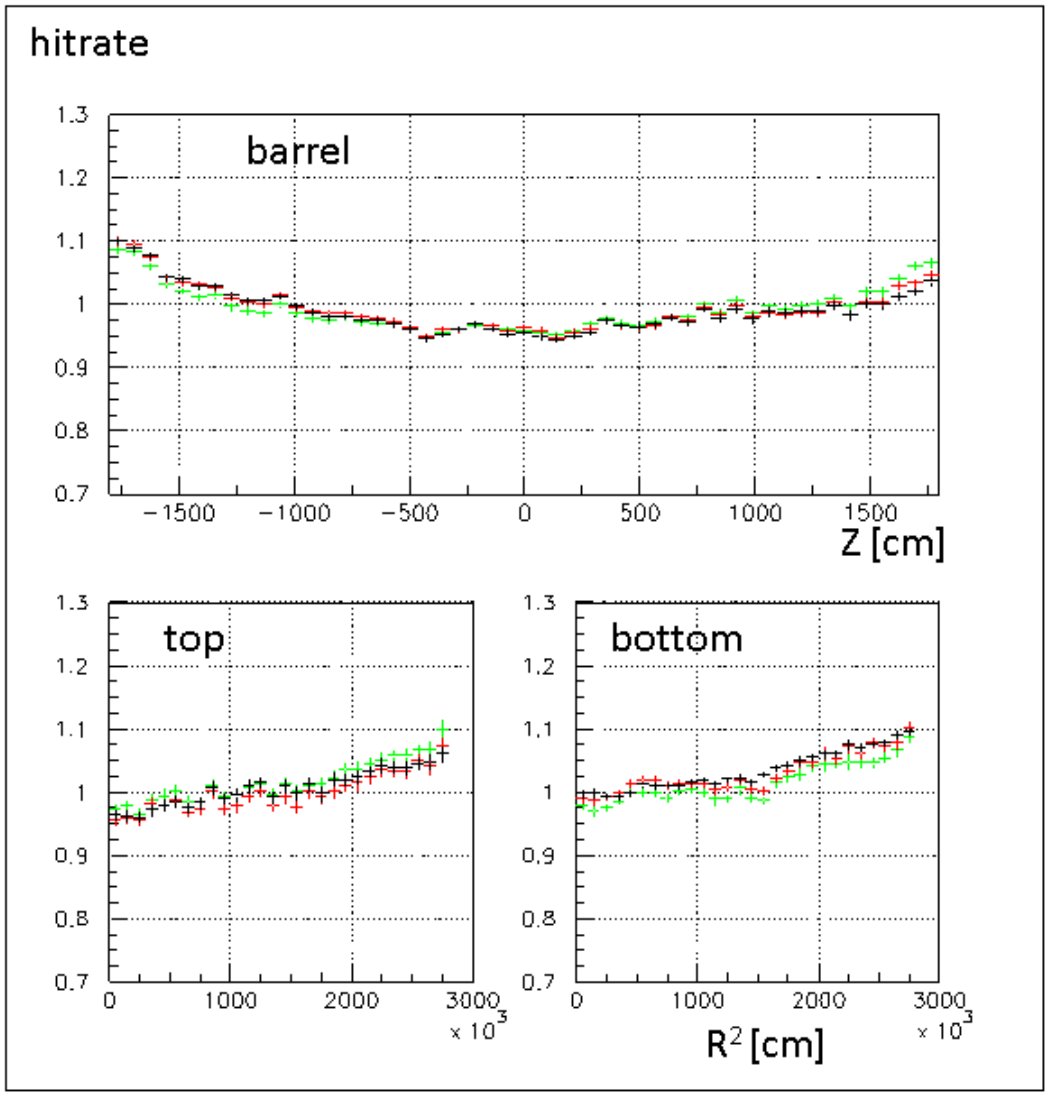

Figure 5.24: Hitrate of data (black) and MC (β=0 for green and β=best for red).

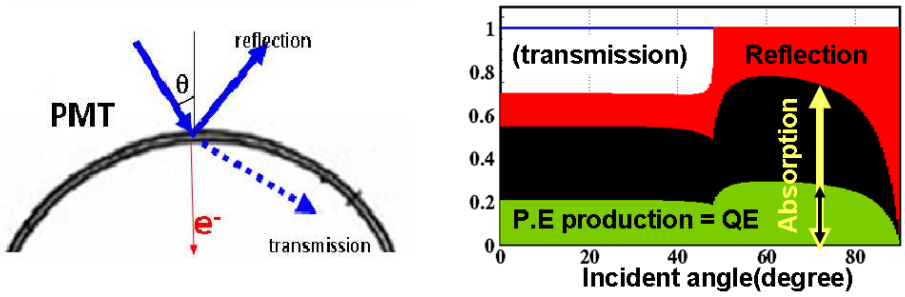

(a) (b)

Figure 5.25: (a) Schematic view of PMT response for incident light. (b) PMT response for incident 420 nm unpolarized light, depending on incident angle. The black area shows the fraction of photons that are absorbed but don't generate photo-electrons.

the photon is detected by the PMT. The timing resolution which is estimated in section 5.2.3 is also taken into account in this simulation.

5.5 Absolute energy scale calibration

In this section the determination of the absolute energy scale and its position and directional depnedences are described. The LINAC calibration system can produce an electron beam with precisely tuned electron momentum, but can only take data with events in the down-going direction. The DT calibration system can produce uniform directional data, but emits continuous momentum electrons along with gamma rays. Because of these differences, the absolute energy scale, i.e. determination of COREPMT, is performed by the LINAC and the corresponding energy scale cross check, which is position and directional dependence, is done by the DT calibration. The time variation of the energy scale, which is estimated by LINAC, DT and decay-e calibrations, will be described in the final subsection.

5.5.1 LINAC calibration

LINAC data taking

The LINAC calibration was done in August of 2009 and August of 2010 during the SK-IV phase. The water transparency was slightly unstable during the August 2009 data taking, so the energy scale determination was done with the August 2010 data. The position and energy mode is summarized in Table 5.8.

Beam momentum estimation

The precise electron beam energy is measured by a germanium detector. The characteristics of the germanium detector is its good energy resolution and good output linearity for given input particle energies. Fig.5.26 shows the output charge of the germanium detector as a function of the gamma-ray energy of several calibrations, which are shown in the point. For the few MeV region, the difference of the output of germanium detector count from the fitted line is within 0.1%.

Aug. 2009 data	
position of beam pipe	energy mode
(-1237,-70.7,1197)[cm]	18.9,13.6,8.8,4.8[MeV]
(-1237,-70.7,-6)[cm]	18.9,13.6,8.8,5.1[MeV]
(-1237,-70.7,-1209)[cm]	18.9,13.6,8.8,5.1[MeV]
(-388.9,-70.7,1197)[cm]	18.9,13.6,8.8,5.1,4.8[MeV]
(-388.9,-70.7,-6)[cm]	18.9,13.6,8.8,5.1,4.8[MeV]
(-388.9,-70.7,-1209)[cm]	18.9,13.6,8.8,5.1,4.8[MeV]
(-1237,-70.7,1197)[cm]	18.9,13.6,8.8,5.1,4.8[MeV]
Aug. 2010 data	
(-1237,-70.7,1197)[cm]	13.6,7.0[MeV]
(-1237,-70.7,-6)[cm]	13.6,7.0[MeV]
(-1237,-70.7,-1209)[cm]	13.6,7.0[MeV]
(-388.9,-70.7,1197)[cm]	13.6,7.0[MeV]
(-388.9,-70.7,-6)[cm]	18.9,13.6,7.0[MeV]
(-388.9,-70.7,-1209)[cm]	13.6,7.0[MeV]

Table 5.8: Data sets of SK-IV LINAC calibration.

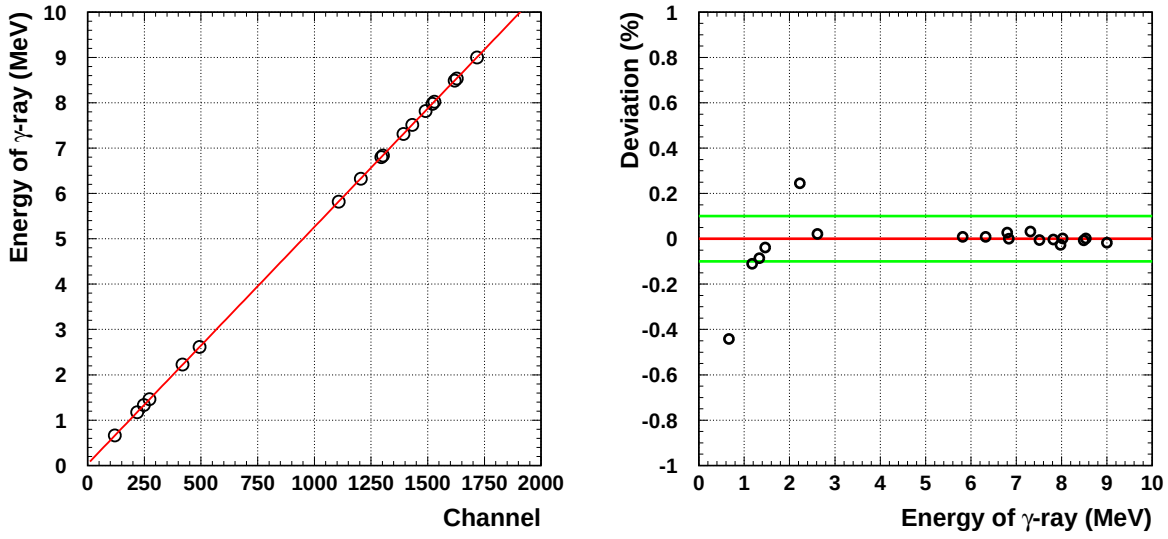

Figure 5.26: The linearity of the germanium detector. The horizontal axis shows the output from the germanium detector [count], while the vertical axis shows the energy of the calibration gamma ray source [MeV]. Deviation of the output of germanium detector count from the fitted line [%] for the solar neutrino energy region gives a difference within 0.1%

.

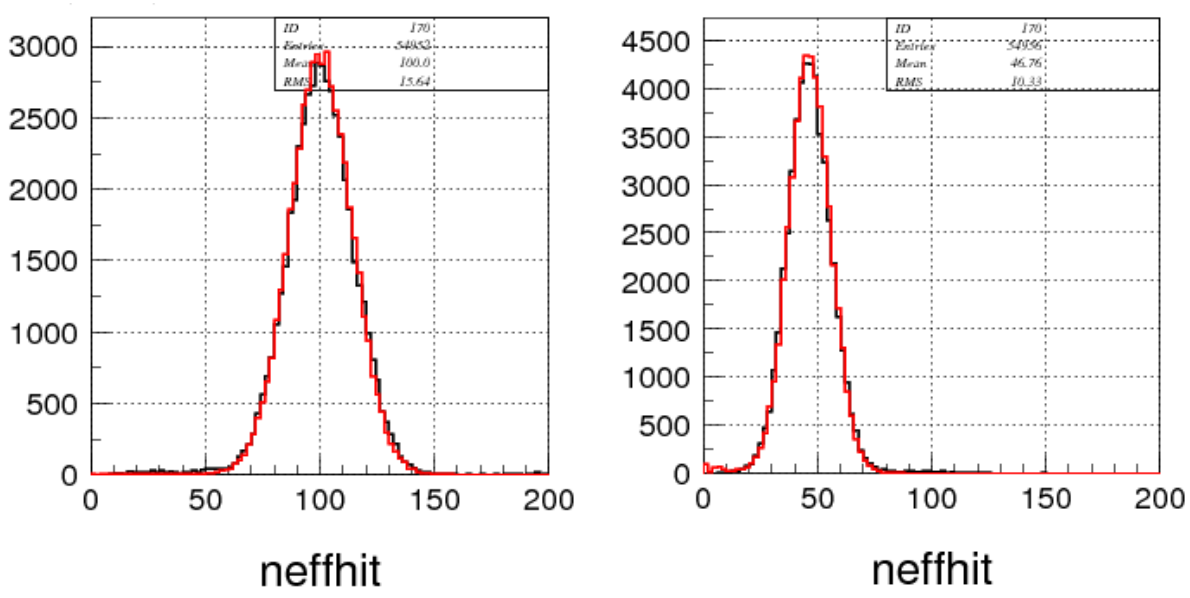

Figure 5.27: N_{eff} for data (black) and MC (red) for 13.6 MeV (left) and 7.0 MeV (right).

LINAC calibration results

Fig.5.27 shows the N_{eff} distributions of both data and MC for the beam endcap position of (-388.9,-70.7,-6) cm. The left figure shows the energy mode of 13.6 MeV and the right shows that of 7.0 MeV. From the peak value of the N_{eff} distribution, we find the COREPMT. The absolute energy scale which is described in section 5.4 is taken from the comparison of Data and MC. The best value of COREPMT is obtained at 0.88 for the SK-IV phase. Fig.5.28 shows the peak value difference between Data and MC.

5.5.2 DT calibration

DT data taking

The DT calibration is done every 3 months. The characteristics of the DT calibration are as follows; the data taking is comparatively easier than that of the LINAC because many more positions can be measured, and the event direction is isotopic.

DT calibration results

Fig.5.29 shows the position dependence difference between DT calibration data and the corresponding MC, in August 2010. The position dependence can be reduced by introducing the position dependence of the water transparency (originally the RMS of the difference was 0.88%), but there still exists a position dependence making up 0.44% of the systematic uncertainty.

Fig.5.30 shows the directional dependence difference between DT data and the correponds MC in August 2010. The directional dependence has been made much lower (0.1%) compared with SK-I (0.5% directional dependence).

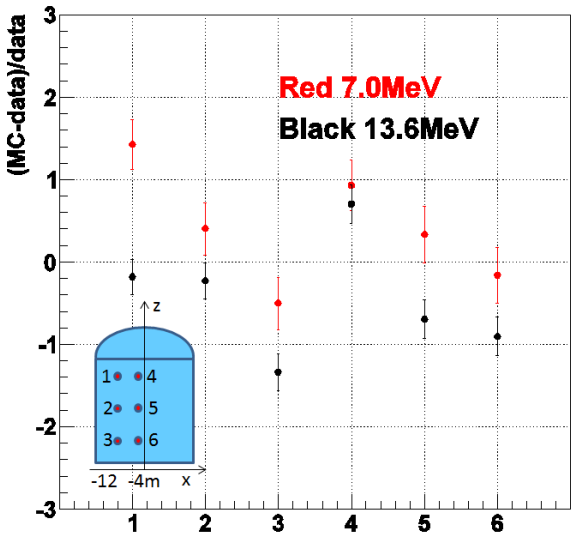

Figure 5.28: The peak value difference of N_{eff} between data and MC for each beampipe position. Vertical axis shows the ratio between MC and data[%].

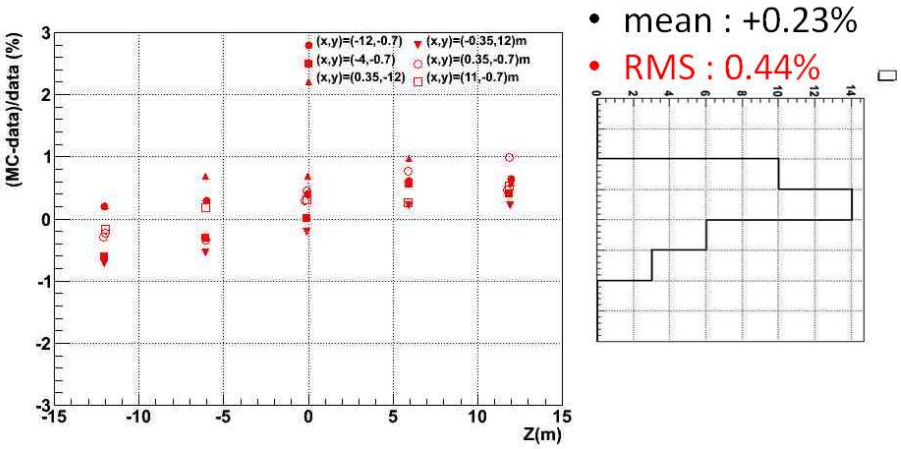

Figure 5.29: The position dependence of DT calibration. Horizontal axis shows the position z[m] and vertical axis shows the ratio between MC and data[%].

.

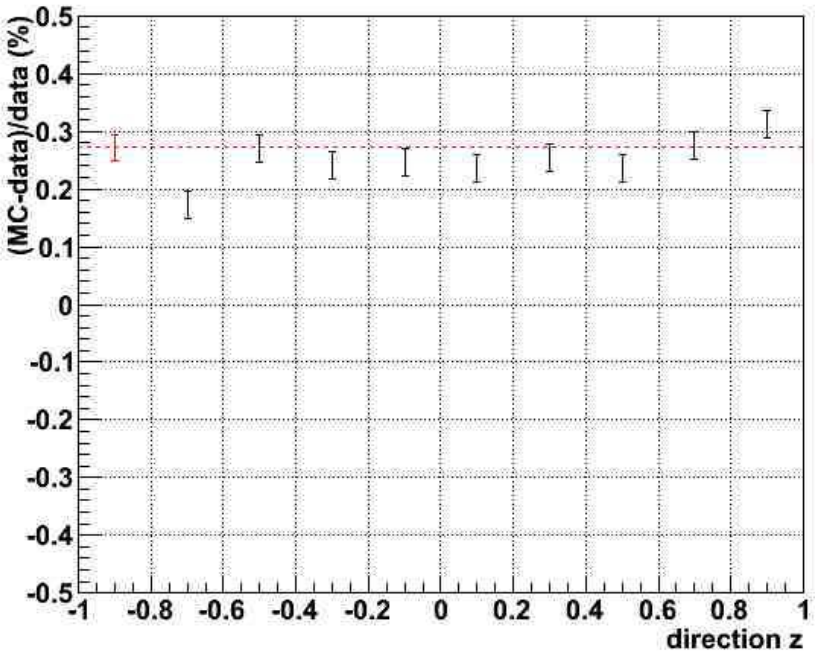

Figure 5.30: The directional dependence of DT calibration. Horizontal axis shows the cosine of the zenith angle and vertical axis shows the ratio between MC and data[%].

.

5.5.3 Systematic uncertainty of absolute energy scale

As descibed in the DT calibration section, the position dependence and directional dependence of the absolute energy scale are 0.44% and 0.1%, respectively. The uncertainty of the electron beam energy determination by the Ge detector is estimated as 0.21% by its calibration, and the water transparency variation during the LINAC calibration is estimated as 0.20%. The total systematic uncertainty of the absolute energy scale is 0.54%, by adding all the contributions in quadrature.

Chapter 6

Data Analysis

After installation of the new data acquisition system in September of 2008, debugging of the system and calibrations were done and start of physics observations marked in October of 2008. In this thesis, the data from October 2008 to March 2012, correponding to a livetime of 1069.3 days, is used. The energy threshold of the SK-IV solar neutrino analysis is set to 4.5 MeV total energy (4.0MeV in kinetic recoil electron energy). To achieve such a low energy threshold, several reduction steps are needed due to the large backgrounds which are listed below. They are much higher event rates than that of the solar neutrino signals. The major background events are as follows;

- Electronics noise.
- PMT flashing.
- Cosmic ray muon.
- Decay-e events from incoming cosmic ray muons.
- Spallation products of cosmic ray muons .
- Radioactivity from the surronding rock, detector materials such as PMTs and their cases.

The solar analysis of SK is designed using total energy. However, other solar neutrino experiments in the world use kinetic energy. So, when we present SK results outside the SK collaboration, we shift the total energy by 0.511 MeV, and present the results using kinetic energy. In this chapter, in order to describe details of the analysis method, total energy is used.

6.1 Run selection

The basic unit of the SK data set is a run. The maximum livetime of one run is set to 24 hours to prevent large data file size. For the SK-III period, the radioactive background level changed greatly, so different energy thresholds were set for different time periods (298.2 livetime days of 5.0 MeV energy threshold and 547.9 livetime days of 5.5 MeV energy threshold). During SK-IV, the background level was kept lower the other periods during the entire period, so all runs are used with a 4.0 MeV energy threshold. The quality of data is checked within each run unit. The selection criteria of bad runs are as follows;

- The run time is less than 5 minutes.

  If one run is very short, there is not enough pedestal data and so it is difficult to judge whether it is a bad run or not. All runs less than 5 minutes are rejected.

- The runs within 15minutes after HV recovered.

  For some calibration data taking, such as LINAC and DT calibrations, the HV needs to be turned off to all PMTs and the SK tank opened. But, soon after HV recovery, the PMTs may still be noisy. So, runs within 15 minutes after the HV is tured on are rejected.

- Hardware and/or software problem happened.

- Calibration and detector maintenance run.

6.2 Pre reduction

If all data were stored, the total data size would be a few hundred GB per day. Almost all of these data is radioactive backgrounds, so it is nesessary to reduce the data size by about 1/100 using a pre reduction. The pre reduction is applied only to obvious background events. Further reduction for solar neutrino analysis is described in the next section.

- Fiducial volume cut:

  Those background events which occurred near the wall of the detector and the reconstructed vertex is near the wall. In the pre reduction, the events which reconstruct within 2 m from the ID wall are cut.

- Gamma ray cut:

  Those background events from PMTs and ID wall inside the fiducial volume. The definition of d_{eff} is the distance from the wall in the direction of the reconstructed event as shown in Fig.6.1. In the pre reduction, $d_{eff} < 400cm$ cut is applied. More tight gamma ray cut is applied below 8MeV.

- Lower energy cut:

  If the reconstructed energy is below 3.5 MeV, these events are rejected in the pre reduction.

- Event quality cut:

  There are background events due to mis-reconstructed events inside the fiducial volume. This cut is to reject events with poor quality in the vertex and direction reconstruction. The two dimensional vertex goodness (g_v) and direction goodness (g_a) distribution is used in this cut. The vertex goodness (g_v) is defined as follows;

$$g_v = \frac{\sum^{hitall} e^{-\frac{1}{2}(\frac{\tau_i(\vec{v})-t_0}{w})^2} e^{-\frac{1}{2}(\frac{\tau_i(\vec{v})-t_0}{\sigma})^2}}{\sum^{hitall} e^{-\frac{1}{2}(\frac{\tau_i(\vec{v}-t_0)}{w})^2}}, \tag{6.1}$$

  where, $\tau_i(\vec{v})$ is a hit time after subtracting the time of flight, t_0 is the fit peak time of the τ distrubution, w is the resolution of the τ diststribution and σ is the timing resolution of the PMT. With this, the vertex goodness is the degree of quality of vertex reconstruction

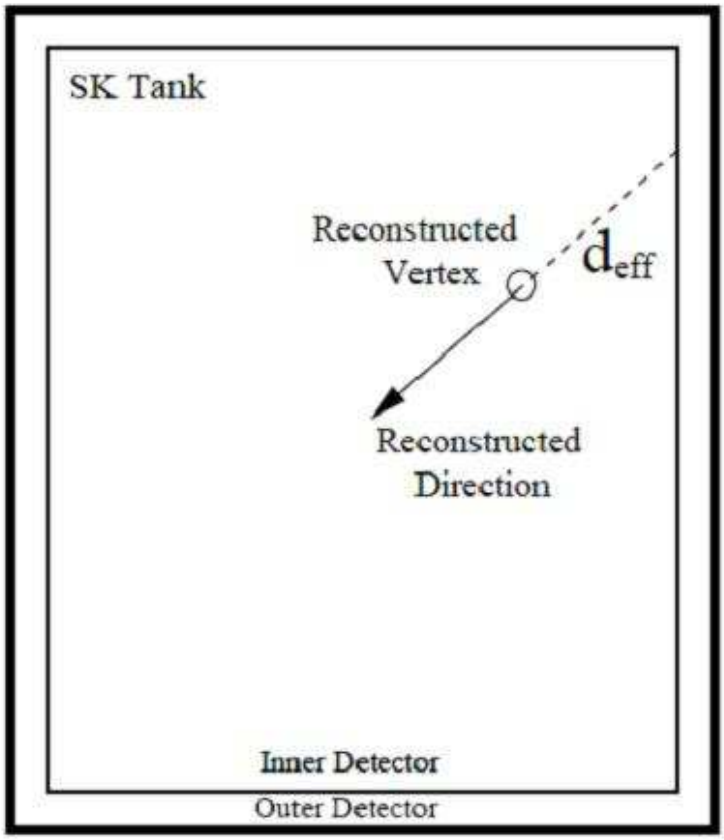

Figure 6.1: Definition of d_{eff}

	number of events	efficiency
before cut	197,524	100%
loose fiducial cut	28,161	14.2%
loose gamma ray cut	14,864	7.5%
lower energy cut	6,872	3.5%
loose event quality cut	2,057	1.0%

Table 6.1: The reduction step and efficiencies of pre reduction.

estimated by the hit PMTs timing information, the value of g_v ranges from 0 to 1, and if this value is close to 1, the quality of the vertex reconstruction is better. The direction goodness (g_a) is defined as follows;

$$g_a = \frac{max\{\angle_{uniform}(i) - \angle_{Data}(i)\} - min\{\angle_{uniform}(i) - \angle_{Data}(i)\}}{2\pi}, \tag{6.2}$$

where, $\angle_{uniform}(i)$ is the azimuthal angle of i-th hit PMT, assuming that the hit PMTs are uniformly distrbuted along a Cherenkov cone, and $\angle_{Data}(i)$ is that of the real angle. The value of g_a ranges from 0 to 1, and if the event is a good event, this value is close to 0. An example of a good event (low direction goodness value) and a bad event (high direction goodness value) are shown in Fig.6.2 .

Fig.6.3 shows the correlation between the square of the vertex goodness(g_v^2) and the direction goodness(g_a^2). The left figure shows the data just after the 2 m fiducial volume cut and the 4 MeV cut, which contains a lot of badly reconstructed events, and the right figure shows the DT calibration data. The line shows the function of $g_v^2 - g_a^2 = 0.25$. From these figures, good single electron like events can be separated from background events by using the value of $g_v^2 - g_a^2$. In the pre reduction, events with $g_v^2 - g_a^2 < 0.1$ are cut. Further cuts will be described later.

The number of events after each pre reduction for one 24 hour run is summarized in Table 6.1. For these cuts, the data size can be reduced by 1/100. The reduction efficiency for the solar neutrino MC simulation by these cuts is shown in Fig.6.17, and is about 5% above 6 MeV.

6.3 Reduction steps for the solar analysis

6.3.1 Total number of hit PMT cut

If the total number of hit PMTs of one event (N_{TOT}) exceeds 400, the energy will be much larger than that of solar neutrino signals. N_{TOT}=400 corresponds to about 60 MeV for an electron type event. By this cut, most of the cosmic ray muons are also rejected.

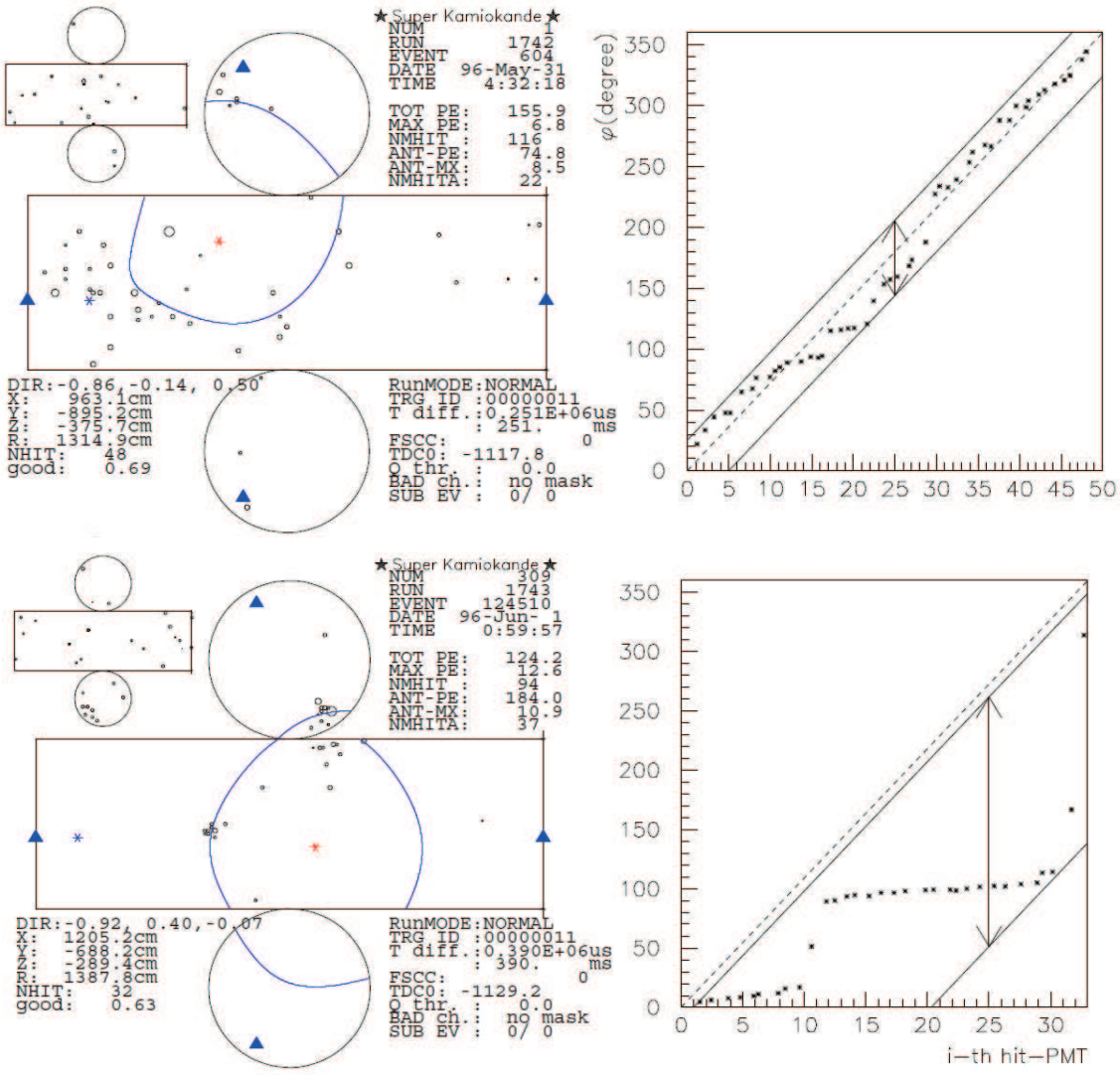

Figure 6.2: Example of a good event (top) and a bad event (bottom).

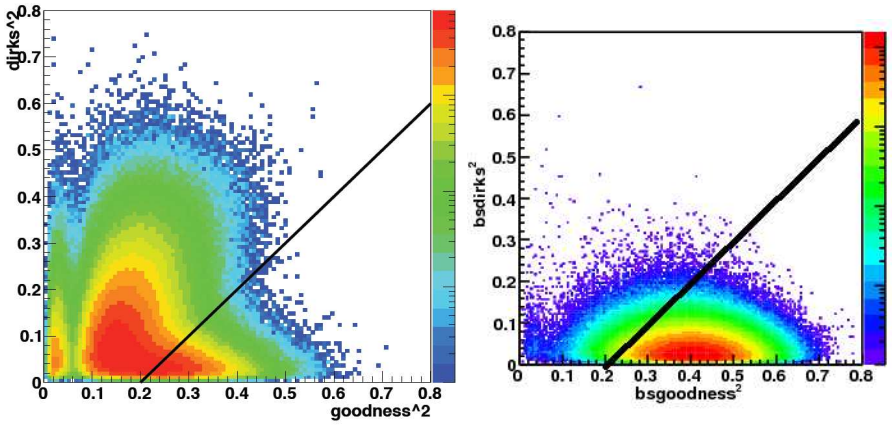

Figure 6.3: Correlation between g_v^2 (horizontal) and g_a^2 (vertical). The line shows the function of $g_v^2 - g_a^2 = 0.25$. Left figure shows the background sample and right figure shows the solar MC.

6.3.2 Trigger cut

Events which are triggered by scheduled events are rejected. There are auto calibration events [1], which are used for timing and water calibration, and the so-called LED-bursts which are used as a test for supernova burst events and happen once every ∼three weeks. Pedestal events to adjust the pedestal of the electronics, happen once every 30 minutes. Those scheduled events have external triggers and they are flagged by the electronics.

6.3.3 Flasher cut

When one PMT emits light due to arc discharge on the dynodes, other PMTs also get pick up the signal, and this is referred to as a 'flasher event'. The characteristics of flasher events are that one PMT contains a large charge hit and there are many hit PMTs surrounding that PMT. Fig.6.4 shows the two dimensional plot of the maximum charge of a PMT in an event and the number of hits in the surrounding 24 PMTs. If the maximum charge of a PMT is greater than 50 [p.e.] and the number of hits in the surrounding 24PMTs is greater than 3, the event is regarded as flasher event and rejected.

6.3.4 Time difference cut

Events which occurred within 50 μsec from the previous LE triggered event are rejected. By this cut, ringing events after high energy events, such as cosmic ray muons, and events which are caused by after pulses and decay-e events are rejected.

6.3.5 Spallation cut

Some cosmic ray muons produce radioactive elements by breaking up an oxygen nucleus. The reaction can be written as

[1] calibration events which are automatically triggered during usual runs

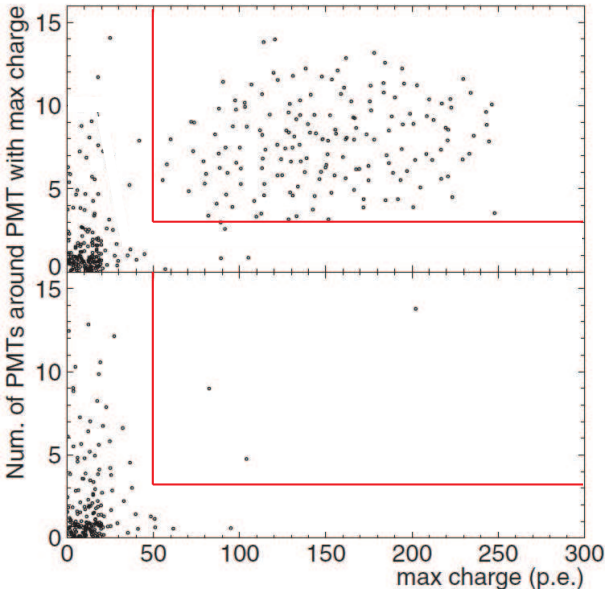

Figure 6.4: Cut criteria for flasher events. The horizontal axis shows the maximum charge of a PMT in an event and the vertical axis shows the number of hits in the surronding 24 PMTs. The top figure shows one run which has flasher events and the bottom figure shows a typical good run.

$$\mu + {}^{16}O \rightarrow \mu + X + \cdots , \tag{6.3}$$

where X is a radioactive nucleus. Also, hadrons ($\pi^{\pm}$, n, p, etc), which are produced by hadronic cascades induced by muon interactions, are captured by other oxygen nucleus and radioactive nucleus can be produced. They are summarized in Table 6.2. When those nuclei decay, βs and/or γs are emitted with a lifetime in the range of 0.001 to 14 sec. These β and γ events are called spallation events. The energy of spallation events is similar to those from solar neutrino signals, so the spallation event is one of the major backgrounds in the solar neutrino analysis. To identify such spallation events, a likelihood method is used. The likelihood is defined as

$$\mathcal{L}_{spa} = f(\Delta T) \times f(\Delta L) \times f(Q_{res}). \tag{6.4}$$

The parameters for the likelihood function are as follows;

- ΔT: Time difference between the spallation candidate event and the proceeding muon event.
- ΔL: Distance from the reconstructed vertex of the spallation candidate event to the reconstructed track of the proceeding muon event.
- Q_{res}: Residual charge of the proceeding muon event which is defined as

$$Q_{res} = Q_{obs} - Q_{unit} \times L, \tag{6.5}$$

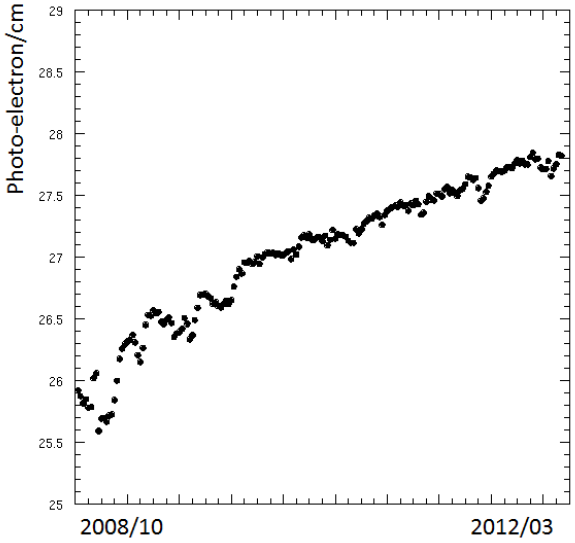

Figure 6.5: Time variation of the observed charge per cm for muons.

where Q_{obs} is the total number of photo-electrons from the proceeding muon, Q_{unit} is the average of the observed charge per cm and L is the reconstructed track length of the proceeding muon event. Because of the time variation of the water transparency and the PMT gain depndence, Q_{unit} changes time to time. Fig.6.5 shows time dependence of Q_{unit}. If a muon make a spallation event, Q_{obs} is often much greater than the expected observed charge(Q_{unit}×L), i.e. $Q_{res} \gg 0$, because the spallation process often happens with a hadronic casade shower.

Also in spallation events, the values of ΔT and ΔL would be smaller than random sample. Those features are reflected in the likelihood method.

The likelihood function of $f(\Delta T)$ is generated by considering the lifetime of the produced radioactive elements. The likelihood functions of $f(\Delta L)$ and $f(Q_{res})$ are generated using two real data samples, a spallation-like sample and a random sample. The spallation sample is composed of events with ΔT $<$ 0.1sec and energy $>$ 8 MeV, and the random sample is composed of events with energy $<$ 5 MeV and assigned random vertex and direction, because most of the low energy events are produced by radioactive sources from the ID wall and not by spallation. The bottom figure of Fig.6.6 shows the calculated log likelihood distribution of the spallation-like sample (black) and the random sample (red). The point of the spallation cut is determined so that the dead time of the random sample is 20%. The cut point is determined to be log(likelihood)=4.52. The position dependence of the dead time is shown in Fig.6.7. This position dependence of the dead time is taken into account when the expected number of solar neutrino events is calculated in the Monte Carlo simulation.

6.3.6 g_v^2-g_a^2 cut

The criteria of the event quality cut, called g_v^2-g_a^2 cut, is determined by calculation of the significance which is defined as follows;

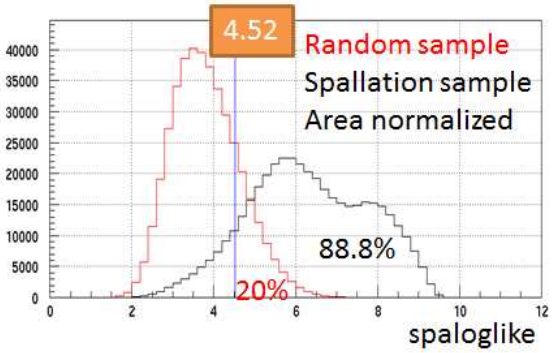

Figure 6.6: The likelihood distribution of the spallation-like sample (black) and the random sample (red). The horizontal axis shows the log(likelihood).

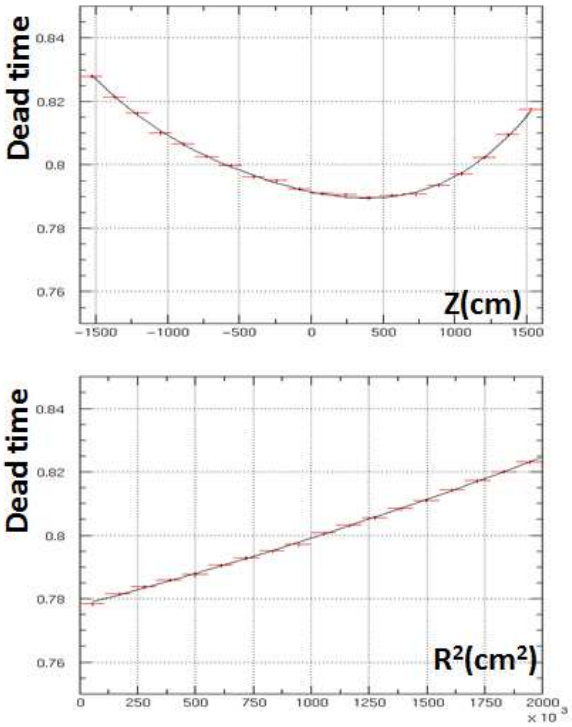

Figure 6.7: The position dependence of the dead time of the spallation cut. The horizontal axis of the top figure is the detector position z[cm] and that of the bottom figure is the radius squared($r^2[cm^2]$).

Isotope	$\tau_{\frac{1}{2}}$(sec)	decay mode	Kinetic Energy (MeV)
$^{8}_{2}He$	0.119	β^-	9.67 + 0.98(γ)
		β^- n	16%
$^{8}_{3}Li$	0.838	β^-	$\sim$ 13
$^{8}_{3}B$	0.77	β^+	13.9
$^{9}_{3}Li$	0.178	β^-	13.6 (50.5 %)
		β^- n	($\sim$ 50 %)
$^{9}_{6}C$	0.127	β^+ n	3$\sim$15
$^{11}_{3}Li$	0.0085	β^-	16$\sim$20 ($\sim$ 50 %)
		β^- n	$\sim$ 16 ($\sim$ 50 %)
$^{11}_{4}Be$	13.8	β^-	11.51 (54.7 %)
			9.41 + 2.1 (γ) (31.4 %)
$^{11}_{4}Be$	0.0236	β^-	11.71
$^{12}_{5}B$	0.0202	β^-	13.37
$^{12}_{7}N$	0.0110	β^+	16.32
$^{13}_{5}B$	0.0174	β^-	13.44
$^{13}_{8}O$	0.0086	β^+	13.2 16.7
$^{14}_{5}B$	0.0138	β^-	14.55+6.09 (γ)
$^{15}_{6}C$	2.449	β^-	9.77 (36.8 %)
			4.47+5.30 (γ)
$^{16}_{6}C$	0.747	β^- n	$\sim$ 4
$^{16}_{7}N$	7.13	β^-	10.42 (28.0%)
			4.29+6.13 (γ) (66.2%)

Table 6.2: Radioactive elements which are produced by Spallation in water

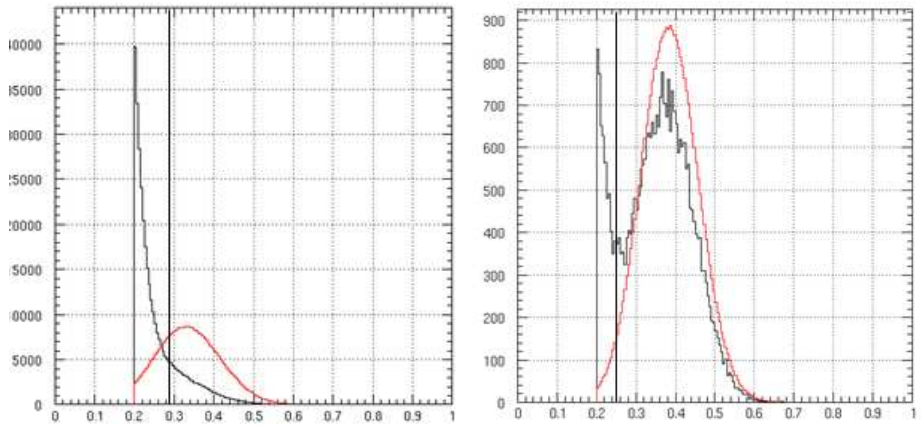

Figure 6.8: $g_v^2 - g_a^2$ distriubtions of the data (black) and the solar neutrino MC (red) for 4.5-5.0 MeV (left figure) and 6.5-7.0 MeV (right figure). Black line shows the criteria of the $g_v^2 - g_a^2$ cut.

$$\frac{\text{(Efficiency for solar neutrino)}}{\sqrt{\text{(Backgrounds)}}}.$$

Fig.6.8 shows the g_v^2-g_a^2 distriubtions of the data (black) and the solar neutrino MC (red) for 4.5-5 MeV (left figure) and 6.5-7.0 MeV (right figure). From the significance of these energy dependence distributions, the criteria of the g_v^2-g_a^2 cut is as follows:

$$\begin{cases} g_v^2 - g_a^2 > 0.29, \ 4.0 \leq Energy < 5.0MeV \\ g_v^2 - g_a^2 > 0.25, \ 5.0 \leq Energy < 7.5MeV \\ g_v^2 - g_a^2 > 0.20, \ Energy \geq 7.5MeV \end{cases} . \tag{6.6}$$

6.3.7 Hit pattern cut

When an event which consists of multiple γ and/or β rays, i.e. spallation products of ^{16}N decays give a Cherenkov ring image which is not a clear single ring pattern. To distinguish a single electron event coming from the solar neutrino signal and not from such βs and/or γs, a likelihood of the hit pattern is used. The definition of the likelihood is as follows;

$$\mathcal{L}_{pattern}(Energy, vertex, diretion) = \frac{1}{N_{50}} \sum_{i}^{N_{50}} \log(P(i, Energy, \cos\theta_{PMT}, f_{wall})), \tag{6.7}$$

where P is a probability density function of the hit pattern, made by a single electron MC. P is a function of the angle between the reconstructed direction and the angle from the reconstructed vertex to each hit PMT ($\cos\theta_{PMT}$), energy, and the effective distance between the wall and the reconstructed vertex point (f_{wall}). The schematic view of $\cos\theta_{PMT}$ and f_{wall} is shown in Fig.6.9.

Fig.6.10 shows $\mathcal{L}_{pattern}$ for data (black) and solar neutrino MC (red) for each energy range. The criteria of the hit pattern cut is as follows;

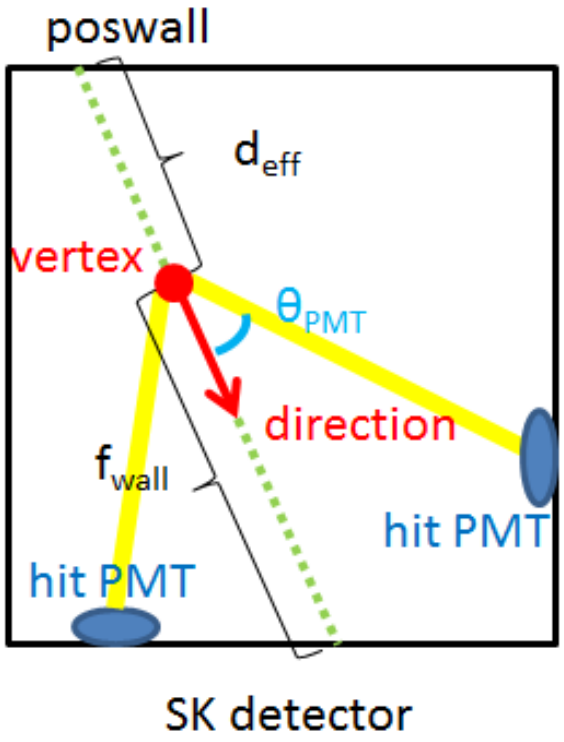

Figure 6.9: Definition of θ_{PMT} and f_{wall}.

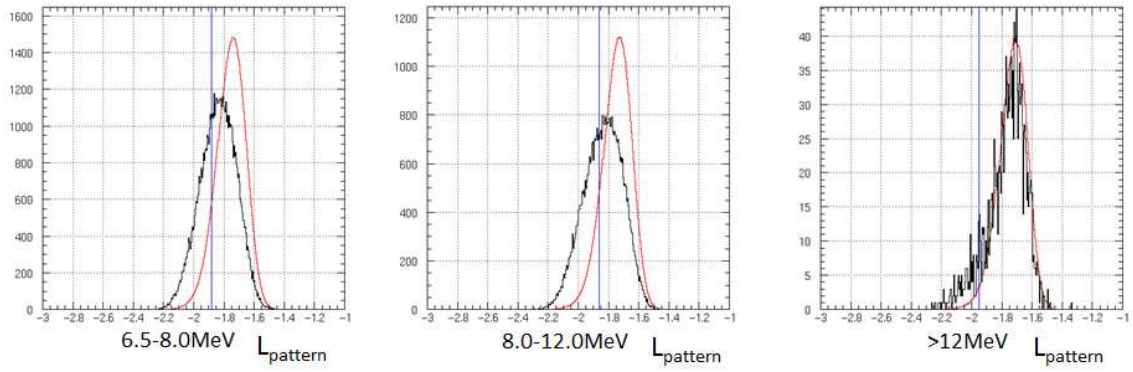

Figure 6.10: $\mathcal{L}_{pattern}$ of data(black) and solar neutrino MC(red) for 6.5-8.0 MeV (left), 8.0-12.0 MeV (middle) and >12 MeV (right). Bule line shows the criteria of hit pattern cut for each energy region.

$$\begin{cases} P > -1.88, & 6.5 \leq Energy < 8.0MeV \\ P > -1.86, & 8.0 \leq Energy < 12.0MeV \\ P > -1.95, & 12.0MeV \leq Energy \end{cases} \tag{6.8}$$

Below 6.5 MeV, it is difficult to distinguish a single electron event and background events because of the smaller number of hit PMTs, so this hit pattern cut is applied above 6.5 MeV.

6.3.8 Gamma ray cut

Fig.6.11 shows the d_{eff} distribution for 5.5-8.0 MeV and 8.0-8.5 MeV. The criteria of the gamma cut is as follows;

$$\begin{cases} d_{eff} > 650cm, & 6.5 \leq Energy < 8.0MeV \\ d_{eff} > 400cm, & 8.0MeV \leq Energy \end{cases} \tag{6.9}$$

Because the radioactive background is not uniformly distributed, a tight fiducial volume cut, which is described in section 6.3.11, is needed. In the determination of the cut point of the gamma ray cut below 5.5 MeV, events which are reconstructed in the central area (position z > -10[m] and r < 13[m]) are used. The criteria are individually determined depending upon the nearest wall of the detector, which is either top, barrel or bottom, named poswall hereafter and defined in Fig.6.9. Fig.6.12 shows the d_{eff} distribution in the 4.5-5.0 MeV region, for each poswall. The criteria of the gamma cut for the lower energy region (4.0-5.5MeV) are as follows;

$$\begin{cases} d_{eff} > 1000cm, & \text{poswall is top} \\ d_{eff} > 1200cm, & \text{poswall is barrel} \\ d_{eff} > 1300cm, & \text{poswall is bottom} \end{cases} \tag{6.10}$$

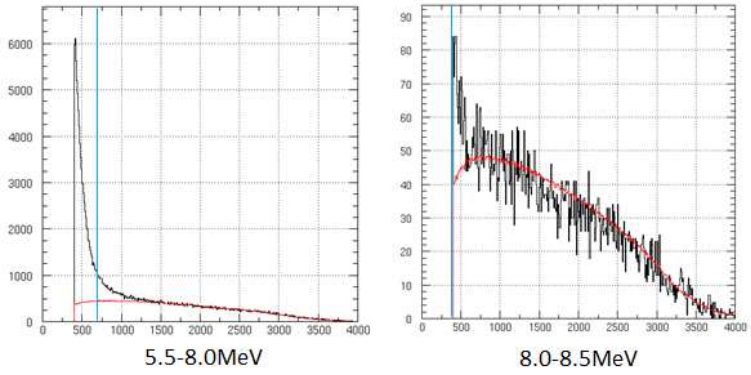

Figure 6.11: d_{eff} distributons of data(black) and solar MC(red) for each energy region. These distributions are scaled suitably. Blue line shows the criteria of gamma ray cut for each energy region.

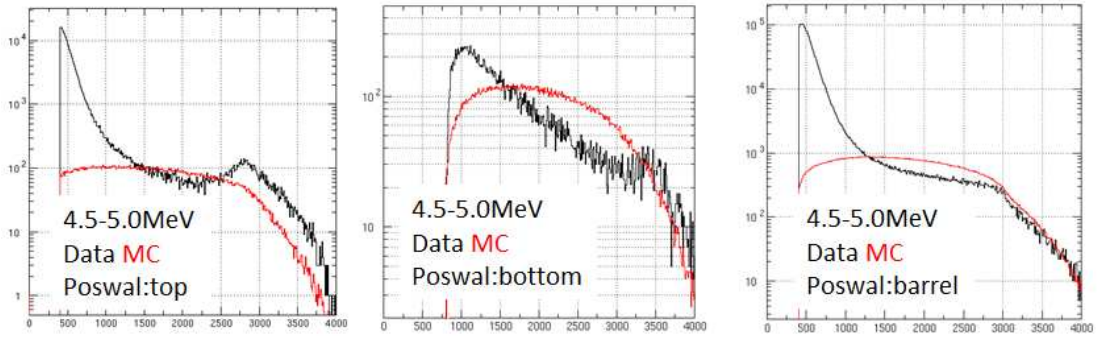

Figure 6.12: d_{eff} distributons of lower energy region for each poswal. The situation is the same as Fig.6.11.

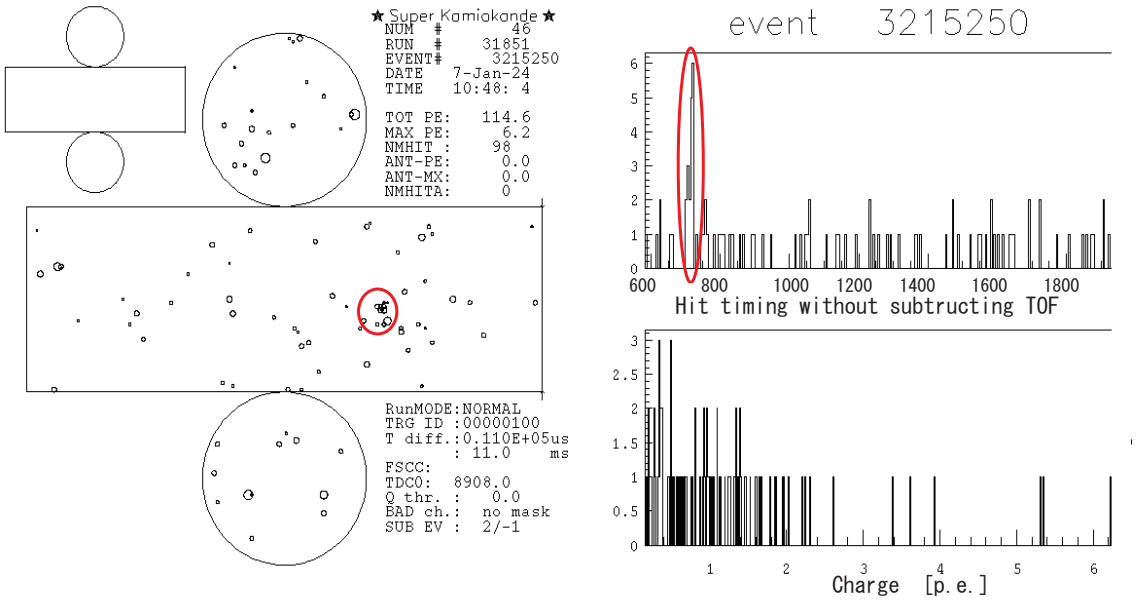

Figure 6.13: An example of a cluster hit event.

6.3.9 ^{16}N cut

When lower energy μ^- cosmic rays are captured by ^{16}O in the detector, ^{16}N can be produced. ^{16}N decays with gamma-rays and/or electrons with the half-life of 7.13 seconds. The main decay mode is a 6.1 MeV gamma and a 4.3 MeV electron (66%) or a 10.41 MeV electron(28%). In order to reject these events, the correlation between stopping muons in the detector and the remaining candidate events are checked. In order to select only captured muons from the stopping muon sample, stopping muons which did not accompany an event within 100 μsec are selected. Then the candidate events which satisfy the following criteria are rejected; (1) reconstructed vertex is within 335 cm from the stopping point of the muon, (2) the time difference is between 100 μsec and 30 sec. The dead time of the ^{16}N cut is estimated to be 0.53% from accidental coincidence between the selected stopping muons and the random sample events.

6.3.10 Cluster hit event cut

This cut rejects events which are triggered by accidental coincidence of dark noise hits and small clusters of hits due to radioactive impurities on the detector wall. They are called cluster hit events. Fig.6.13 shows one example of a cluster hit event. Solar neutrino events which occur near the edge of detector also make small culsters, but compared with cluster hit events, the radius of the solar neutrino cluster is larger than these background events. So using the size of the cluster, one can distinguish solar neutrino events and cluster hit events.

There are two parameters to evaluate the size of cluster, '$R02$' and '$N20_{rawT}$'. $R02$ is the size of the clustering hits in space and is defined to be the minimum radius such that more than 20% of hit PMTs are contained within a sliding 20 nsec window. $N20_{rawT}$ is the clustering of hits in time, which is defined as the maximum number of hits within a 20 nsec 'raw' timing window, without subtracting the time of flight from the reconstructed vertex. The reason for

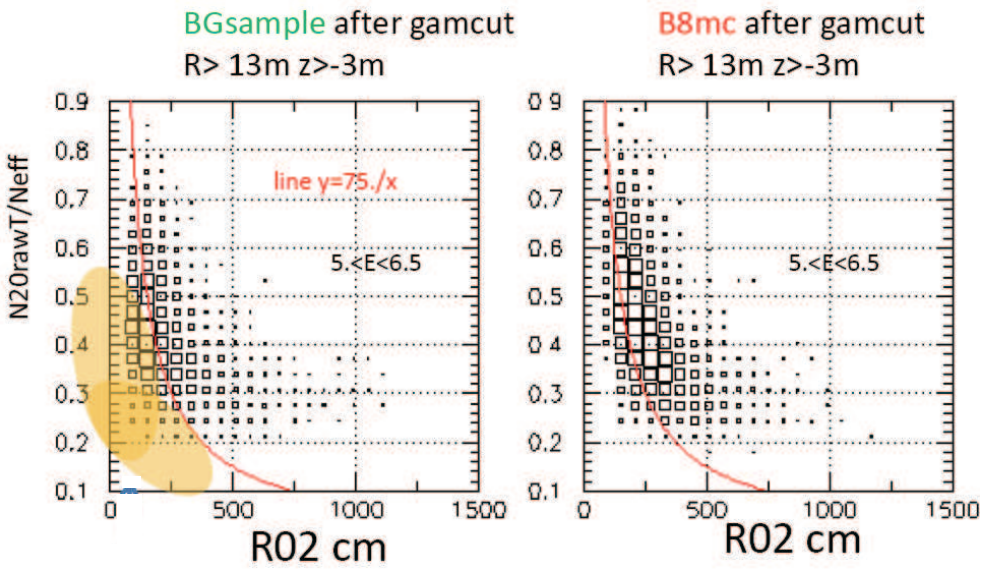

Figure 6.14: Relationship between $R02$ and $N20_{rawT}$ for background (left) and solar neutrino MC (right).

this is that for backgrounds which hit PMTs outside of a cluster are randomly distributed. The number of $N20_{rawT}$ divided by total number of hits, $N20_{rawT}/N_{eff}$, is expected to be a smaller than that of solar neutrino signal.

Fig.6.14 shows the relationship between $R02$ and $N20_{rawT}/N_{eff}$ for background and solar neutrino MC events, around the edge of fiducial volume. The definition of a parameter called CLIK, which is used by this cluster hit event cut, is as follows;

$$\text{CLIK} = R02 \times N20_{rawT}/N_{eff}. \tag{6.11}$$

And the criteria of the cluster hit event cut are as follows;

$$\begin{cases} CLIK < 75, r^2 > 155m^2, z < -7.5m, & \text{for 5.0 } \leq\text{E}< \text{5.5 MeV} \\ CLIK < 75, r^2 > 120m^2, z < -3m \text{ or } z > 13m & \text{for 4.0 } \leq\text{E}< \text{5.0 MeV} \end{cases} \tag{6.12}$$

6.3.11 Tight fiducal volume cut

Fig.6.15 shows the vertex distribution for the lower energy range. Even though several cuts are applied, there still remain backgrounds in the bottom and edge of the barrel regions. The uniformity of the vertex distribution is important because a non-uniform background shapes makes large systematic uncertainty, especially for the day-night analysis of the solar neutrino flux. Based on a significance calculation, the 1st fiducial volume cut is applied below 5.5 MeV as

$$R^2 < 180m^2 \text{ and } z > -7.5m = 13.3kton, \tag{6.13}$$

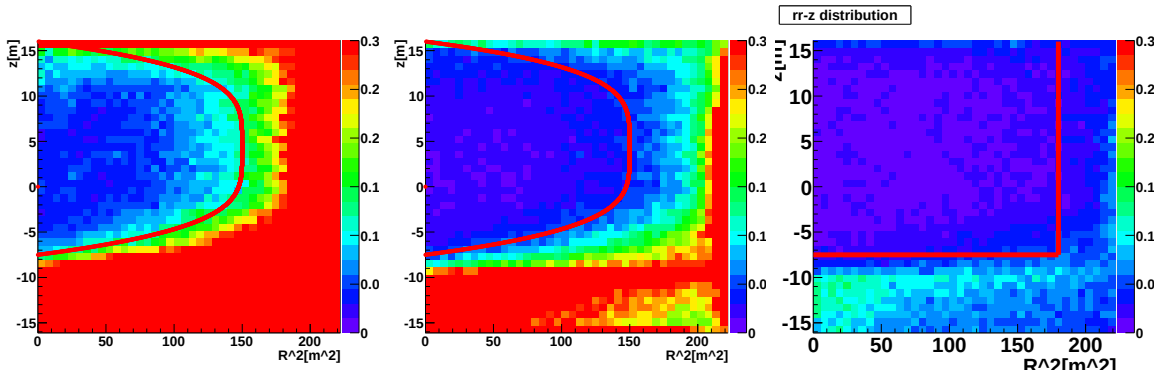

Figure 6.15: Vertex distribution of 4.0-4.5 MeV (left), 4.5-5.0 MeV (middle) and 5.0-5.5 MeV (right). The tight fiducial volume cut is shown with the red curve.

which is shown in the right portion of Fig.6.15. But a more oval like tight fiducial volume cut is needed below 5.0 MeV. So the new tight fiducial volume shape is described as

$$(x^2 + y^2) + (\frac{150}{11.75^4} * |z - 4.25|^4) \leq 150, \tag{6.14}$$

is applied. The fiducail volume below 5.0 MeV is 8.8 kton. Above 5.5 MeV, no tight fiducial volme cut is needed and the fiducial volume is 22.5 kton.

6.4 Summary of reduction step

Fig.6.16 shows the energy spectrum of each reduction step and Fig.6.17 shows the remaining event efficiency of the ^8B solar neutrino MC. Both figures also show the SK-III final sample. Above 6.5 MeV, the remaining efficiency of the final sample is almost the same level as SK-III, while for 5.5-6.5 MeV the SK-IV remaining efficiency is better than SK-III, which is caused by a looser gamma ray cut and removal of the cluster hit cut. Below 5.5 MeV, the SK-III remaining efficiency is better than that of SK-IV, caused by the additional tight $g_v^2 - g_a^2$ cut for 5.0-5.5 MeV and a tighter fiducial volume cut for 4.0-5.0 MeV. Fig.6.18 shows the time variation of the final data sample for SK-III and SK-IV. By improvements of the water circulation system, which is described in Sec.3.3.2, a continuous lower background level is achieved in SK-IV period.

6.5 Signal extraction method

In the case of ν-e interactions of solar neutrino signals, the incident neutrino and recoil electron directions are highly correlated. Fig.6.19 shows the $cos\theta_{sun}$ distribution for events between 4.5-20 MeV, where $cos\theta_{sun}$ is the direction between the sun and the reconstructed direction, which is defined in Fig.6.20. A clear peak due to solar neutrinos can be seen. The flat component in the $cos\theta_{sun}$ distribution is due to remaining background, such as spallation products and of surrounding rock and so on. In this section, the method of the solar neutrino signal extraction is described.

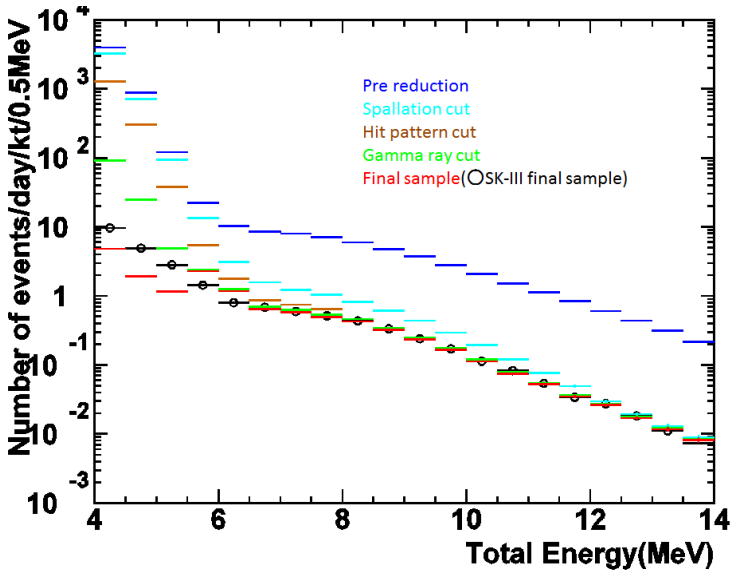

Figure 6.16: Energy distribution for each reduction step. The 1st reduction of SK-IV corresponds to the pre reduction and that of SK-III corresponds to a precut which is explained in this thesis.

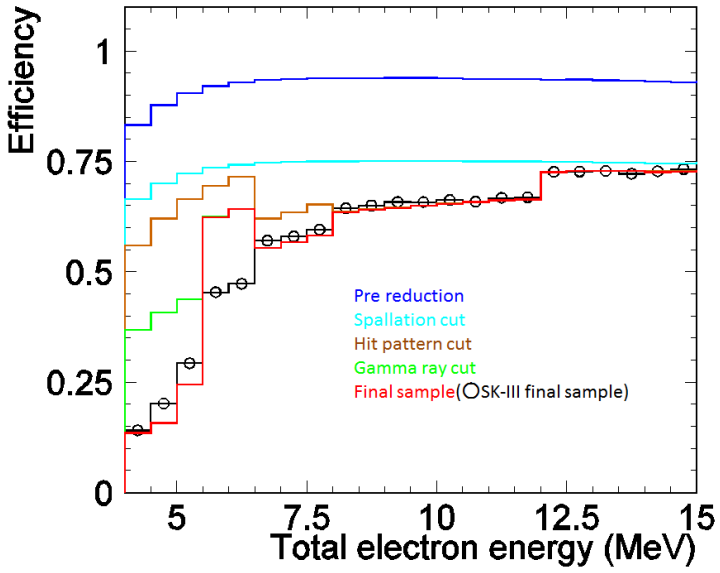

Figure 6.17: Reduction efficiency for the solar neutrino MC simulation.

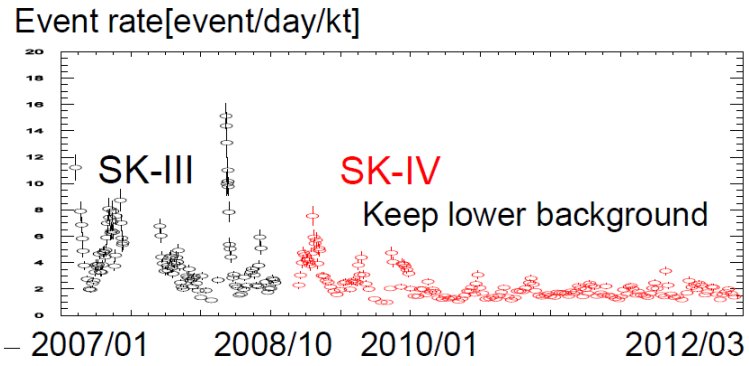

Figure 6.18: The event rate of the final data sample for SK-III (black) and SK-IV (red).

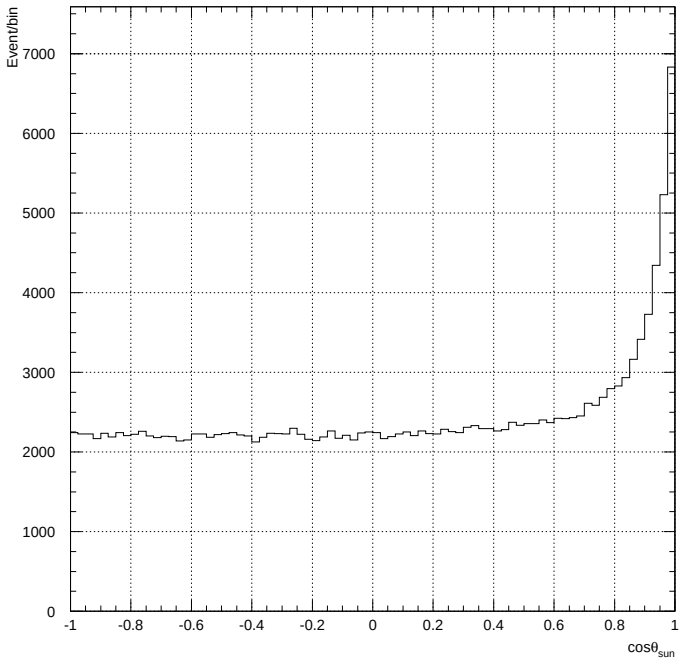

Figure 6.19: $cos\theta_{sun}$ distribution for events between 4.5-20 MeV.

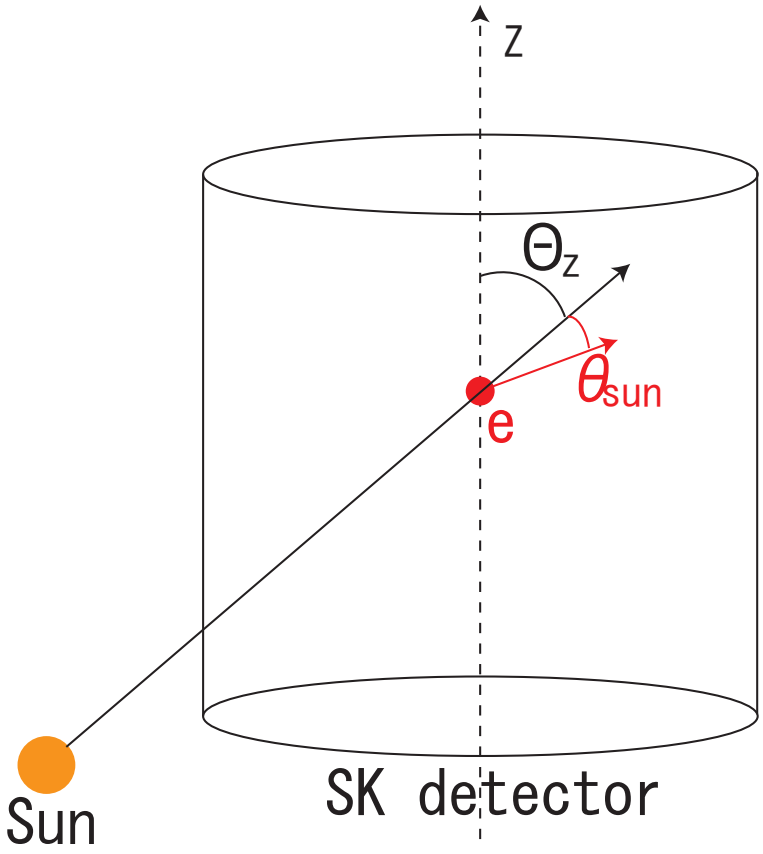

Figure 6.20: The definition of $cos\theta_{sun}$.

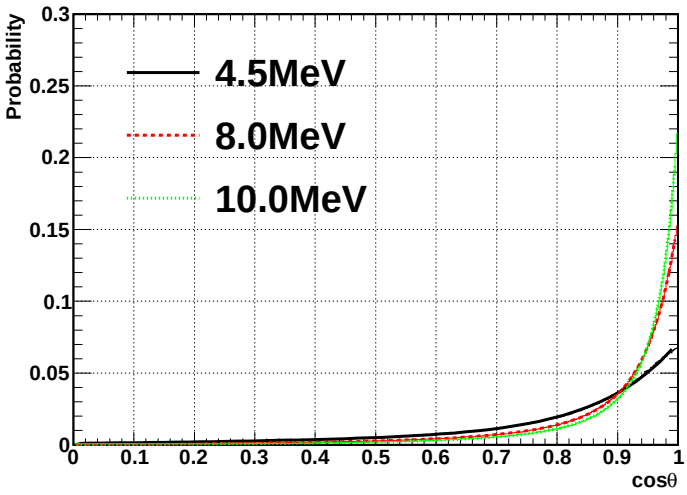

Figure 6.21: The probability density function of the signal(s_{ij}) for given energy.

In order to obtain the measured flux based on the SSM, an extended maximum likelihood method is used. The likelihood function is defined as;

$$\mathcal{L} = e^{-(\sum_i B_i + S)} \prod_{i=1}^{N_{bin}} \prod_{j=1}^{n_i} (B_i \cdot b_{ij} + S \cdot Y_i \cdot s_{ij}), \tag{6.15}$$

where N_{bin} is the number of bins between 4.0 MeV and 20.0 MeV. For SK-IV, N_{bin}=23 is used, where the bin width is 0.5MeV from 4.0 to 14.0 MeV and 1.0MeV bin width is used from 14.0 to 16.0 MeV. The last bin goes from 16.0 to 20 MeV. n_i is the number of observed events in the i-th energy bin. S and B_i are the free parameters of this likelihood function and are the total number of observed solar neutrino events and the number of background in the i-th energy bin, respectively. Y_i is the expected fraction of signal event in the i-th energy bin, estimated by solar neutrino MC. The probability density functions b_{ij} and s_{ij} are the expected shapes of the background and solar neturino signal, respectively. The background shape, b_{ij}, is based on the zenith and the azimuthal angular distribution of real data. Namely, these detector oriented angular distributions are fit with polynomial functions, and then converted to the $cos\theta_{sun}$ coordinate. b_{ij} is not a completely flat shape because of the effect of cylindrical shape of the detector and the effect of the zenith and azimuthal dependence of the background distribution. The expected solar neutrino signal shape, s_{ij} is obtained by the solar neutrino MC by fitting the $cos\theta_{sun}$ distributions with a triple exponential plus a Gaussian. Fig.6.21 shows the obtained s_{ij} probability density function for 4.5 MeV, 8.0 MeV and 10.0 MeV, while Fig.6.22 shows the b_{ij} probability density function. Finally, the values of S and B_i are obtained by the maximum likelihood method.

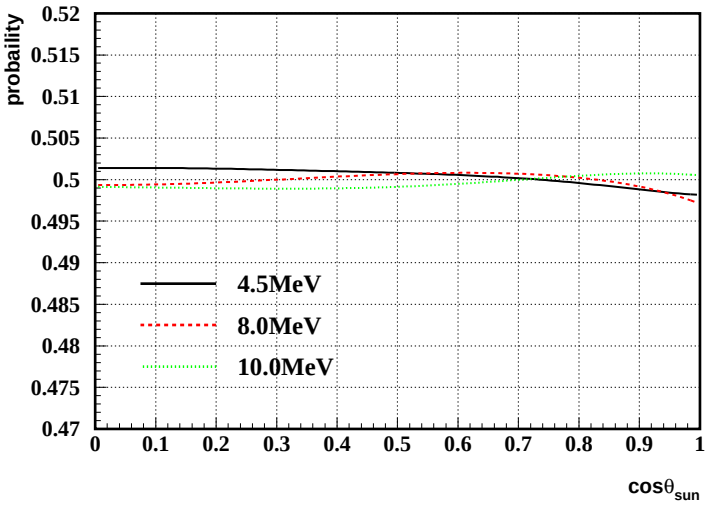

Figure 6.22: The probability density function of the background(b_{ij}) for a given energy.

6.6 Multiple scattering goodness

There are still remaining backgrounds in the lower energy region, even after applying reductions which were described in this chapter. The main background comes from radioactive impurities in the detector, with the most likely source coming from ^{214}Bi decays into beta rays which have a 3.3 MeV endpoint energy. Because of the finite (about 20% for 4.0MeV electron) energy resolution, those beta rays can be reconstructed above 4.0 MeV. However, they should have incurred more multiple scattering in water than true 4.0 MeV electrons. The degree of multiple scattering is evaluated using a 'multiple scattering goodness (MSG)' which is calculated by the following method.

- Select the pairs of hit PMTs within a 20 nsec window from the initial event time, after time of flight subtraction. The two vectors from the vertex to each hit PMTs, r_i and r_j are considered 'hit direction's.
- For each pair of hit PMTs, 2 cones which have 42° opening angles from the vertex are projected and the counted number of intersecting points of the two cones on the detector surface gives zero, one or two. Fig.6.23 shows the case of the two intersection case.
- For pairs of PMTs with two intersection points, the vector from the vertex to each of the intersection points is taken as a 'unit vector', which has one unit length. we find all the candidates of 'unit vectors' by selecting all the possible pairs of hit PMTs within a 20 nsec window.
- For all candidates of 'unit vectors', the 'sums vector' is calculated by forming vector sums of the 'unit vectors' which are within 50° of one candidate 'unit vector'. The longest 'sums vector' is defined as the 'best direction vector' and we then sum the 'unit vectors' which

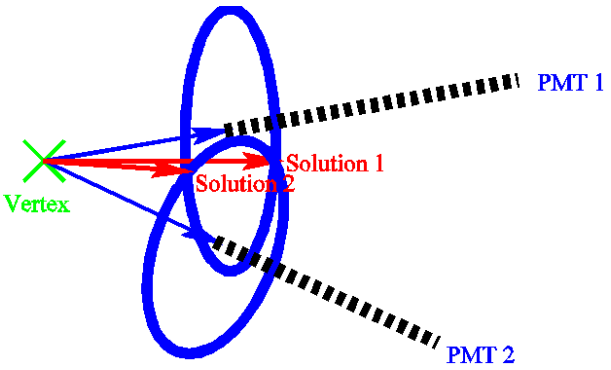

Figure 6.23: The schematic view of cones which have 42° opening angles from the vertex and the number of intersection points.

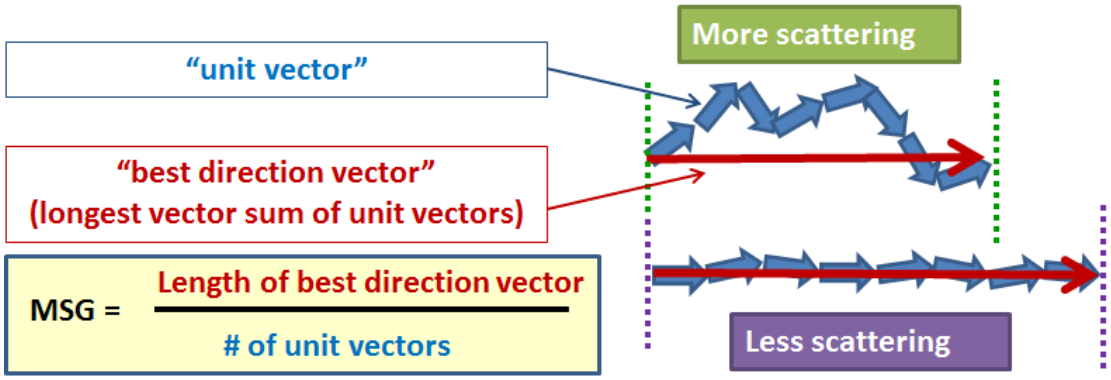

Figure 6.24: The schematic view of the 'unit vector' and the 'best direction vector' for more and less scattering events.

forming the 'best direction vector' along the 'best direction'. The schematic view of the 'unit vector' and the 'best direction vector' for the more or less scattering cases are shown in Fig.6.24

- The MSG value is defined as follows;

$$MSG = \frac{\text{Length of best direction vector}}{\text{number of unit vector}} \tag{6.16}$$

The MSG value ranges from 0 to 1, with higher real energy electrons having a higher MSG value.

The events below 7.5 MeV are divided into three MSG groups, low MSG (MSG<0.35), middle MSG (0.35≥MSG≥0.45) and high MSG (MSG>0.45), and then the signal extraction is executed. By dividing into 3 groups, the effective signal extraction can be improved because the middle and high MSG groups have an improved signal to noise ratio, and it makes the statistical

error smaller. The systematic uncertainty and signal extraction results is described in the next chapter.

Chapter 7

Systematic Uncertainties

In this chapter, the systematic uncertainties for the total flux between 4.5-20.0 MeV and for the energy spectrum shape are described. The systematic uncertainty for the day/night analysis is described in section 9.5.

7.1 Energy scale

The systematic uncertainty on the flux due to the energy scale is estimated taking into account the inaccuracy of the abolute energy scale (0.54%). In order to do this, the signal extraction was repeated with the energy scale shifted. Y_i^{scale+} and Y^{scale_i}, which are the obtained total flux after shifting the energy scale by $\pm 0.54\%$, are calculated by changing the reconstructed energy of each solar neutrino MC event. The Y_i is the expected fraction of signal event in the i-th energy bin which is defined in Sec.6.5. With this method the 0.54% energy scale uncertainty makes $\pm 1.2\%$ change in the total flux for 4.5-20.0 MeV and is taken as the uncertainty resulting from the energy scale.

7.2 Energy resolution

The systematic uncertainty due to energy resolution is obtained based on the difference of the energy resolution between data and MC, obtained from the LINAC calibration as shown in Fig.7.1. The difference of the energy scale ($\Delta\sigma(E_{res})$) is

$$\Delta\sigma(E_{res}) = \begin{cases} 2.53\%(E < 4.77MeV) \\ 1.0\%(E > 6.75MeV) \\ \text{interpolation}(4.77 \leq E \leq 6.75MeV) \end{cases} \tag{7.1}$$

To estimate the systematic uncertainty of the energy resolution, the predicted energy spectrum was distorted with a shifted energy resolution. The predicted spectrm($\mathcal{F}$) is calculated by

$$\mathcal{F}(E_{obs}) = \left\{ \int_0^{E_{max}} F(E_e) R(E_e, E_{obs}) dE_e \right\}, \tag{7.2}$$

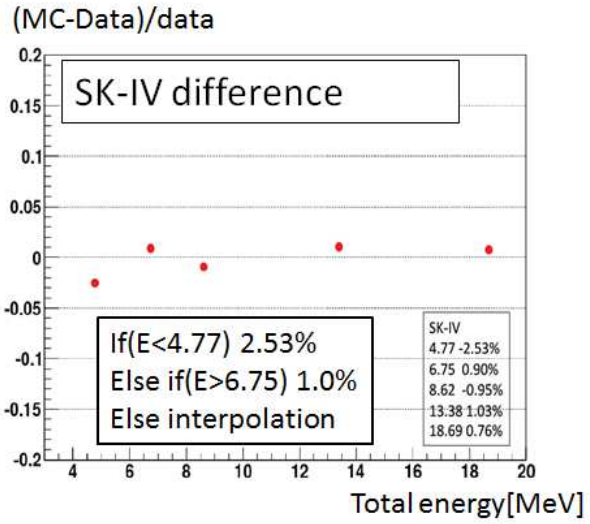

Figure 7.1: The difference of the energy resolution between data and MC for the LINAC calibration.

where E_e is the total energy of the recoli electron, F(E_e) is the recoil energy spectrum, calculated in equation 3.4, $R(E_e, E_{obs})$ is the detector response function, which takes into account energy resolution($\sigma(E_e)$) and is described as;

$$R(E_e, E_{obs}) = \frac{1}{\sqrt{2\pi\sigma(E_e)^2}} \exp\left(-\frac{(E_e - E_{obs})^2}{\sigma(E_e)^2}\right). \tag{7.3}$$

Fig.7.2 shows the energy distribution (top) and the energy resolution function (bottom) obtained by single electron MC. The black points show the standard deviation of the Gaussian fit, while the red line shows the fit result;

$$\sigma(E_e) = \frac{1}{E_e}(-0.123 + 0.376\sqrt{E_e} + 0.0349E_e). \tag{7.4}$$

To replace $\sigma(E_e)$ of equation 7.3 with $\sigma^+(E_e)$=$\sigma(E_e)(1 + \Delta\sigma(E_{res}))$ or $\sigma^-(E_e)$=$\sigma(E_e)(1 - \Delta\sigma(E_{res}))$, the $\mathcal{F}^+(E_{obs})$ or $\mathcal{F}^-(E_{obs})$ are obtained. Finally, the ratio of $\mathcal{F}^+(E_{obs})$ or $\mathcal{F}^-(E_{obs})$ to the original $\mathcal{F}$ is used as a weighting factor of Y_i, and hence the Y_i^{Eres+} or Y_i^{Eres-} is obtained. Using this method, the obtained flux uncertainty due to the energy resolution is estimated to be $\pm$ 0.15%.

7.3 ^{8}B spectrum

The uncertainty due to the ^{8}B spectrum shape is estimated in paper [25], which includes both experimental and theoretical uncertainties. To estimate this effect, the original spectrum $\phi(E_\nu)$ is deformed over the range of the spectrum shape uncertainty. Then $F^{^8B+(\text{or-})}$ is made with equation 3.4. By using $F^{^8B+(\text{or-})}$ in equation 7.3, $Y_i^{^8B+}$ and $Y_i^{^8B-}$ are obtained and the

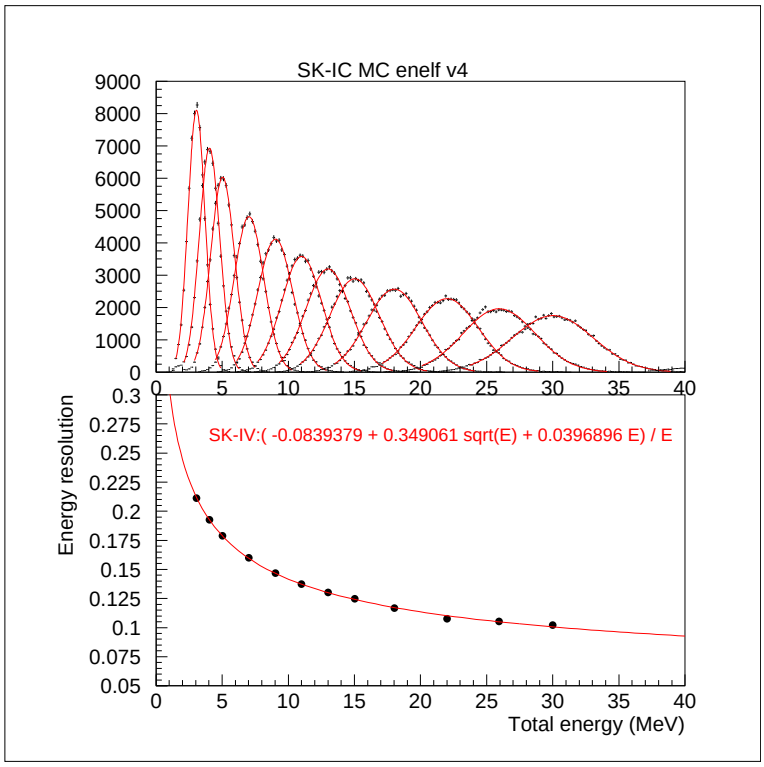

Figure 7.2: Top; Reconstruction energy distribution (black) of electron MC simulation with Gaussian fit (red). Bottom; Black point shows the obtained one standard deviation of the Gaussian fit with the fittng result by the polynominal function.

deviation from the original Y_i is taken. Thus the obtained flux uncertainty due to the ^{8}B spectrum shape is $\pm 0.35\%$.

7.4 Trigger efficiency

The trigger efficiency depends on the vertex position, water transparency, hit PMTs and so on. The systematic uncertainty of the trigger efficiency is estimated by comparing the nickel calibration data and MC simulation. For 4.0-4.5 and 4.5-5.0 MeV, the difference between data and MC is 4.5% and 0.37%, respectively. Above 5.0 MeV, trigger efficiency is 100%, so its uncertainty is negligible.

7.5 Reduction

7.5.1 Fiducial volume cut

The systematic uncertainty of the fiducial volume cut is estimated using the difference of the reconstructed vertex from the nickel calibration, between data and MC, which we call the 'vertex shift'. Fig.7.3 shows the vertex shift at each position for SK-IV (left) and SK-III (right). The origin of the arrow shows the nickel source position, while the direction indicates how the reconstructed vertex is shifted. The length of the arrow shows the magnitude of the vertex shift. The vertex shift for SK-IV is improved compared with that of SK-III. The reason is not fully understood, but the main contributions could be better linearity of the new front-end electronics and a more precise timing calibration.

To estimate the systematic uncertainty, the reconstructed vertex positions of solar neutrino MC events are artificially shifted, following the arrows in Fig.7.3, and the fraction of events which are rejected by the fiducial volume cut is estimated. Fig.7.4 shows the energy dependence of the fraction of rejected events. The energy dependence below 5.5 MeV comes from the tight fiducial volume cut, not by the energy dependence of vertex shift. The systematic uncertainty on the total flux is estimated to be $\pm 0.17\%$.

7.5.2 Gamma ray cut

The vertex shift and angular resolution difference between data and MC can cause a bias to the gamma ray cut efficiency. We shift the reconstructed vertex and direction artificially as shown in Fig.7.5, and estimate the fraction of events which are rejected by gamma ray cut. And the systematic uncertainty of the gamma ray cut is obtained. The systematic uncertainty on the total flux is estimated to be $\pm 0.2\%$.

7.5.3 $g_v^2 - g_a^2$ cut

The systematic uncertainty of the $g_v^2 - g_a^2$ cut is estimated using the difference of the $g_v^2 - g_a^2$ cut efficiency between LINAC data and the correponding MC, as shown in Fig.7.6. The $g_v^2 - g_a^2$ cut systematic uncerteinty on the total flux is estimated to be $\pm 0.3\%$.

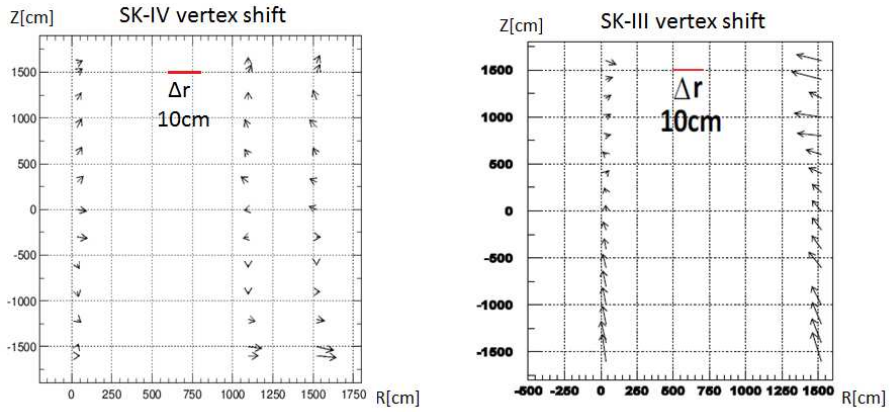

Figure 7.3: The vertex shift which is measured by the nickel calibration for SK-IV (left) and SK-III (right). The origin of the arrow shows the nickel source position and the direction indicates the average of the reconstructed position. The length of arrow shows the magnitude of the vertex shift.

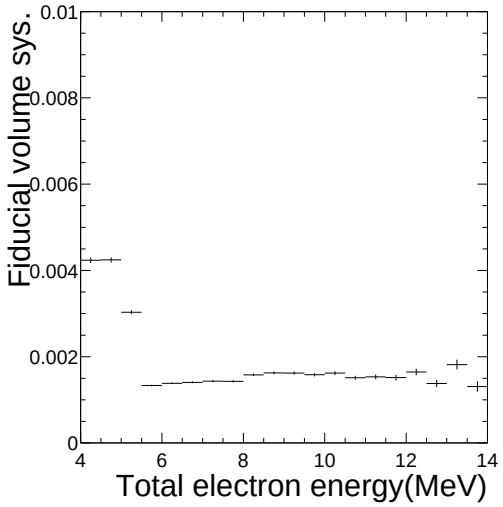

Figure 7.4: The energy dependence of the fraction of events which are rejected by (tight) fiducial volume cut, due to the vertex shift.

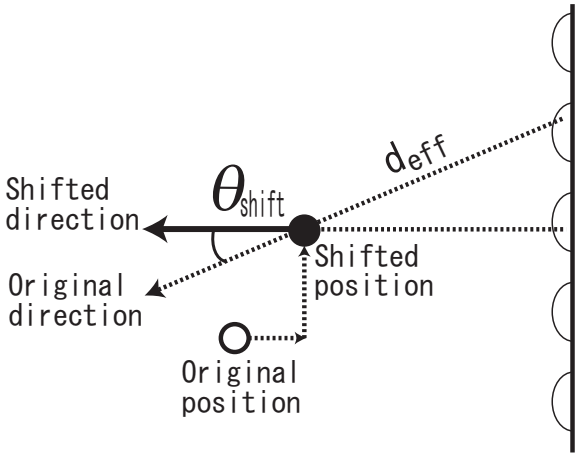

Figure 7.5: The method to artificially shift the reconstructed vertex and direction. The shifted direction is determined based on the original direction and reconstructed direction.

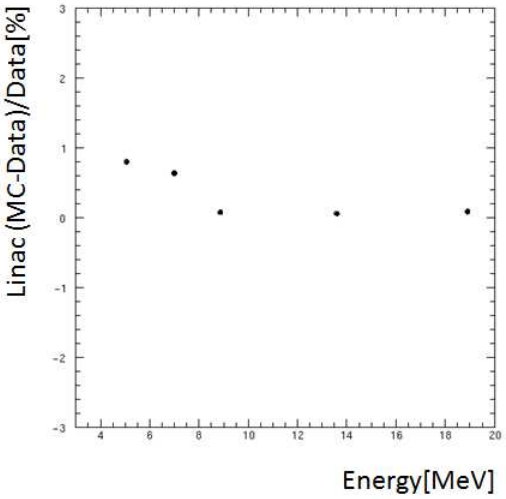

Figure 7.6: The difference of the $g_v^2 - g_a^2$ cut efficiency between data and MC obtained by the LINAC calibration.

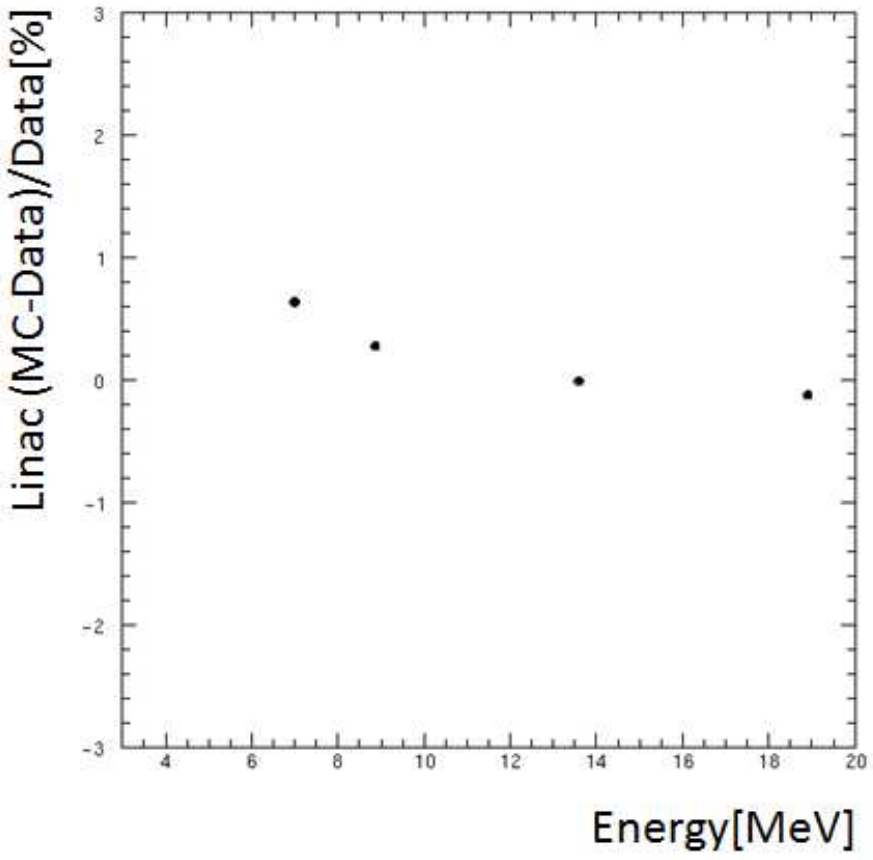

Figure 7.7: The difference of the hit pattern cut efficiency between data and MC for the LINAC calibration.

7.5.4 Hit pattern cut

The systematic uncertainty on the total flux by hit pattern cut is also estimated by the difference of the cut efficiency between LINAC data and the correspponding MC, as shown in Fig.7.7. The hit pattern cut systematic uncertainty on the total flux is estimated to be $\pm 0.3\%$.

7.5.5 Cluster hit event cut

The systematic uncertainty on the total flux by cluster hit event cut is estimated by the difference of its efficiency between DT data and the correponding MC. DT events taken at the region where the cluster hit event cut is enforced (6.12) are used. Fig.7.8 shows the obtained CLIK distribution of the DT data (black) and MC (red). The difference of the cluster hit event cut efficiency for 5.0-5.5 MeV, 4.5-5.0 MeV and 4.0-4.5 MeV is 0.44%, 0.64% and 1.1%, respectively. The systematic uncertainty on the total flux is estimated to be 0.3%.

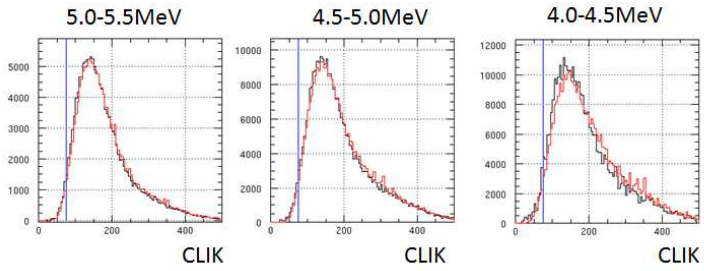

Figure 7.8: The difference of the CLIK cut efficiency between data and MC obtained by the DT for 5.0-5.5MeV(left), 4.5-5.0MeV(middle) and 4.0-4.5MeV(right).

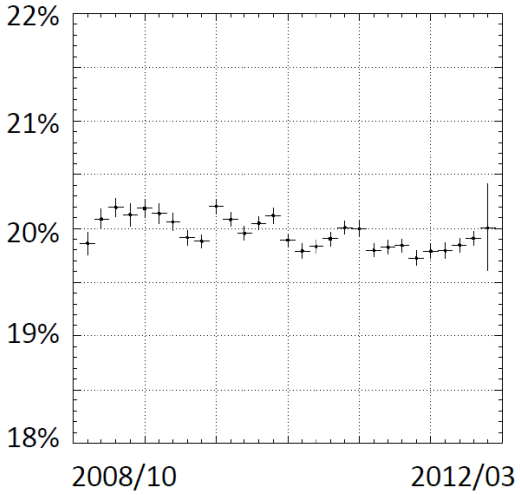

Figure 7.9: The time variation of the dead time of the spallation cut.

7.5.6 Spallation cut

The systematic uncertainty coming from the spallation cut is estimated by the difference in the dead time due to the spallation cut between data a random sample and MC, which takes into account the position dependence of the dead time function, and is shown in Fig.6.7. Fig.7.9 shows the time variation of the dead time. The spallation cut systematic uncertainty on the total flux is estimated to be 0.2%.

7.6 Angular resolution

The angular resolution is obtained using the LINAC. The angular resolution is defined as the angle which includes 68% of the reconstructed directions within the distribution from the LINAC beam direction. The systematic uncertainty of the angular resolution is obtained from the difference of the angular resolution between the LINAC data and the correponding MC, which is shown in Fig.7.10. The result is comparable to that for SK-III in the lower energy

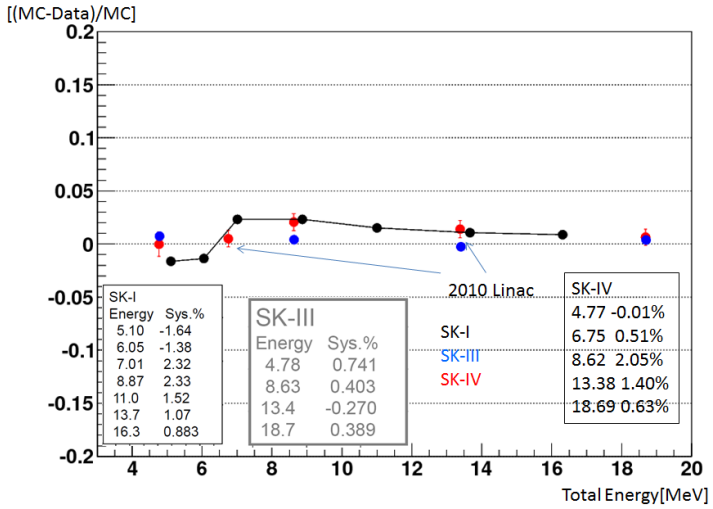

Figure 7.10: The difference of the angular resolution between data and MC from the LINAC calibration.

region, and slightly worse in the higher energy region, but the same level as that for SK-I.

In the SK-III solar neutrino analysis, the Y_i^{ang+} or Y_i^{ang-} was made by artificially shifting the reconstructed direction of the solar neutrino MC events. But this estimation method seems to over-estimate the uncertainty because the difference between Y_i^{ang+} or Y_i^{ang-} and Y_i includes the systematic uncertainty of the reduction steps, which is described in the last section. For SK-IV, the estimation of the expected shape of the solar neutrino signal, which takes into account the angular resolution systematic uncertainty(s_{ij}^{ang+} or s_{ij}^{ang-}), is used. This method is the same as that for SK-I. The systematic uncertainty on the total flux is estimated to be $\pm 0.36\%$.

7.7 Background shape

The systematic uncertainty of the background shape prediction is estimated as follows. As described in section 6.5, the solar angular distribution is fit with a non-flat background shape. To get the non-flat background shape, not only the distribution of the z-direction, but also the distribution of the phi direction is fit. To estimate the systematic uncertainty of the background shape, the background shape assuming a flat phi distribution, and taking into account only the zenith angle distribution, is made. The difference of the fit results from these two types of background shapes are taken as the systematic uncertainty on the total flux, which is 0.1%.

7.8 Signal extraction method

The systematic uncertainty coming from the signal extraction method is estimated by applying the signal extraction to dummy data, which have a known number of signal and background events. The systematic uncertainty of signal extraction method is estimated to be $\pm 0.7\%$.

Source	Flux(4.5-20.0MeV)	Reference
Energy scale	±1.2%	Sec.7.1
Energy resolution	±0.15%	Sec.7.2
^{8}B spec.	±0.33%	Sec.7.3[25]
trigger efficiency	±0.1%	Sec.7.4
Vertex shift	±0.17%	Sec.7.5.1
$g_v^2 - g_a^2$	±0.3%	Sec.7.5.3
Hit pattern cut	±0.3%	Sec.7.5.4
Spallation	±0.2%	Sec.7.5.6
Gamma-ray cut	±0.2%	Sec.7.5.2
Cluster hit cut	±0.3%	Sec.7.5.5
Ang. resolution	±0.36%	Sec.7.6
Background shape	±0.1%	Sec.7.7
Signal ext. method	±0.7%	Sec.7.8
Cross section	±0.5%	Sec.7.9[37]
Total	±1.7%	

Table 7.1: Summary of the systematic uncertainty on the total flux. The combined total systematic uncertainty is ±1.7%.

7.9 Cross section

The systematic uncertainty of the solar neutrino interaction cross section is estimated from the paper [37], in which the radiative corrections parameters for neutrino-electron scattering, ρ and κ, have 1σ theoretical uncertainties. The errors of ρ and κ are mainly due to the lack of precise knowledge of top quark and Higgs mass and QCD origin. The parameters are shifted by $\pm 1\sigma$ and the flux was obtained. The obtained systematic uncertainty on the total flux is ±0.5%.

7.10 Summary of systematic uncertainty

The systematic uncertainty of the total flux is summarized in Table 7.1. The combined systematic uncertainty is calculated as the quadratic sum of all components and found to be 1.7%. This is the best value compared with SK-I and III. The spectrum systematic uncertainty is described in the next section and the day/night systematic uncertainty is described in 9.5 .

7.11 Spectrum systematic uncertainty

The systematic uncertainty of the spectrum shape consists of two components, which are energy-correlated and energy-uncorrelated errors.

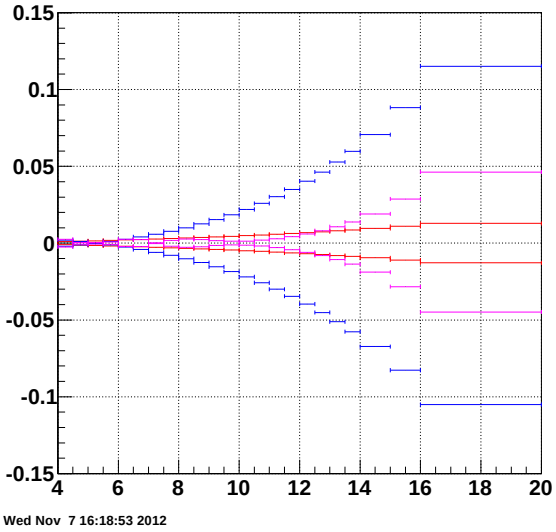

Figure 7.11: The energy-correlated systematic errors for each energy bin. The red, pink and blue distributions correspond to systematic errors of the ^{8}B spectrum shape, the energy resolution and the absolute energy scale, respectively.

7.11.1 Energy-correlated systematic uncertainty

The energy-correlated systematic uncertainty comes from the absolute energy scale, the energy resolution and the ^{8}B spectrum shape. This systematic uncertainty is estimated using equation 7.2, with individually artifically shifted energy scale, energy resolution and ^{8}B spectrum. The result is shown in Fig.7.11, with these values taken into account in the spectrum shape analysis and the oscillation analysis.

7.11.2 Energy-uncorrelated systematic uncertainty

Multiple scattering goodness

The systematic uncertainty of the signal extraction using MSG, below 7.5 MeV, is estimated using the MSG distribution from LINAC data and MC. Fig.7.12 shows an example of a MSG distribution of data (black points) and MC (blue), for the 4.8 MeV LINAC (top) and the ratio of the MC to the data for 4.8 MeV (red), 8.8 MeV (black) and 18.6 MeV (blue). This ratio is used as a scaling factor to bring the MC into better agreement with the data. After applying this ratio to the MC, the signal extraction is applied again. The difference in the number of solar neutrino events is taken as the systematic uncertainty. The systematic uncertainty of the MSG signal extraction is summarized in Table 7.2.

Summary of the energy-uncorrelated systematic error

The energy-uncorrelated energy spectrum uncertainties are summarized in Table 7.2. In this table, the common offset of the uncertainties is omitted in order to estimate the true effect on

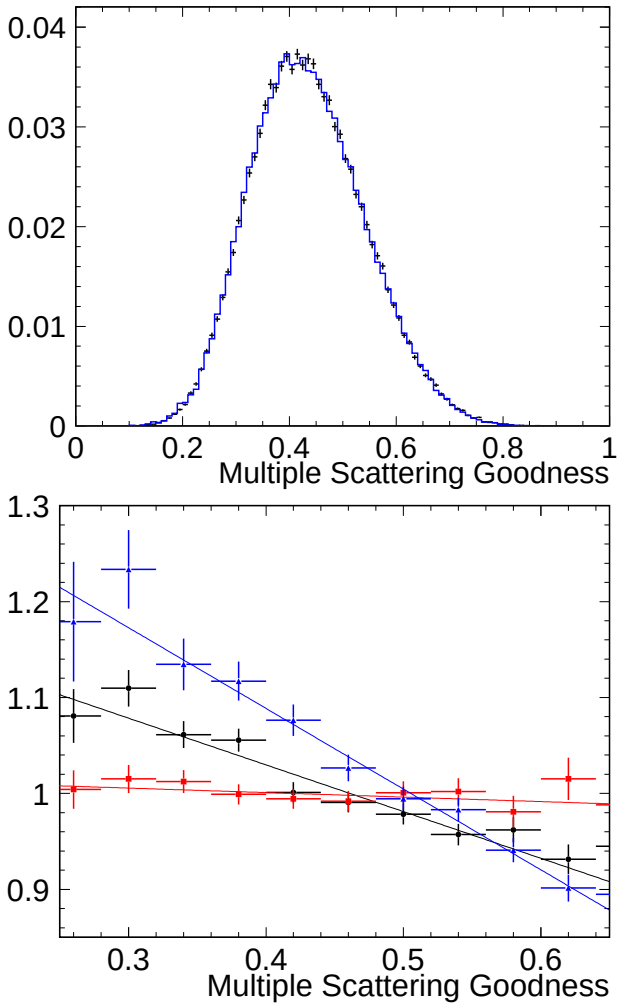

Figure 7.12: Top; MSG distributions of 4.8 MeV LINAC data (black points) and MC (red). Bottom; Ratio of the MC to the data for 4.8 MeV (red), 8.8 MeV (black) and 18.6 MeV (blue).

Energy (MeV)	4-4.5	4.5-5	5-5.5	5.5-6	6-6.5	6.5-7.5	7.5-8.5	8.5-20
Trig eff	±4.5%	±0.37%	-	-	-	-	-	-
$g_v^2 - g_a^2$	±0.8%	±0.8%	±0.8%	±0.8%	±0.64%	±0.64%	±0.1%	±0.1%
Hit pattern	-	-	-	-	-	±0.64%	±0.28%	±0.28%
Gamma Cut	±0.1%	±0.1%	±0.1%	±0.1%	±0.1%	±0.1%	±0.1%	±0.1%
Vertex shift	±0.5%	±0.5%	±0.3%	±0.17%	±0.17%	±0.17%	±0.17%	±0.17%
BG shape	±2.9%	±1.0%	±0.8%	±0.2%	±0.1%	±0.1%	±0.1%	±0.1%
Sig.Ext.	±2.1%	±2.1%	±2.1%	±0.7%	±0.7%	±0.7%	±0.7%	±0.7%
Cross section	±0.2%	±0.2%	±0.2%	±0.2%	±0.2%	±0.2%	±0.2%	±0.2%
MSG	±0.4%	±0.3%	±0.3%	±0.3%	±1.7%	±1.7%	±1.7%	-
Total	±6.0%	±2.6%	±2.5%	±1.2%	±2.0%	±2.1%	±1.9%	±0.8%

Table 7.2: Energy uncorrelated systematic uncertainty on the spectrum shape.

the energy spectrum shape.

Chapter 8

Results of the SK-IV solar analysis

In this chapter, the results of the solar neutrino analysis of SK-IV are described. The unit of energy in this chapter is kinetic energy. In order to explicity describe so, it is written as 'MeV(kin)'.

8.1 ^{8}B neutrino flux

Fig.8.1 shows the solar angle distribution of the SK-IV final sample, with a recoil electron kinetic energy range from 4.0 to 19.5 MeV(kin). The horizontal axis shows $\cos\theta_{sun}$, which is defined in Fig.6.20 and is divided into 80 bins. The vertical axis shows the event rate in units of [Event/day/kton/bin]. The best fit signal and background shapes are also shown in the solid and dash red lines, respectively. The total number of extracted solar neutrino signals is 19,811 $^{+220}_{-218}$(stat.) $\pm$337(syst.).

By comparing with the total number of expected solar neutrino signals obtained from the solar neutrino MC, the observed ^{8}B solar neutrino flux is calculated.

First, the expected number of solar neutrino interactions in SK is calculated as

$$\int_0^{E_\nu^{\max}} \phi(E_\nu)\sigma_{total}(E_\nu)N_e T_{live} dE_\nu, \tag{8.1}$$

where E_ν is the incident neutrino energy, $\phi(E_\nu)$ is the solar neutrino flux of ^8B neutrinos for E_ν, $\sigma_{total}(E_\nu)$ is the total scattering cross section, N_e is the total number of target electrons in the ID detector (1.086×10^{34} electrons) and T_{live} is the livetime in units of seconds. For the ^8B neutrino spectrum, the calculated spectrum based on the alpha spectrum measurement by Winter et al. [25] is used. Using a total flux of 5.25 [$\times10^6/cm^2$/s], which is the central value of the flux measured by the SNO NC analisys [7], the calculated event rate from equation (8.1) is 3.4×10^{-3} events/second, for ^8B neutrinos.

Second, the solar neutrino MC is generated. The position is set uniformly and the energy and direction of the recoil electrons are determined by equations (3.4) and (3.6), respectively. To reduce the statistical error of the calculation, the generated event rate of the Monte Carlo simulation is 100 per minute, for the full operation time. The generated MC events are processed through the same analysis procedure described in section 6.3, and the expected number of events for the assumed flux ($5.25\times10^6/cm^2$/s) is found.

Finally, the observed ^{8}B solar neutrino flux is found to be

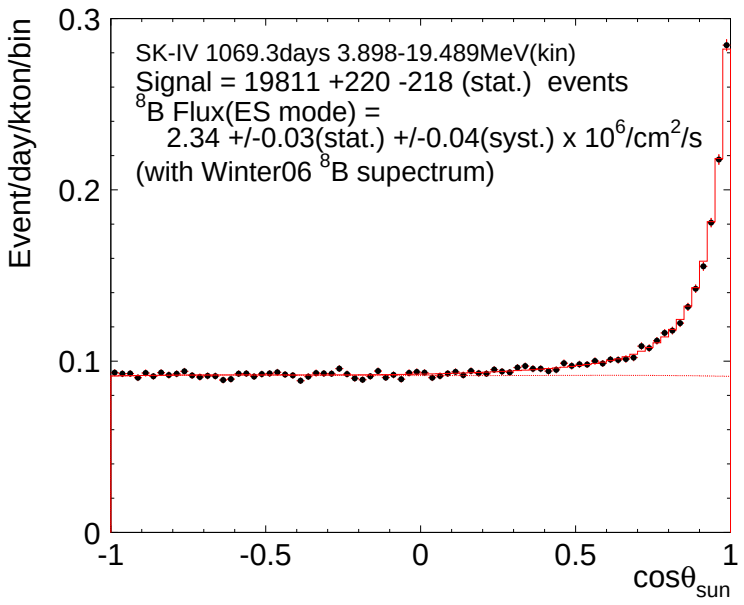

Figure 8.1: The solar angle distribution of 4.0-19.5 MeV(kin) events. The black point show the data. The solid and dashed red lines show the fit signal and background shapes, respectively.

$$2.34 \pm 0.03(\text{stat.}) \pm 0.04(\pm syst.) \times 10^6 \text{cm}^{-2}\text{sec}^{-1}. \tag{8.2}$$

8.2 Day/Night flux asymmetry

The day and night times are defined as

$$cos\theta_z \leq 0 \qquad \text{Day livetime=506.5 days} \tag{8.3}$$
$$cos\theta_z > 0 \qquad \text{Night livetime=562.8 days} \tag{8.4}$$

θ_z is the solar zenith angle, which is defined in Fig.6.20. Fig.8.2 shows the angular distribution of the day and night times. The observed fluxes are

$$\begin{aligned} \Phi_{day} &= 2.27 \pm 0.04(stat.) \pm 0.05(sys.) \times 10^6 \text{cm}^{-2}\text{sec}^{-1} \\ \Phi_{nignt} &= 2.39 \pm 0.04(stat.) \pm 0.05(sys.) \times 10^6 \text{cm}^{-2}\text{sec}^{-1}. \end{aligned} \tag{8.5}$$

The straight day/night flux asymmetry A_{DN}(straight) is defined as

$$\begin{aligned} A_{DN}(\text{straight}) &= \frac{\Phi_{day} - \Phi_{night}}{\frac{1}{2}(\Phi_{day} + \Phi_{night})} \\ &= -0.052 \pm 0.023(stat.) \pm 0.014(sys). \end{aligned} \tag{8.6}$$

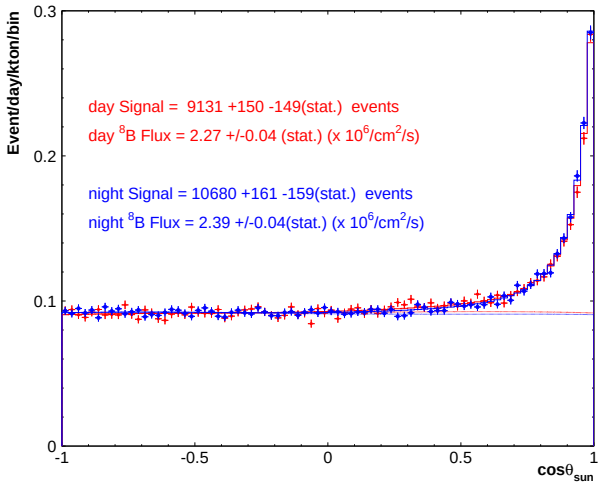

Figure 8.2: The solar zenith angle distribution for the day time and the night time.

Fig.8.3 shows the summary of fluxes for each cos_z value, which is divided into 10 bins. For each given oscillation parameter, the time variation during the night time can be predicted. So, using such a constraint, the day/night asymmetry can be more precisely measured. Details of such a day/night asymmetry is described in section 9.5.

8.3 Energy spectrum

The spectrum of recoil electrons is measured in the same method as the measurement of the total flux. In the case of the spectrum measurement, the final sample of solar neutrino candidates is divided according to the reconstructed electron kinetic energy, and then the flux is calculated using the extended maximum likelihood method described in section 6.5. As described in section 6.6, the final sample below 7.5 MeV(kin) is divided into three MSG groups and are taken into account in the flux calculation. Fig.8.4 shows the solar zenith angle distribution for the three MSG groups. For each MSG group and energy bin, the signal extraction was done with a given $b_{ij}(E_{kin}$,MSG) and $s_{ij}(E_{kin}$,MSG), which are probability density functions of the background and solar neutrino signal, respectively. Table 8.1 shows the observed and expected rates in each energy bin with units of [event/kton/year]. The error value of the observed rate is a statistical error only. Fig.8.5 shows the statistical error differences between the original signal extraction and the signal extraction by taking into account MSG groups. The statistical error can be reduced by about 10% at maximum. Fig.8.6 shows the event rate of both solar neutrino MC (red) and observed solar neutrino events, for each energy bin, and Fig.8.7 shows the energy spectrum of SK-IV. The vertical axis is [(observed rate)/(expected rate) with the expect rate=$5.25\times10^6 cm^{-2}s^{-1}$]. The obtained spectrum, normalized by the expectation, is consistent with a flat shape. More detailed analysis of the energy spectrum combining other SK phases is discussed in section 9.4.2

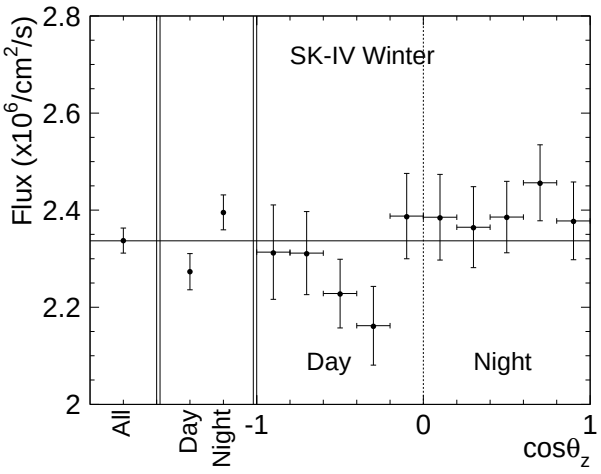

Figure 8.3: The solar zenith angle dependence of the solar neutrino flux. The error bars show only statistical errors.

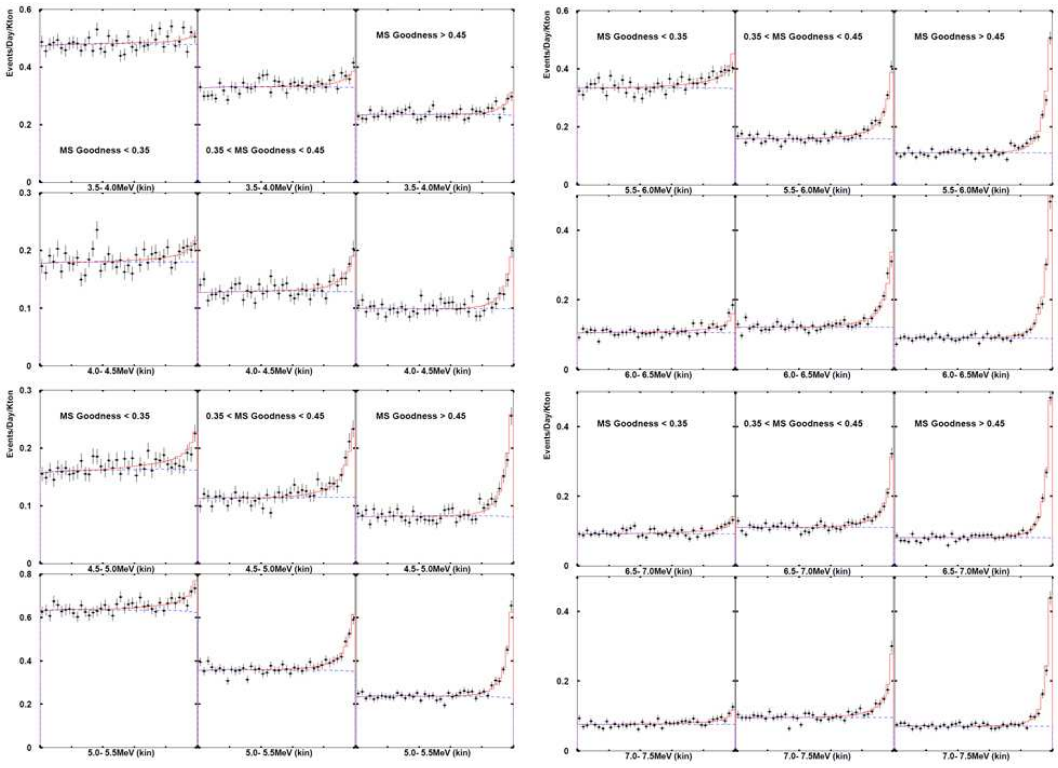

Figure 8.4: The solar zenith angle distribution for each MSG groups for 3.5-5.5 MeV(kin).

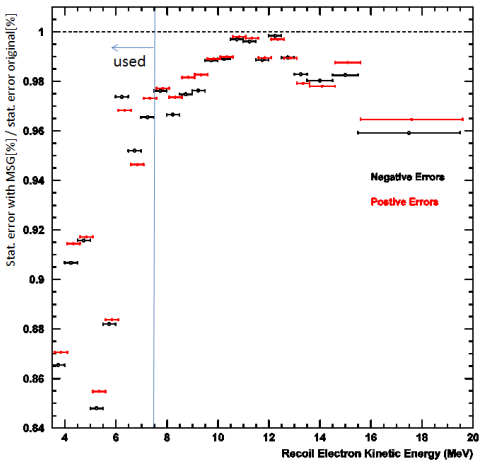

Figure 8.5: Ratio of the statistical errors of the method taking into account the MSG groups and the original (i.e. w/o MSG) methods. The red and black points are for the positive and negative errors, respectively.

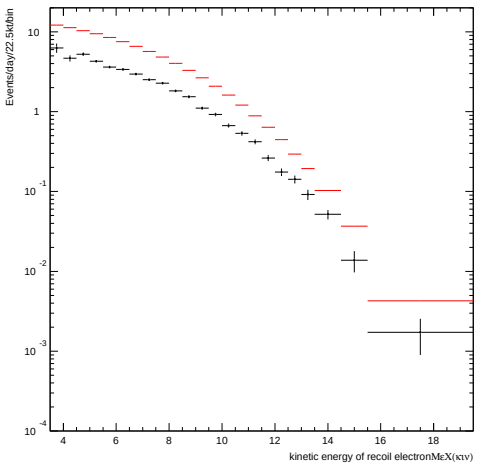

Figure 8.6: The event rate of the solar neutrino MC (red) and observed solar neutrino events. The reduction efficiencies are corrected.

Energy (MeV(kin))	Observed rate ALL $-1 \leq \cos\theta_z \leq 1$	DAY $-1 \leq \cos\theta_z \leq 0$	NIGHT $0 < \cos\theta_z \leq 1$	Expected rate ^{8}B	hep
$3.5 - 4.0$	$102.1^{+13.6}_{-13.3}$	$103.0^{+21.1}_{-20.4}$	$101.4^{+18.0}_{-17.4}$	196.7	0.345
$4.0 - 4.5$	$75.7^{+6.5}_{-6.3}$	$66.3^{+9.9}_{-9.4}$	$83.1^{+8.8}_{-8.4}$	183.0	0.336
$4.5 - 5.0$	$85.2^{+4.3}_{-4.2}$	$87.5^{+6.5}_{-6.3}$	$83.3^{+5.8}_{-5.6}$	167.7	0.325
$5.0 - 5.5$	$69.7^{+2.6}_{-2.6}$	$64.0^{+3.8}_{-3.7}$	$74.7^{+3.6}_{-3.5}$	153.2	0.314
$5.5 - 6.0$	$58.9^{+2.0}_{-1.9}$	$56.1^{+2.9}_{-2.8}$	$61.5^{+2.8}_{-2.7}$	138.0	0.303
$6.0 - 6.5$	$55.0^{+1.9}_{-1.8}$	$50.5^{+2.6}_{-2.5}$	$59.1^{+2.6}_{-2.5}$	122.0	0.287
$6.5 - 7.0$	$48.1^{+1.7}_{-1.6}$	$46.4^{+2.4}_{-2.3}$	$49.6^{+2.3}_{-2.2}$	106.7	0.272
$7.0 - 7.5$	$40.8^{+1.5}_{-1.5}$	$40.5^{+2.2}_{-2.1}$	$41.2^{+2.1}_{-2.0}$	92.2	0.256
$7.5 - 8.0$	$37.0^{+1.4}_{-1.3}$	$37.9^{+2.0}_{-1.9}$	$36.2^{+1.9}_{-1.8}$	78.0	0.238
$8.0 - 8.5$	$29.5^{+1.2}_{-1.1}$	$29.6^{+1.7}_{-1.6}$	$29.4^{+1.6}_{-1.6}$	65.0	0.220
$8.5 - 9.0$	$24.9^{+1.0}_{-1.0}$	$25.4^{+1.5}_{-1.5}$	$24.5^{+1.4}_{-1.3}$	53.4	0.204
$9.0 - 9.5$	$18.0^{+0.9}_{-0.8}$	$17.6^{+1.2}_{-1.2}$	$18.3^{+1.2}_{-1.1}$	42.8	0.185
$9.5 - 10.0$	$15.0^{+0.8}_{-0.7}$	$15.7^{+1.1}_{-1.1}$	$14.3^{+1.0}_{-1.0}$	33.7	0.167
$10.0 - 10.5$	$10.9^{+0.6}_{-0.6}$	$10.6^{+0.9}_{-0.8}$	$11.1^{+0.9}_{-0.8}$	26.0	0.150
$10.5 - 11.0$	$8.70^{+0.55}_{-0.52}$	$7.52^{+0.77}_{-0.70}$	$9.79^{+0.81}_{-0.75}$	19.54	0.133
$11.0 - 11.5$	$6.82^{+0.47}_{-0.44}$	$6.40^{+0.68}_{-0.61}$	$7.21^{+0.68}_{-0.62}$	14.30	0.117
$11.5 - 12.0$	$4.27^{+0.37}_{-0.34}$	$3.39^{+0.49}_{-0.43}$	$5.13^{+0.56}_{-0.50}$	10.19	0.102
$12.0 - 12.5$	$2.84^{+0.30}_{-0.27}$	$2.90^{+0.44}_{-0.37}$	$2.78^{+0.44}_{-0.38}$	7.08	0.087
$12.5 - 13.0$	$2.31^{+0.27}_{-0.24}$	$2.59^{+0.41}_{-0.35}$	$2.03^{+0.37}_{-0.31}$	4.75	0.074
$13.0 - 13.5$	$1.49^{+0.22}_{-0.19}$	$1.42^{+0.32}_{-0.26}$	$1.55^{+0.32}_{-0.26}$	3.10	0.062
$13.5 - 14.5$	$1.68^{+0.23}_{-0.20}$	$1.79^{+0.35}_{-0.29}$	$1.55^{+0.31}_{-0.25}$	3.19	0.092
$14.5 - 15.5$	$0.447^{+0.133}_{-0.101}$	$0.439^{+0.191}_{-0.128}$	$0.457^{+0.206}_{-0.141}$	1.117	0.059
$15.5 - 19.5$	$0.224^{+0.108}_{-0.073}$	$0.296^{+0.176}_{-0.109}$	$0.148^{+0.146}_{-0.074}$	0.460	0.068

Table 8.1: The observed and expected event rates in each energy bin at 1 AU. The errors are statistical errors only. The reduction efficiencies are corrected and the expected event rates are for a flux of $5.25\times10^6/cm^2/$s.

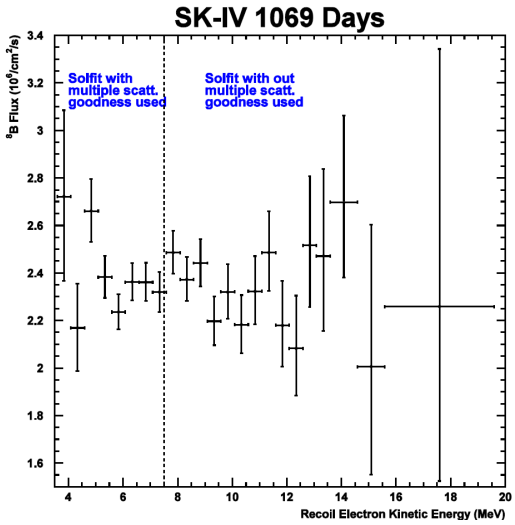

Figure 8.7: The energy spectrum of SK-IV. Below 7.5 MeV(kin), signal extraction with MSG is used.

Chapter 9

SK-I,II,III,IV Combined Analysis

9.1 ^{8}B neutrino total flux

The total flux values of ^{8}B neutrinos obtained from SK-I [6], II [35], III [36] and IV are as follows;

$$\begin{aligned}
2.38 \pm 0.02(\text{stat.}) \pm 0.08(\text{sys.}) \times 10^6 cm^{-2}s^{-1} &\quad \text{SK-I(4.5-19.5MeV(kin))} \\
2.41 \pm 0.05(\text{stat.})^{+0.16}_{-0.15}(\text{sys.}) \times 10^6 cm^{-2}s^{-1} &\quad \text{SK-II(6.5-19.5MeV(kin))} \\
2.40 \pm 0.04(\text{stat.}) \pm 0.05(\text{sys.}) \times 10^6 cm^{-2}s^{-1} &\quad \text{SK-III(4.5-19.5MeV(kin))} \\
2.34 \pm 0.03(\text{stat.}) \pm 0.04(\text{sys.}) \times 10^6 cm^{-2}s^{-1} &\quad \text{SK-IV(4.0-19.5MeV(kin))}.
\end{aligned}$$

For the SK-III flux calculation, the energy dependence in the ν-e differential cross section (equation 3.2) was accidentally eliminated in our previous report [36]. This problem was fixed in this thesis.

The ^{8}B flux in each SK phase is summarized in Fig.9.1. The vertical axis is in units of [(SK-rate)/MC(unoscillated)], where MC(unoscillated) corresponds to $5.25\times10^6 cm^{-2}s^{-1}$. The statistical average flux from the SK-I, II, III, IV results is 0.451±0.007, and the χ^2 to this average value is 0.58/3D.O.F. So, the fluxes of all SK phases are consistent.

The combined solar zenith angle distribution is shown in Fig.9.2. The total number of observed solar neutrino signals is counted to be about 57,700 events during the SK-I, II, III, IV total livetime of 3904 days. The day/night asymmetry analysis and the oscillation analysis, which are described in the next sections, can be accomplished with such a large number of solar neutrino events.

9.2 Energy spectrum

The energy spectra for all phases, with systematic uncertainties, are shown in Fig.9.3. As described in 6.6, the flux measurement with MSG is used below 7.5 MeV(kin) for the SK-III and SK-IV spectrum. The trigger efficiency of the 3.5-4.0 MeV(kin) energy bin in the SK-IV phase is about 86%. By the SK experiment rule, the energy bin in which obtained trigger efficiency was below 90% should not be used, so we did not use this energy bin in the oscillation analysis.

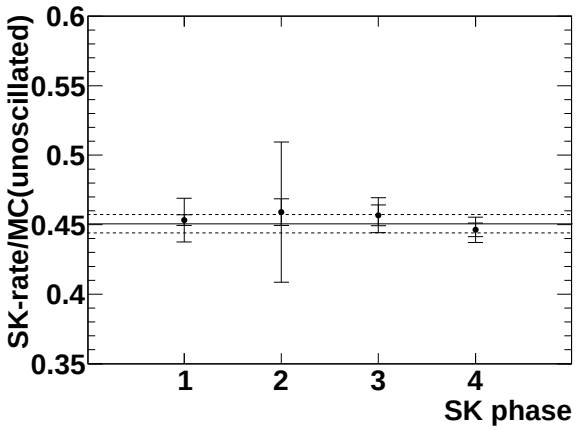

Figure 9.1: The ^{8}B flux in each SK phase. The vertical axis is in units of ([SK-rate)/MC(unoscillated)], where MC(unoscillated) corresponds to $5.25\times10^6 cm^{-2}s^{-1}$. The solid line shows the statistical averaged flux of SK-I, II, III, IV and the dashed line shows the 1σ error from the average.

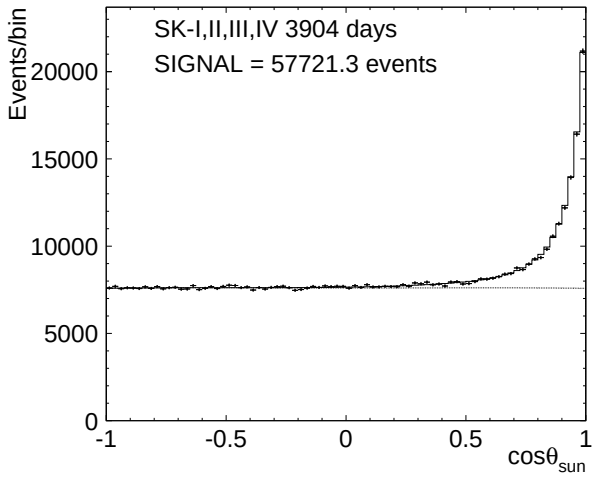

Figure 9.2: The combined solar zenigh angle distribution from SK-I, II, III, IV with livetime of 3904 days.

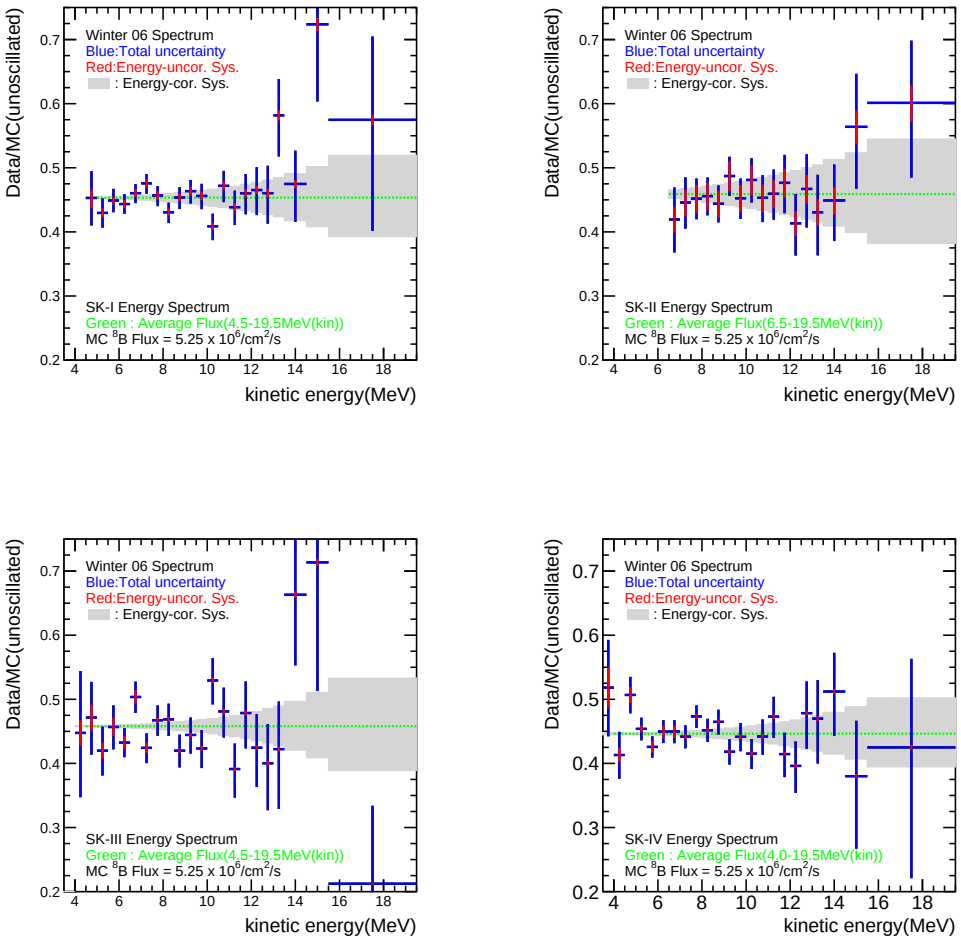

Figure 9.3: The energy spectrum for each phase, with systematic uncertainty.

9.3 Oscillation analysis method

9.3.1 Neutrino oscillation predictions

The predicted energy spectrum which takes into account neutrino oscillations is calculated as follows. As described in section 2.4, the oscillation parameter $\sin^2(\theta_{13})$ is fixed to 0.0242, with a three flavor oscillation analysis used in this analysis.

In the following, two flavor oscillation method is described for simplicity. The survival probability of the electron neutrino(p_e) is predicted by three steps.

1. From the production point of the solar neutrino to the surface of the Sun.
2. From the surface of the Sun to the surface of the Earth.
3. From the surface of the Earth to the detector.

In practice, since the distance between the Sun and Earth is much larger than the vacuum oscillation length of the favored parameter $\Delta m^2/\mathrm{E} \sim 10^{-9} eV^2/\mathrm{MeV}$, the propagation of ν_1 and ν_2 at step 2 can be assumed to be incoherent. In this case, the net electron survival probability p_e can be described by the following equation, using p_i (ν_e which is produced in the core to appear as ν_i, where i is the mass eigenstate) and p_{ie} (ν_i at the surface of the earth to appear as ν_e at the detector).

$$p_e = p_1 \times p_{1e} + p_2 \times p_{2e} = 2p_1 p_{1e} + 1 - p_1 - p_{1e} \tag{9.1}$$

For the solar portion (step1), the production point distribution is calculated using the standard solar model. The value of p_1 is obtained by averaging over the production points. For the Earth portion (step3), p_{1e} is obtained as a function of neutrino energy and zenith angle of the sun ($\cos\Theta_z$). For various oscillation parrameter sets, Δm^2_{21}, θ_{12}, and $p_e(\Delta m^2_{21}, \theta_{21}, E_\nu, cos\Theta_z)$ are obtained.

Second, from the survival probability obtained by equation (9.1), the predicted neutrino interaction rate, with neutrino oscillations, for the i-th energy bin($E_{low,i}$ <E< $E_{high,i}$), can be written as

$$r_i = \int_{E_{low,i}}^{E_{high,i}} dE \int_{E_\nu} dE_\nu \phi(E_\nu) \int_{E_e} dE_e R(E_e, E) \left(p_e \frac{d\sigma_{\nu_e}}{dE_e} + (1-p_e) \frac{d\sigma_{\nu_\mu,\nu_\tau}}{dE_e} \right), \tag{9.2}$$

where $R(E_e, E)$ is the energy resolution function, which is defined in equation(7.3), $\frac{d\sigma_{\nu_e}}{dE_e}$ and $\frac{d\sigma_{\nu_\mu,\nu_\tau}}{dE_e}$ is the difference in cross section of the elastic scattering for ν_e and $\nu_{\mu,\tau}$ of energy E_ν, with a recoil electron energy E_e (shown in Fig.3.2), and $\phi(E_\nu)$ is the solar neutrino flux as a function of neutrino energy, which is shown in Fig.3.3 for ^{8}B neutrinos.

In this oscillation analysis, the zenith angle ($cos\theta_z$) of the nighttime (0< $cos\theta_z$≤1) is divided into 1000 bins and 1 bin during the daytime (-1< $cos\theta_z$≤0). This binning is defined as the cz bin (cz=1∼1001 bin). With this binning, the predicted observed event rate of ^{8}B and hep neutrinos for the i-th energy bin are described as

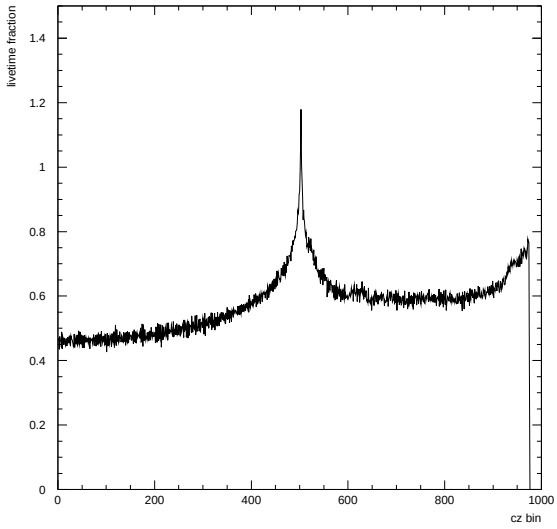

Figure 9.4: The livetime fraction in bin cz from 1 to 1000. cz bin = 1 and 1000 corresponds to $\cos\Theta_z = 0$ and 1, respectively.

$$
\begin{aligned}
B_i^{osc} &= \sum_{cz=1}^{1001} \frac{\tau(cz)}{\tau_{tot}} \cdot r_i^{\,^8B}(cz) \\
H_i^{osc} &= \sum_{cz=1}^{1001} \frac{\tau(cz)}{\tau_{tot}} \cdot r_i^{hep}(cz),
\end{aligned}
\tag{9.3}
$$

where $\tau(cz)$ is the livetime of the cz bin, which is obtained from the run profile of the real data and shown in Fig.9.4 (only for night part, corresponding cz bin from 1st to 1000th bin), and τ_{tot} is the total livetime.

9.3.2 Spectrum shape fitting

The comparison between the observed and predicted spectra is done by fitting their energy spectra in a χ^2 analysis. The χ^2 value is calculated for each SK phase individually, because each SK phase has unique energy correlated and uncorrelated errors, as shown in Fig.9.3.

A simple χ^2 caluclation is given by

$$
\chi^2_{simple} = \sum_{i=1}^{N_{bin}} \frac{(d_i - \beta b_i - \eta h_i)^2}{\sigma^2_{i,stat}},
\tag{9.4}
$$

where N_{bin} is defined in section 6.5 and is the number of energy bins (21st bin for SK-I, 17th bin for SK-II and 22nd bin for SK-III,IV). d_i is the data spectrum term, with statistical error of

$\sigma_{i,stat}$ and β and η are free parameters to allow for the arbitrary fit of the total neutrino fluxes. The d_i, b_i and h_i in equation 9.4 are as follows;

$$d_i = \frac{D_i}{B_i + H_i} \tag{9.5}$$

$$b_i = \frac{B_i^{osc}}{B_i + H_i} \tag{9.6}$$

$$h_i = \frac{H_i^{osc}}{B_i + H_i}, \tag{9.7}$$

where B_i and H_i are the predicted rates in case of no neutrino oscillations, which are shown in Table 8.1. So, d_i is the observed energy sepctrum, which is shown in Fig.9.3, and B_i^{osc} and H_i^{osc} are the predicted rates, which take into account neutrino oscillations and are calculated in equation (9.3).

Systematic uncertainty treatment

The χ^2 value described in equation (9.4) takes into account only statistical errors. In this subsection, the treatment of the systematic uncertainty, both energy correlated and uncorrelated are described.

The definition of the χ^2 which takes into account the systematic uncertainties is written as

$$\chi^2 = \sum_{i=1}^{Nbin} \frac{(d_i - (\beta b_i + \eta h_i) \times f(E_i, \delta_B, \delta_S, \delta_R))^2}{\sigma_i^2} + \delta_B^2 + \delta_S^2 + \delta_R^2. \tag{9.8}$$

The energy correlated systematic uncertainties consist of uncertainties on the absolute energy scale, the energy resolution and the ^{8}B spectrum, which are shown in Fig.7.11. Since these uncertainties directly impact the shape of the SK energy sepctrum, the χ^2 must reflect these possible changes. The energy correlated systematic uncertainties are applied to the spectrum as multiplicative energy shape factors (f), in order to reflect an actual one sigma shift. However, since the data may better agree with a lesser or greater shift from the one sigma assigned value, the factors are varied until the χ^2 gives a minimum value.

The combined energy shape factor is defined as below;

$$f(E_i, \delta_B, \delta_S, \delta_R) = f_B(E_i, \delta_B) \times f_S(E_i, \delta_S) \times f_R(E_i, \delta_R), \tag{9.9}$$

where B, S and R denote the ^{8}B spectrum shape, the absolute energy scale and the energy resolution, respectively. The energy shape factors ($f_x(E_i.\delta_x)$) are written as

$$f_x(E_i, \delta_x) = \frac{1}{1 + \delta_x \times \epsilon_x^{\pm}(E_i)}, \qquad (x = B, S, R), \tag{9.10}$$

where $\epsilon_x^{\pm}$ is the 1σ energy correlated uncertainty and $\delta_x^{\pm}$ is the unit-less parameter which scales $\epsilon_x^{\pm}$. δ_x is varied until the χ^2 gives the minimum value for a given β_m and η_m.

The σ_i in equation (9.8) is an uncertainty which combines the statistical and energy uncorrelated systematic uncertainty by quadrature with these errors. To take into account the energy uncorrelated systematic uncertainty on the total flux , a Taylor expansion to the second order

around the minimum β_m and η_m is used. The χ^2 using the Taylor expansion terms can be written as

$$\chi^2(\beta,\eta) = \chi^2_m(\beta_m,\eta_m) + \begin{pmatrix} \beta-\beta_m \\ \eta-\eta_m \end{pmatrix}^T C_0 \begin{pmatrix} \beta-\beta_m \\ \eta-\eta_m \end{pmatrix} \tag{9.11}$$

where C_0 is the curvature matrix which is defined as

$$C_0 = \sum_{i=1}^{N_{bin}} \begin{pmatrix} \frac{b_i^2}{\sigma_i^2} & \frac{b_i h_i}{\sigma_i^2} \\ \frac{b_i h_i}{\sigma_i^2} & \frac{h_i^2}{\sigma_i^2} \end{pmatrix}. \tag{9.12}$$

The C_0 is inversely proportional to the uncertainties of the fitting parameters β and η. Therefore it is possible to scale the curvature matrix by α_{sys} to allow the addition of the total energy uncorrelated systematic uncertainty to the total flux scale factors. The α_{sys} is defined as

$$\alpha_{sys} = \frac{\sigma_0^2}{\sigma_0^2+\sigma_{sys}^2}, \qquad \text{where} \qquad \sigma_0^2 = \sum_{i=2}^{N_{bin}} \frac{1}{\sigma_{stat,i}^2}, \tag{9.13}$$

and so, χ^2_α can be wriiten as

$$\chi^2_\alpha(\beta,\eta) = \chi^2_m(\beta_m,\eta_m) + \begin{pmatrix} \beta-\beta_m \\ \eta-\eta_m \end{pmatrix}^T \alpha_{sys}\cdot C_0 \begin{pmatrix} \beta-\beta_m \\ \eta-\eta_m \end{pmatrix}. \tag{9.14}$$

Finally, the χ^2 for the energy spectrum shape is expressed as

$$\chi^2_{spec}(\beta,\eta) = \mathrm{Min}(\chi^2_\alpha(\beta,\eta,\delta_B,\delta_S,\delta_R) + \delta_B^2 + \delta_S^2 + \delta_R^2), \tag{9.15}$$

with the number of fitting parameters at five; β, η, δ_B, δ_S and δ_R.

9.3.3 Time variation fitting

The time variation analysis is a different approach from the spectrum fit analysis, as it can take into account the earth matter effects.

The likelihood function that was used for extracting the solar signal (equation (6.15)) was modified using a scaling function which reflects the deviation from the average number of events, arising from time variations. Using a suitable substitution for the zenith angle, to take into account its time dependence, the oscillation rate prediction of earth (step3 in section 9.3.1) can be used to form the ratio $r_i(cz)/r_i^{ave}$, where r_i is a predicted solar zenith angle time variation for a given cz bin and energy bin i, which is obtained from equation (9.2), where r_i^{ave} is the averaged variation of r_i. The calculated time variation (r_i) for Δm^2_{21}=4.84$\times$ 10^{-5}eV^2 and $\sin^2\theta_{12}$=0.314 is shown in Fig.9.5.

The modified likelihood function can be written as follows.

$$\mathcal{L}_{t.v.} = e^{-(\sum_i B_i + S)} \prod_{i=1}^{N_{bin}} \prod_{j=1}^{n_i} (B_i\cdot b_{ij} + S\cdot Y_i \cdot s_{ij}\cdot r_i(cz)/r_i^{ave}). \tag{9.16}$$

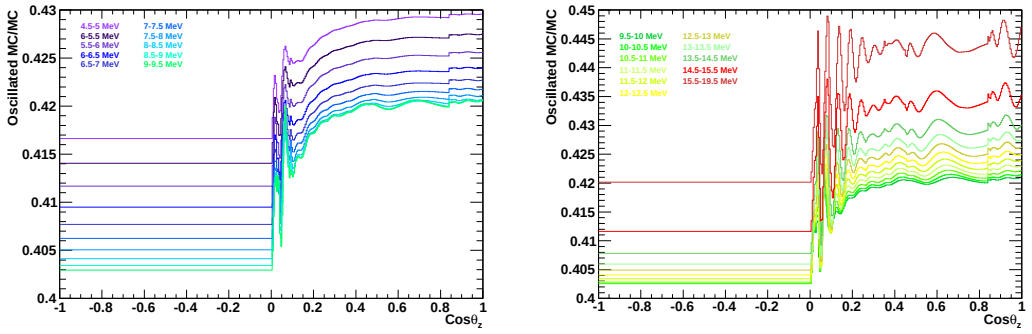

Figure 9.5: The predicted solar zenith angle time variation assuming a typical LMA solution, Δm^2_{21}=4.84$\times$ 10^{-5}eV^2 and $\sin^2\theta_{12}$=0.314.

If we set $r_i(cz)/r_i^{ave}$=1, this likelihood funciton becomes the original one. The effect of the earth matter oscillations can be tested by comparing the modified likelihood ($\mathcal{L}_{t.v}$) with the original likelihood. $\Delta\chi^2_{t.v.}$ is obtained from the calculation of

$$\Delta\chi^2_{t.v.} = -2(\log\mathcal{L} - \log\mathcal{L}_{t.v.}). \tag{9.17}$$

Then, the full SK χ^2 becomes

$$\chi^2_{SK} = \chi^2_{spec} + \chi^2_{t.v.}. \tag{9.18}$$

9.3.4 Flux constrained fitting

In the spectrum shape method, the ^{8}B and hep rate factors β and η are free to take any value, in order to minimize the difference between data and MC oscillated predictions. For the rate constrained fit, the rate factors β and η are constrained to the total rate of all active flavors of neutrinos on Earth. For the results presented later, we adopted the NC flux measurement by SNO.

In the flux constrained fitting the terms $(\beta-1)^2/\sigma_{\phi_{^8B}}$ and $(\eta-1)^2/\sigma_{\phi_{hep}}$ are added to the χ^2 of equation (9.18). $\sigma_{\phi_{^8B}}$=0.04 and $\sigma_{\phi_{hep}}$=2.0 correspond to the SNO NC ^{8}B flux uncertainty and the hep flux limit(ϕ_{hep} <2.9SSM) [7].

9.4 Oscillation analysis results

9.4.1 Oscillation parameter constraints from SK

The results of the two χ^2 fitting methods, the spectrum shape fitting (equation 9.15) and time variation fitting (equation 9.17), are described. After minimizing the free parameters described above, the χ^2 value is calculated for each oscillation parameter set, i.e. $\sin^2\theta_{12}$ and Δm^2_{21}. A χ^2 map is obtained on the plane of these oscillation parameters, and the minimum χ^2 point is found. From the minimum χ^2 point, allowed/excluded regions were obtained using a standard $\Delta\chi^2$ method. The minimum χ^2 point is obtained at

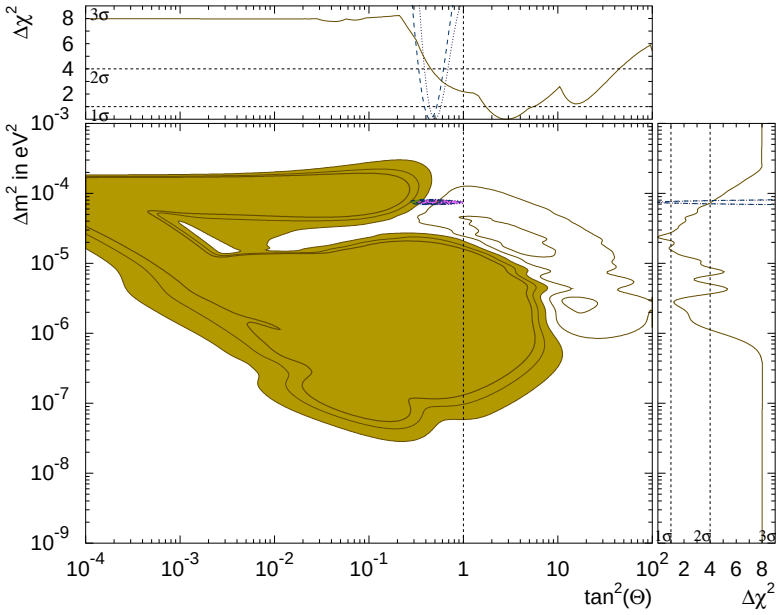

Figure 9.6: The excluded region from the SK combined analysis with KamLAND 3σ allowed region(purple). The χ^2 contours are shown for 1σ steps. The brown region corresponds to the 3σ excluded region.

$$sin^2(\theta_{12}), SK = 0.339^{+0.028}_{-0.024} \quad (9.19)$$

$$\Delta m^2_{21}, SK = 4.69^{+1.80}_{-0.83} \times 10^{-5} eV^2. \quad (9.20)$$

Fig.9.6 shows the obtaned SK-I,II,III,IV combined excluded/allowed regions by the spectrum shape fitting and the time variation fitting methods. SK data now excludes SMA and solution above the 5σ level and LOW solution above the 4.5σ level. Fig.9.7 shows the SK flux constrained allowed regions (green), showing the LMA region from KamLAND (blue) and the SK and KamLAND combined result (purple). The best fit parameters obtained by the SK combined fit with the flux constrained are

$$sin^2(\theta_{12}),\text{SK} = 0.322^{+0.024}_{-0.020} \quad (9.21)$$

$$\Delta m^2_{21},\text{SK} = 7.49^{+0.2}_{-0.20} \times 10^{-5} eV^2. \quad (9.22)$$

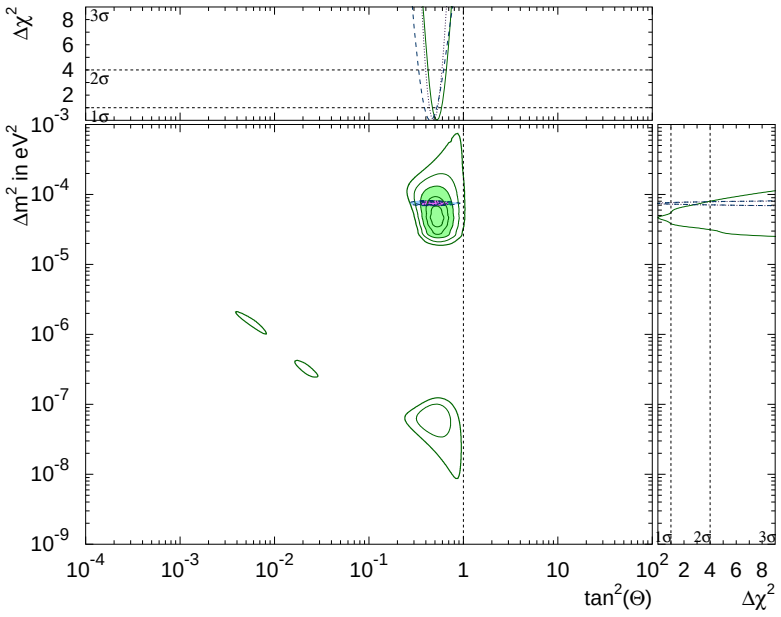

Figure 9.7: The allowed region from SK combined analysis with the flux constrained. The χ^2 contours are plotted from the 1σ to 5σ levels. The green painted region corresponds to the 3σ allowed region, the blue painted region corresponds to the KamLAND 3σ allowed region and the purple painted region corresponds to the all SK+KamLAND 3σ allowed regions.

oscillation par's	χ^2(d.o.f=81)	$\Phi_{^8B}$ [/cm^2/s]	Φ_{hep} [/cm^2/s]
LMA MSW osc. prediction1	79.02	$5.34{\cdot}10^6$	$17.4{\cdot}10^3$
LMA MSW osc. prediction2	76.54	$5.47{\cdot}10^6$	$16.0{\cdot}10^3$
flat probability	75.29	$5.25{\cdot}10^6$	$14.7{\cdot}10^3$
flat probability, dσ ratio	75.23	$5.53{\cdot}10^6$	$14.4{\cdot}10^3$

Table 9.1: The comparison of χ^2 value, best fit ^{8}B neutrino flux and best fit hep neutrino flux for each prediction of given oscillation parameters.

9.4.2 Results of the energy spectrum fit

Fig.9.8 shows the observed energy spectrum and the predicted energy spectrum distortions under four different assumptions. In the spectrum shape fitting, we calculated the χ^2 value for each SK phase, and then added the χ^2's of all of them to give a final combined χ^2. This plot shows the SK combined energy spectrum for descriptive purposes, because it is not statistically correct to add spectra which have different systematic errors, and so this plot itself is not used in the oscillation analysis.

The assumptions of the predicted energy spectrum are as follows;

1. LMA MSW oscillation prediction1 (blue):
   Oscillation parameters are $\sin^2\theta_{12}$=0.304 and Δm^2_{21}=7.44$\times 10^{-5} eV^2$, and MSW effect is taken into account.

2. LMA MSW oscillation prediction2 (green):
   Oscillation parameters are $\sin^2\theta_{12}$=0.310 and Δm^2_{21}=4.86$\times 10^{-5} eV^2$, and MSW effect is taken into account.

3. Flat probability (black):
   Assuming that the unoscillated ^{8}B spectrum is decreased by a factor independent of energy. In the spectrum analysis, the 'flat' corresponds to the case that neutrino oscillation is assumed as energy independent. To obtain the flat probability shape, the p_e in the equation(9.1) is set to constant value, and calculate the χ^2 value. The best fit factor from the SK energy spectrum is obtained by p_e=0.317. But because of the different shape of the differential cross section between ν_e and $\nu_{\mu,\tau}$ ($d\sigma_{\nu_e}/dE_e$ vs. $d\sigma_{\nu_{\mu,\tau}}/dE_e$), the energy spectrum is slightly distorted.

4. Flat probability, dσ ratio (purple);
   Assuming that $d\sigma_{\nu_{\mu,\tau}}/dE_e$ has the same energy dependence as $d\sigma_{\nu_e}/dE_e$.

The χ^2 values and the best fit ^{8}B and hep flux ($\Phi_{^8B}$, Φ_{hep}) for each assumption are summurized in Table 9.1. The fourth assumption, 'the flat probability, dσ ratio', gives the minimum χ^2 among them, and is favored over the MSW oscillation assumptions by 1.1-1.9σ.

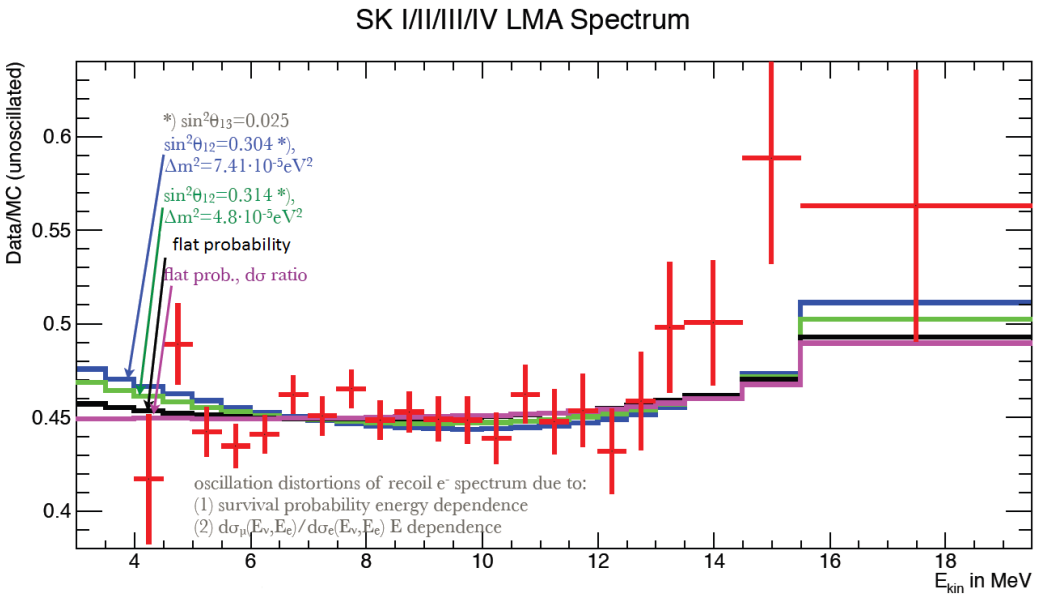

Figure 9.8: The SK combined energy spectrum (red point are statistical errors only) with the predicted distorted shape of $sin^2\theta$=0.304 and Δm^2=7.44×10$^{-5}eV^2$ (blue), $sin^2\theta$=0.310 and Δm^2=4.86×10$^{-5}eV^2$ (green) and flat shapes (best quadratic fit (black) and flat prob of dσ ratio (purple)).

9.5 Day/Night asymmetry analysis

Due to the matter effect from the Earth, the observed solar neutrio flux is affected while the sun is below the horizon. This effect is called 'the day/night effect' and it increases the ν_e flavor content as shown in Fig.9.5.

To evaluate the day/night effect, two methods are used, one is called the straight day/night flux asymmetry, defined in equation (8.7)and the other uses a day/night amplitude fitting method described later. In this subsection, these two methods are explained and the results are described.

9.5.1 Straight day/night asymmetry

A straight day/night asymmetry method separately measures the flux during the day(ϕ_{day}) and night(ϕ_{night}) times and forms the day/night asymmetry A_{DN}. The definitions of ϕ_{day} ,ϕ_{night} and A_{DN} were described in section 8.2

The values of A_{DN} for SK-I,II,III and IV were found to be

$$
\begin{aligned}
-2.1 \pm 2.0(\text{stat.}) \pm 1.3(\text{sys.})[\%] \quad & \text{SK-I(4.5-19.5MeV(kin))} \\
-6.3 \pm 4.2(\text{stat.}) \pm 3.7(\text{sys.})[\%] \quad & \text{SK-II(6.5-19.5MeV(kin))} \\
-5.6 \pm 3.1(\text{stat.}) \pm 1.3(\text{sys.})[\%] \quad & \text{SK-III(4.5-19.5MeV(kin))} \\
-5.2 \pm 2.3(\text{stat.}) \pm 1.4(\text{sys.})[\%] \quad & \text{SK-IV(4.0-19.5MeV(kin))}.
\end{aligned}
$$

The negative sign on each value corresponds to the fact that the night flux is larger than day flux. Taking just the statistically weighted average of those values,

$$A_{DN}, \text{SK combined} = -4.0 \pm 1.3(stat.)[\%] \tag{9.23}$$

is obtained. Only the combined statistical uncertainty is quoted here, because a more sophisticated method is necessary to combine the systematic uncertainties. The method is described in the next subsection.

9.5.2 Day/night amplitude fit

Day/night amplitude fit method

The day/night amplitude fit method [38] is a more sophisticated method which employs a maximum likelihood fit to the amplitude of the time variation, constrained by the predicted manner of the variation. A modified likelihood function from the original signal extraction (6.15) is defined as follows:

$$\mathcal{L} = e^{-(\sum_i B_i + S)} \prod_{i=1}^{N_{bin}} \prod_{j=1}^{n_i} (B_i \cdot b_{ij} + S \cdot Y_i \cdot s_{ij} \cdot z_i(\alpha, t)), \tag{9.24}$$

where $z_i(\alpha, t)$ is a new signal factor which includes any time variable parameters, such as solar zenith angle (day/night effect).

To take into account the time variation of the solar zenith angle, the predicted solar zenith angle variation rate of the i-th energy bin ($r_i(cz)$), which is shown in Fig.9.5, is used. From the $r_i(cz)$ distribution and livetime distribution ($l(cz)$), which is shown in Fig.9.4, the livetime averaged total rate(r_i^{av}), day rate(r_i^{day}), night rate(r_i^{night}) and predicted day/night asymmetry (A_i) of the i-th energy bin are calculated as follows;

$$\begin{aligned} r_i^{day} = \int_{day} r_i(cz) \cdot l(cz) d(cz) \quad , \qquad r_i^{night} &= \int_{night} r_i(cz) \cdot l(cz) d(cz) \\ r_i^{ave} &= \int_{all} r_i(cz) \cdot l(cz) d(cz) \\ A_i &= \frac{r_i^{day} - r_i^{night}}{1/2(r_i^{day} + r_i^{night})}. \end{aligned} \tag{9.25}$$

From the day livetime (L_D) and the night livetime (L_N), the livetime asymmetry (L_{DN}) and the effective asymmetry parameter (a_i) are also calculated. The L_{DN} and a_i are defined as follows;

$$L_{DN} = \frac{L_D - L_N}{1/2(L_D + L_N)} \tag{9.26}$$

$$a_i = \frac{1}{2} A_i \times \frac{1}{2} L_{DN}. \tag{9.27}$$

Then, the $z_i(\alpha, t)$ which was introduced in equation (9.24) is defined as

$$z_i(\alpha, t) = \frac{1 + \alpha((1 + a_i) r_i(t)/r_i^{av} - 1)}{1 + \alpha a_i}, \tag{9.28}$$

where α is a free parameter which is called the day/night scaling factor. The signal (S), the backgrounds (B_i) and the α which give the maximum likelihood is computed and for the resulting α and σ_α, which is a statistical uncertainty of the α value, the day/night asymmetry is calculated by

$$A_{DN} = A_i \times \alpha \pm A_i \times \sigma_\alpha(stat.). \tag{9.29}$$

This day/night amplitude method fit depends on the assumed shape of $r_i(t)$, and the predicted day/night asymmetry value A_i also depends on the oscillation parameters ($sin^2\theta$, Δm^2). For this day/night amplitude method, events which have energy above 4.5 MeV(kin) for SK-I,III and IV and above 6.5 MeV(kin) for SK-II were used.

Systematic uncertainty

Almost all the systematic uncertainties which were described in chapter 7 can be canceled for the day/night asymmetry analysis because the difference between such short time scales is discussed. However, there still remain some systematic uncertainties for the day/night analysis, especially coming from direction dependence of the signal and background.

- Direction dependence of the energy scale:

  The direction dependence of the energy scale may cause a systematic shift in the day/night asymmetry. To quantify the direction dependence of the energy scale, DT data and the corresponding MC were compared. For this purpose, a polynomial fit to the detector zenith angle dependence of the energy scale was made. To translate this function to a direction dependence of the energy scale systematic uncertainties, solar neutrino MC event energies were scaled based on this function. Fig.9.9 shows a fit result of the direction dependence of the energy scale for solar neutrino events for SK-IV, which varies by 0.3% from downward to upward going events. The fitted function was then applied to all events while running the unbinned amplitude fit, and the 0.08% change in the day/night asymmetry taken as the systematic uncertainty for SK-IV. The systematic uncertainty method was done for each SK phase, and obtained to be 0.8% for SK-I and II and 0.2% for SK-III. The systematic uncertainty for SK-III and IV is lower than that for SK-I and II because of the introduction of the position dependence of the water transparency to the MC, which was described in detail in section 5.4.

- Background shape:

  The systematic uncertainty from the background shape should be considered. The method of the estimation is similar to that for the flux uncertainty which is described in section 7.7, comparing the day/night amplitude factor between the corresponding two background shapes and the difference taken as the systematic uncertainty. The total SK-IV uncertainty is estimated as 0.6%, and is the largest contribution to the day/night systematic uncertainty.

- Gamma ray cut:

  Because of the tight fiducial volume cut used for 4.5-5.0 MeV(kin) and the poswall dependence of the lower energy gamma ray cut (equation (6.10)) for SK-III and SK-IV, there is a contribution to the systematic uncertainty from the gamma ray cut. Following the method

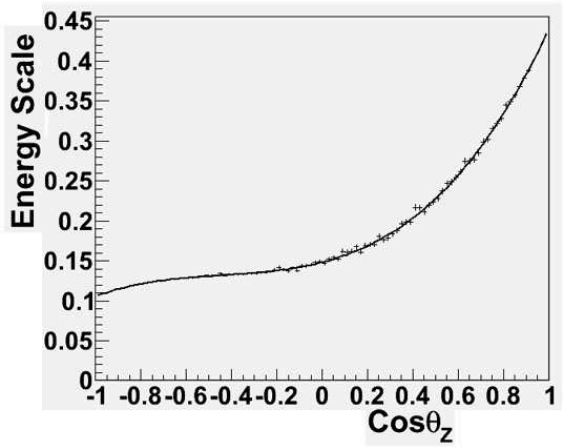

Figure 9.9: The zenith angle dependence of the energy scale for SK-IV.

	SK-I	SK-II	SK-III	SK-IV
energy scale	±0.8%	±0.8%	±0.2%	±0.08%
background shape	±0.6%	±0.6%	±0.6%	±0.6%
gamma ray cut	-	-	±0.2%	±0.1%
Total	±1.0%	±1.0%	±0.7%	±0.7%

Table 9.2: Systematic uncertainties for the day/night asymmetry.

of estimation of systematic uncertainty described in chapter 7, the estimated systematic uncertainty is ±0.1% for SK-IV and ±0.2% for SK-III.

The total systematic uncertainties for each SK phase are summarized in Table 9.2

Day/night amplitude fit results

As described above, when we obtain the day/night scaling factor(α) and the day/night asymmetry(A_{DN}, which is defined in equation 9.29), the predicted solar zenith angle time variation (r_i) is used. Because r_i has dependence on oscillation parameters, the day/night asymmetry also has oscillation parameters dependence. By assuming $sin^2(\theta_{12}) = 0.339$ and $\Delta m^2_{21} = 4.69 \times 10^{-5} eV^2$, the day/night asymmetries resulting from the day/night amplitude fit for each SK phase are obtained as follows;

$$
\begin{aligned}
&-2.0 \pm 1.7(\text{stat.}) \pm 1.0(\text{sys.})[\%] && \text{SK-I(4.5-19.5MeV(kin))} \\
&-4.3 \pm 3.8(\text{stat.}) \pm 1.0(\text{sys.})[\%] && \text{SK-II(6.5-19.5MeV(kin))} \\
&-4.3 \pm 2.7(\text{stat.}) \pm 0.7(\text{sys.})[\%] && \text{SK-III(4.5-19.5MeV(kin))} \\
&-2.8 \pm 1.9(\text{stat.}) \pm 0.7(\text{sys.})[\%] && \text{SK-IV(4.5-19.5MeV(kin))},
\end{aligned}
$$

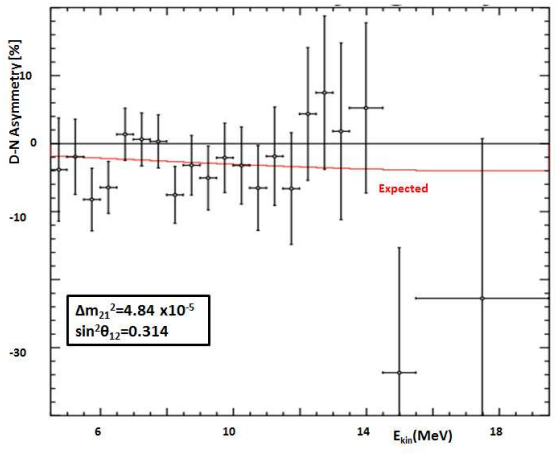

Figure 9.10: Energy dependence of the fit day/night asymmetry for Δm^2=4.84·$10^{-5}eV^2$ and $\sin^2(\theta_{12})$=0.314. The red line shows the expected energy dependence of the day/night asymmetry.

and the SK combined day/night amplitude is obtained as

$$A_{DN}, \text{SK combined} = -2.8 \pm 1.1(stat.) \pm 0.5(syst.)[\%]. \tag{9.30}$$

Fig.9.10 shows the energy dependence of the day/night asymmetry along with the predicted day/night asymmetries (A_i, red line). The error bar shows only the statistical uncertainty. Fig.9.11 shows the Δm^2_{21} dependence of the predicted and observed day/night asymmetry for $\sin^2(\theta_{12})$ fixed to 0.314. The allowed Δm^2_{21} range of the solar experiments (green band) and KamLAND (purple band) are overlaid. Fig.9.12 shows the $sin^2(\theta_{12})$ dependence of the day/night asymmetry when Δm^2_{21} is fixed to 4.69×$10^{-5}eV^2$. The day/night asymmetry is sensitive to Δm^2_{12}, but gives no information about $\sin^2(\theta_{12})$.

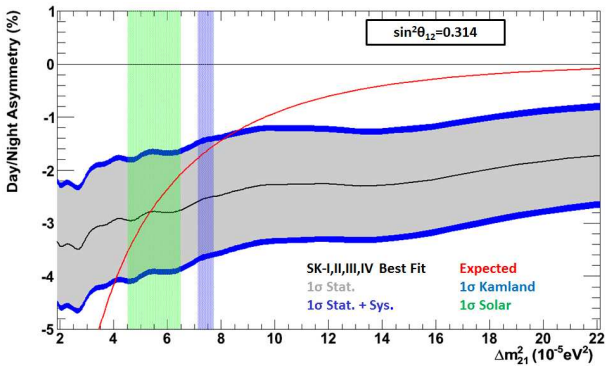

Figure 9.11: Dependence of the day/night asymmetry on Δm^2 for $sin^2(\theta_{12})$=0.314. The light gray band shows the statistical error and the blue band shows the statistical + systematic error. The red line shows the expected day night asymmetry and the green and purple bands show the 1σ allowed region for the solar experiments and the KamLAND Δm^2,respectively.

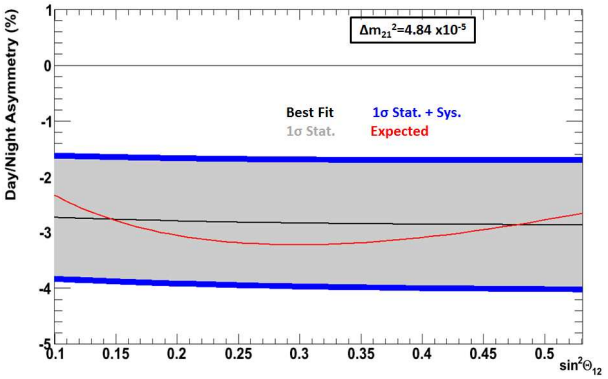

Figure 9.12: Dependence of the day/night asymmetry on $sin^2(\theta_{12})$ for Δm^2=4.88·10$^{-5}eV^2$. The light gray band shows the statistical error and the blue band shows the statistical + systematic error. The red line shows the expected day night asymmetry.

Chapter 10

Discussion

In this chapter, the results of the neutrino oscillation parameters(θ_{12}, Δm^2_{21}) obtained by SK are compared with that of other experiments. Also, combined results with them are also presented.

10.1 Comparison/Combine with SNO result

The SNO collaboration fit the neutrino signal based on an average $\Phi_{^8B}$ for the day and night time, a ν_e survival probability as a function of neutrino energy(E_ν), during the day($P_{ee}^{day}(E_\nu)$) and the night($P_{ee}^{night}(E_\nu)$), and a day/night asymmetry survival probability($A_{ee}(E_\nu)$), which is defined by

$$A_{ee}(E_\nu) = 2\frac{P_{ee}^{night}(E_\nu) - P_{ee}^{day}(E_\nu)}{P_{ee}^{night}(E_\nu) + P_{ee}^{day}(E_\nu)}. \tag{10.1}$$

The $P_{ee}^{day}(E_\nu)$ and $A_{ee}(E_\nu)$ are parameterized by

$$P_{ee}^{day}(E_\nu) = c_0 + c_1(E_\nu[\mathrm{MeV}] - 10) + c_2(E_\nu[\mathrm{MeV}] - 10)^2 \tag{10.2}$$

$$A_{ee}(E_\nu) = a_0 + a_1(E_\nu[\mathrm{MeV}] - 10), \tag{10.3}$$

where c_0, c_1 and c_2 are parameters defining the ν_e survival probability and a_0 and a_1 are parameters defining the relative difference between the night and day ν_e survival probability [7].

For the combined fit to all SNO phases (I, II, III) using the maximum likelihood technique, each obtained parameters are summarized in Table 10.1.

Fig.10.1 shows the $P_{ee}^{day}(E_\nu)$ and $A_{ee}(E_\nu)$ with RMS spread, taking into account the parameter uncertainties and correlations between each parameter. The red band represents the result from the maximum likelihood fit, and the blue band shows the cross check from the Bayesian fit.

Then a χ^2 was defined to compare between the oscillation parameters from the predicted neutrino oscillation hypothesis and the SNO observations, and contours of oscillation parameters were obtained and seen in Fig.10.2. Comparing Fig.10.2 and Fig.9.7, the results of SK and SNO are consistent with each other. The SK and SNO results are then combined by adding their

	Best fit	+Stat	-Stat	+Syst	-Syst
$\Phi_{^8B}[\times 10^6/\mathrm{cm}^2/\mathrm{s}]$	5.25	0.16	0.16	0.11	0.13
c_0	0.317	0.016	0.016	0.009	0.009
c_1	0.0039	0.0065	0.0067	0.0045	0.0045
c_2	-0.0010	0.0029	0.0029	0.0014	0.0016
a_0	0.046	0.031	0.031	0.014	0.013
a_1	-0.016	0.025	0.025	0.010	0.011

Table 10.1: results from the maximum likelihood fit

χ^2's. At this time, the total flux of ^{8}B flux is a common parameter. Fig.10.3 shows the obtained combined contours of SK-I,II,III,IV and SNO-I,II,III. The best fit oscillation parameters are

$$sin^2(\theta_{12})\text{,SK,SNO} = 0.317^{+0.014}_{-0.016} \quad (10.4)$$

$$\Delta m^2_{21}\text{,SK,SNO} = 4.85^{+1.44}_{-0.54} \times 10^{-5} eV^2. \quad (10.5)$$

The contour of KamLAND is also shown in the figure. There is a slight tension in the Δm^2_{21} between KamLAND and the SK/SNO combined result.

10.2 Combined with other solar neutrino experiments

The results from the Chlorine experiment (Homestake), Gallium experiments (SAGE, Gallex/GNO) and Borexino (only ^{7}Be neutrino flux) are added to the χ^2 of the SK and SNO combined oscillation analysis. The χ^2 values of those experiments are based on two equivalent ways of defining the χ^2 function [39] which is described by

$$\chi^2_{rate} = \sum_{n,m=1}^{N(=3)} (R^{expt}_n - R^{theor}_n)[\sigma^2_{nm}]^{-1}(R^{expt}_m - R^{theor}_m), \quad (10.6)$$

where N is the number of experiments, in this case N=3 (Cl, Ga, Borexino experiment). The σ^2_{nm} is a matrix of squared uncertainties which are sums of the correlated and uncorrelated uncertainties among experiments, R^{expt} is the observed rate and R^{theor} is the SSM predicted event rate. Fig.10.4 shows the contour plot of all solar combined allowed regions (green at 3σ allowed region) and with KamLAND (blue at 3σ allowed region). The best fit values and 1σ values of SK, SNO, radiochemical and Borexino combined analysis are

$$sin^2(\theta_{12})\text{,all solar} = 0.310^{+0.014}_{-0.015} \quad (10.7)$$

$$\Delta m^2_{21}\text{,all solar} = 4.86^{+1.44}_{-0.52} \times 10^{-5} eV^2 \quad (10.8)$$

Finally, combining the results of all solar neutrino experiments and the KamLAND reactor neutrinos,

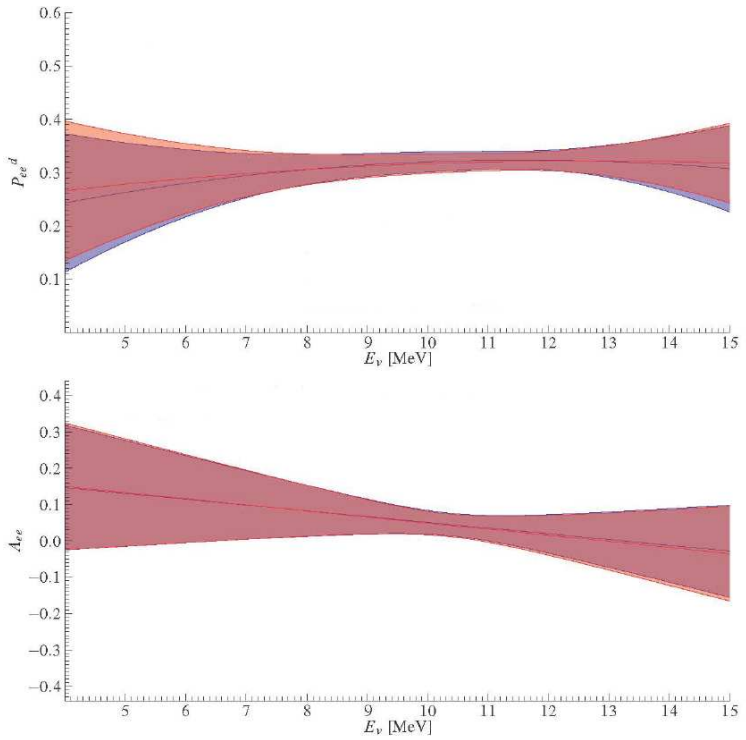

Figure 10.1: The observed $P_{ee}^{day}(E_\nu)$ (top) and $A_{ee}(E_\nu)$ (bottom) with the RMS spread in the SNO combined result. The red band represents the results from the maximum likelihood fit and the blue band represents the cross check by the Bayesian fit.

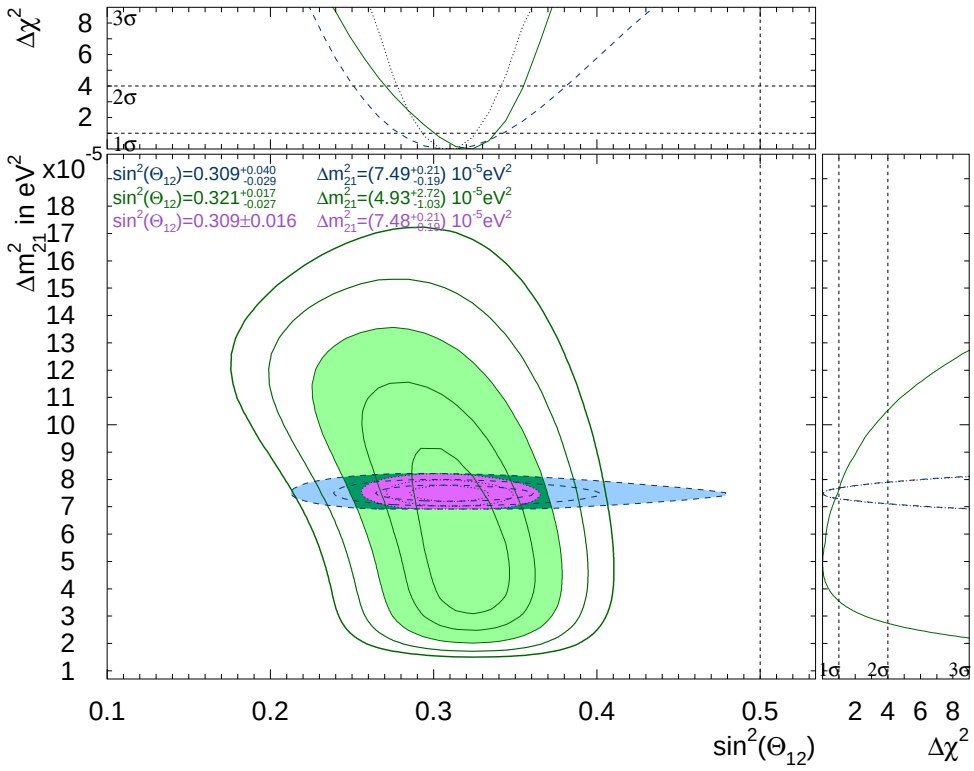

Figure 10.2: The allowed region from the SNO analysis and KamLAND. The χ^2 contours are plotted from 1σ to 5σ levels. The green painted region corresponds to the SK+SNO 3σ allowed region, the blue painted region corresponds to the KamLAND 3σ allowed region and the purple painted region corresponds to the SK+SNO+KamLAND 3σ allowed region.

$$sin^2(\theta_{12})\text{,all solar,KamLAND} = 0.304^{+0.013}_{-0.013} \quad (10.9)$$

$$\Delta m^2_{21}\text{,all solar, KamLAND} = 7.44^{+0.20}_{-0.19} \times 10^{-5} eV^2 \quad (10.10)$$

10.3 The future prospects of solar neutrino analysis

As described in Sec.9.4.2 and Sec.9.5, the energy spectrum analysis with the combined SK-I,II,III,IV data showed that the flat probability spectrum was favored at 1.1-1.9σ over MSW-LMA oscillation prediction shapes and the day/night asymmetry analysis showed a non-zero value with 2.3σ significance. In this section, the future prospects of the energy spectrum analysis and day/night asymmetry analysis are described.

10.3.1 Future Energy spectrum analysis

To observe the energy spectrum distortion due to the MSW effect, it is necessary to achieve a lower energy threshold(<4.0MeV(kin)), and to reduce the statistical uncertainty in the lower energy region. For this purpose, (1) instllation of another data acquisition system and (2) reducing the background and suppressing statistical uncertainty due to background fluctuation are considered.

- Additional data acquisition system
  The current trigger threshold for data acquisition is limited by the performance of disk access. We are now preparing another data acquisition system, which is called WIT (Wide-band Intelligent Trigger). Fig.10.5 shows a schematic view of the data acquisition system including WIT. Details of the WIT system are described in [40]. In the WIT module, fast online event reconstruction is performed to apply fiducial volume cut. This can reduces backgrounds, in paticular the radioactive background originating in the PMT glass and the fiberglass backings of the PMT enclosures. That is, the WIT system can take lower energy data without introducing more backgrounds. After installation of WIT, the energy threshold will only be limited by the event reconstruction performance, and a 3.0MeV(kin) threshold will be possible.

- Reducing the background
  As shown in Fig.6.15, there are still backgrounds remaining near the wall. The main backgrounds would be a radioactive source from the wall, but we haven't completely understood the origin of those backgrounds. If we understand those backgrounds and remove them, the sensitivity of energy spectrum analysis would be improved.

10.3.2 Future day/night asymmetry analysis

Due to improvements in the solar neutrino MC, the day/night asymmetry result is statistically limited, so by taking more data, the significance will improve. For 10 more years of data, the significance of a non-zero day/night asymmetry will be more than 3σ.

Another prospect for day/night asymmetry analysis is using solar neutrinos at Hyper-Kamiokande (HK)[41]. The HK detector is proposed as a next generation underground water

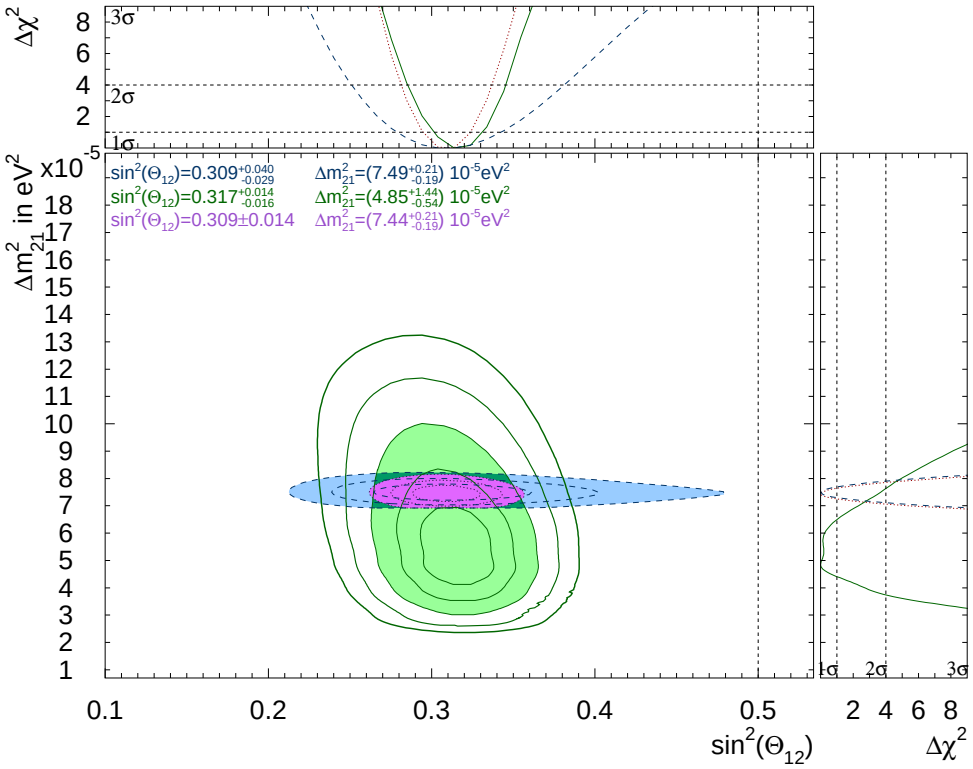

Figure 10.3: The allowed region from the SK and SNO combined analysis and KamLAND. The χ^2 contours are plotted from 1σ to 5σ levels. The green painted region corresponds to the SK+SNO 3σ allowed region, the blue painted region corresponds to the KamLAND 3σ allowed region and the purple painted region corresponds to the SK+SNO+KamLAND 3σ allowed region.

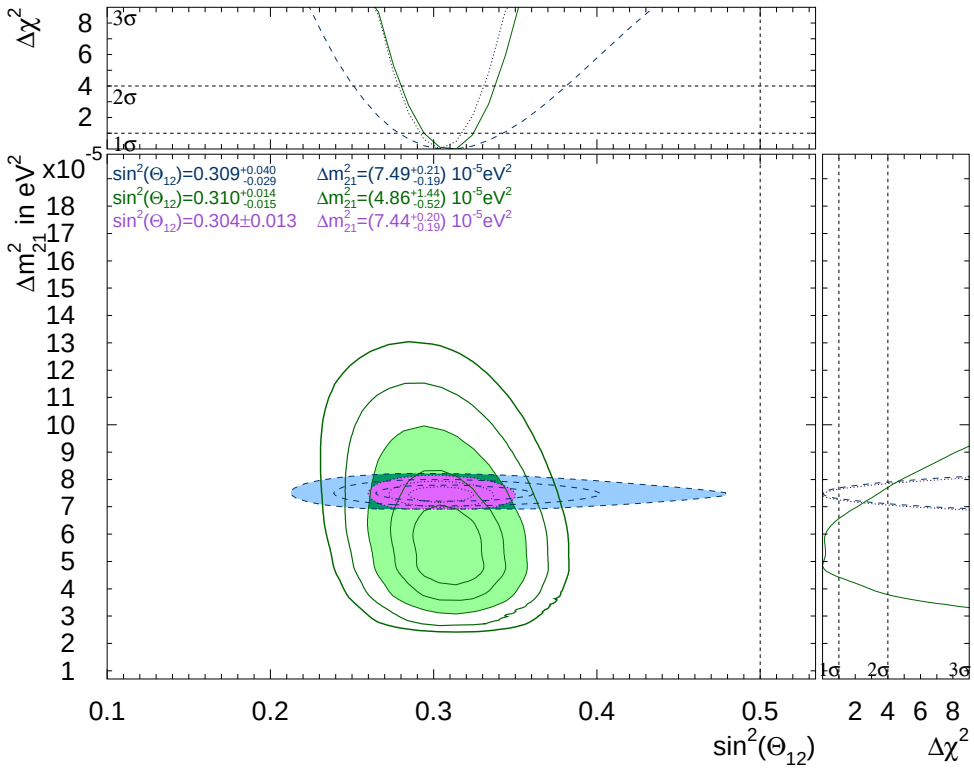

Figure 10.4: The allowed region from all solar combined analysis and KamLAND. The χ^2 contours are plotted from 1σ to 5σ levels. The green painted region corresponds to the all solar 3σ allowed region, the blue painted region corresponds to the KamLAND 3σ allowed region and the purple painted region corresponds to the all solar+KamLAND 3σ allowed region.

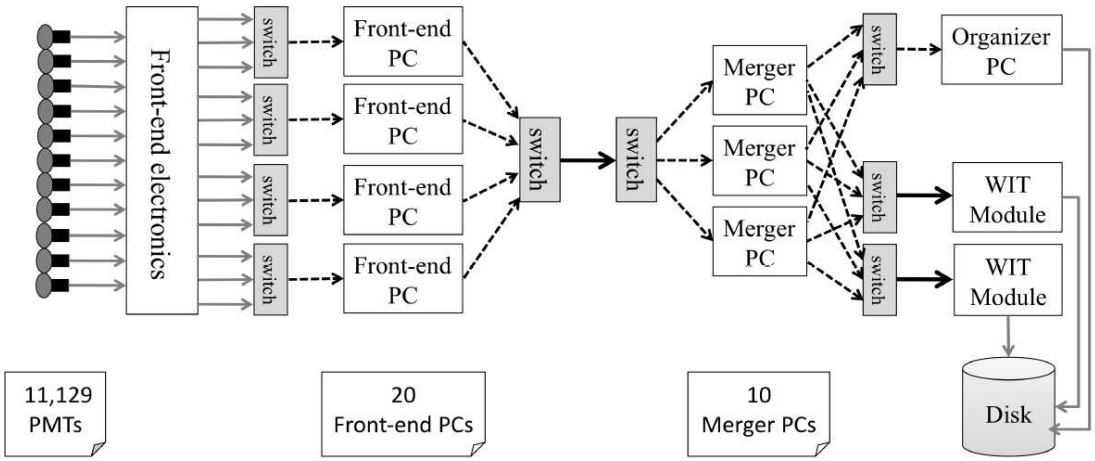

Figure 10.5: Schematic view of the data acquisition system including the WIT system.

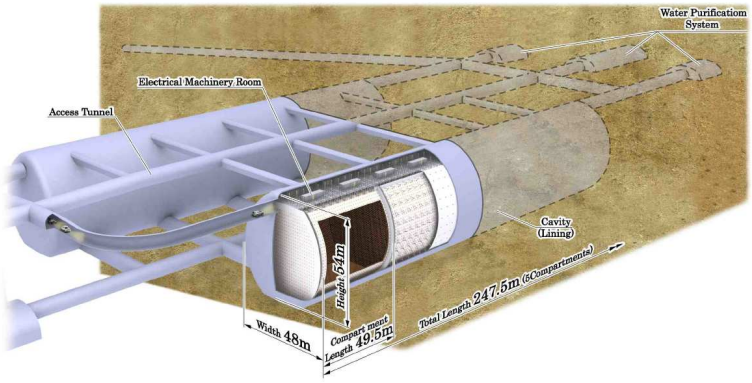

Figure 10.6: Schematic view of the proposed HK detector.

Cherenkov detector and R&D studies are on going. Fig.10.6 shows the schematic view of HK. The proposed total mass of the detector will be 0.99 million metric tons, which is about 20 times larger than SK, and the photo-cathode coverage will be about 20%; similar coverage as SK-II. The HK observation will help the precise measurement of day/night asymmetry with huge statistics.

Chapter 11

Conclusion

The solar neutrino analysis of the fourth phase of the Super-Kamiokande(SK-IV) detector was carried out. With the improvement of the water circulation system, lowering the background level in the central region was achieved and enabled a lowering of the energy threshold of the analysis down to 4.0 MeV(kinetic energy) from 4.5MeV(kin). The position dependence of the water transparency was introduced to the detector simulations for SK-III and IV, and a new parameter to evaluate multiple scattering goodness was introduced in the data analysis. Because of those improvements, statistic and systematic uncertainties were greatly reduced.

The systematic error of the total flux is estimated as $\pm 1.7\%$ in the SK-IV analysis, which is reduced compared with SK-I ($^{+3.5\%}_{-3.2\%}$) and SK-III (2.2%). The ^8B flux obtained from the data in the energy range of 4.0 to 19.5 MeV(kinetic energy) in SK-IV is

$$2.34 \pm 0.03(Stat.) \pm 0.04(Syst.) \times 10^6/cm^2/s, \tag{11.1}$$

which is consistent with the SK-I,II,III results.

The neutrino oscillation analysis combining all SK phases and other solar neutrino experiments (Chlorine, Gallium, SNO and Borexino), give the best fit oscillation parameters as

$$sin^2(\theta_{12}),\text{all solar} = 0.310^{+0.014}_{-0.015} \tag{11.2}$$

$$\Delta m^2_{21},\text{all solar} = 4.86^{+1.44}_{-0.52} \times 10^{-5} eV^2. \tag{11.3}$$

The $\sin^2(\theta_{12})$ values of the solar global analysis and the KamLAND reactor experiment are consistent, but there is a slight tension in the Δm^2_{21} they measure. Combining the results of all solar neutrino experiments and the KamLAND reactor experiment, the oscillation parameters are obtained as

$$sin^2(\theta_{12}),\text{all solar,KamLAND} = 0.304^{+0.013}_{-0.013}$$

$$\Delta m^2_{21},\text{all solar, KamLAND} = 7.44^{+0.20}_{-0.19} \times 10^{-5} eV^2.$$

The χ^2 of the spectrum fit to all SK data with MSW predictions for the two best fit oscillation parameters described above and for an assumption of a flat shape (constant reduction factor independent of energy) are 76.54, 79.2 and 75.29 for 81 d.o.f, respectively. The flat shape is favored at the 1.1-1.9σ level compared with the best fit oscillation parameter predictions.

By introducing the day/night amplitude fit method and with improved systematic uncertainties, the SK combined day/night amplitude was obtained as A_{DN}(=(day-night)/$\frac{1}{2}$(day+night)) = -2.8 $\pm$ 1.1(stat.) $\pm$0.5(syst.) [%], and a hint of a non-zero day/night flux asymmetry, at the 2.3σ level, is seen.

Bibliography

[1] Reiness F., Cowan C.L. Phys. Rev,. 92 830(1953)

[2] B.T.Cleveland et al. Astrophys.J., 496 505(1998)

[3] Y.Fukuda et al. Phys. Rev. Lett 77 420(1998)

[4] J.N.Abdurashitov et al. Phys. Rev. C 80,015807(2009)

[5] W.Hampel et al. Phys. Lett. B 447 127 (1999)

[6] J. Hosaka et al. Phys. Rev.D73,112001(2006)

[7] B.Aharmim et al. arXiv:1109:0763

[8] L.Wolfenstein. Phys. Rev.D 17 2369(1978)

[9] S.P.Mikheyev and A.Yu.Smilnov Nuovo Cim. 9C 17 (1986)

[10] J.N.Bahcall et al. Phys. Lett. B 374 1 (1996)

[11] J.N.Bahcall et al. Phys Rev.Lett., 92 121301 (2004)

[12] D.L.Anderson. Theory of the Earth Blackwell scientfic publication(1989)

[13] Y.Fukuda et al. Phys. Rev. Lett., 81 1562(1998)

[14] Z.Maki et al. Phys. Lett. 28B 498 (1969)

[15] J.N.Bahcall et al. Phys. Rev. D, 51 11(1995)

[16] M.Altmann et al. Phys Lett B 616 174 (2005)

[17] G.Bellini et al. Phys. Rev. Lett., 107 141302(2011)

[18] Jennifer A Thomas, Patricia L vahle. NEUTRINO OSCILLATIONS, Present Status and Future Plans

[19] Y.Abe et al. Phys. Rev. Lett., 108, 13801 (2012)

[20] F.P.An et al. Phys.Rev.Lett., 108, 171803 (2012)

[21] J.K. Ahn et al. Phys. Rev. Lett., 108, 191802 (2012)

[22] S.Abe et al. Phys. Rev. Lett., 100, 221803 (2008)

[23] B.Aharmim et al. Phys. Rev. C 81, 055504 (2010)

[24] K.Nakamura et al. J.Phys. G 37, 075021 (2010)

[25] W. T. Winter et al. Phys.Rev.C, **73** 025503 (2006)

[26] C.E. Ortiz et al. Phys. Rev. Lett., 85 2909(2000)

[27] J.N.Bahcall et al. Phys. Rev. C 54 6146(1995)

[28] H.Nishino et al. Nucl. Inst and Meth A.620(2009)

[29] E.D.Commins and P.H.Bucksbaum. "Weak interactions of Leptons and Photons", (Cambridge University Press, Cambridge, England, 1983)

[30] M.Smy Proc. of the 30th ICRC, 5 1279 (2007)

[31] E. Blaufuss et al. Nucl.Instr.and Meth. A **458** 636 (2001)

[32] W. Y. Chang et al. Nature **139** 962 (1937)

[33] M. Nakahata et al. Nucl.Instr.and Meth. A **421** 113 (1999)

[34] R.M.Pope and E.S.Fry. Appl. Opt. 36, 8710(1997)

[35] J.P. Cravens et al. Phys. Rev. D 78, 032002(2008)

[36] K.Abe et al. Phys. Rev. D 83,052010(2011)

[37] J.N.Bahcall et al. Phys. Rev. D 51 6416 (1995)

[38] M.B.Smy et al. Phys. Rev. D 69,011104(2003)

[39] G.L.Fogli et al. Phys Rev D 66 053010(2002)

[40] G.Carminati Proc. of the 32nd ICRC, Beijing (2011)

[41] arXiv hep-ex 1109.3262 (2011)